Ernst Moritz Arndt Universität Greifswald
Mathematisch-Naturwissenschaftliche Fakultät
Institut für Physik

Masterthesis

Investigation of an In-Situ Calibration Method for the Imaging MSE-Diagnostic on ASDEX Upgrade Utilizing the Edge Zeeman Emission

eingereicht von

Manuel Zolchow

am 04. September 2014

Erster Gutachter: PD Dr. Andreas Dinklage
Zweiter Gutachter: Prof. Dr. Ralf Schneider

Max-Planck-Institut für Plasmaphysik

ERNST MORITZ ARNDT UNIVERSITÄT GREIFSWALD

Wissen lockt. Seit 1456

Abstract

The Imaging Motional Stark Effect diagnostic (IMSE) is a new optical diagnostic installed at ASDEX Upgrade to measure current density profiles in the plasma center utilizing emission from neutral beam injection. Early test measurements at ASDEX Upgrade have shown an unforeseen response of the IMSE-system to the Zeeman split H_α-edge emission. The aim of this thesis is to extend the established theoretical description of the IMSE-system for general measurements of Zeeman H_α-emission in order to determine if this can be used for an in-situ calibration. The main difference to former theoretical description are the emergence of a non negligible degree of circular polarisation and smaller multiplett energy splitting. The results are analysed for varying conditions of magnetic field strength and observation geometry. The general theory was implemented into a forward model, which is based on the measurement geometry and optical setup for the IMSE-diagnostic at ASDEX Upgrade.
The theoretical investigation has shown, that the for calibration essential polarisation angle can not be extracted accurately from measurements. Theoretically it can be obtained by fitting simulated data to measurements. The simulated results from the developed forward model do not fit the measured data. Several measurements were performed at ASDEX Upgrade to find the reason for the deviation. Nearly all physical reason were excluded, but the essential reason causing this deviation was not found. First performance test measurements in laboratory imply, that the diagnostic operates for the Zeeman H_α-emission as theoretically expected, but further measurement are required to verify this

Preface

This work is submitted to the Institut fër Physik of the Ernst Moritz Arndt Universität Greifswald a a master thesis. It serves for the purpose of attaining the academic degree 'Master of Science'.

My deepest gratitude goes to Oliver Ford, Andreas Dinklage and Robert Wolf for the great support, many helpful advices and the nice working atmosphere during my work for this thesis at the Max-Planck-Institut für Plasma Physik in Greifswald. I also want to give thanks to Ralf Schneider, who writes the second survey for my thesis, and to my parents for the financial and moral support during the study of physics.

Contents

Introduction

For over 60 years of nuclear fusion research the ultimate aim has been the development of an efficient fusion power plant for economic electricity production. The huge global increase of energy consumption in the last decades, which result from growing population and global development demands the exploitation of new energy sources for the future. The strong limitation of fossil fuels and their support of global warming due to the anthropogenic greenhouse effect, make the search for new energy source urgent. Existing renewable energy systems have the disadvantage of depending strongly on local environmental factors like sufficient insolation or wind and therefore require not yet available energy storage and transportation. Other energy sources are in competition to essential food production like biogas power plants or constitute strong safety risks for mankind and environment like fission reactors. For a fusion power plant, these fundamental disadvantages are not present or are strongly minimised, so a realisation of a fusion power plant would play a strong role in solving these problems.
Nuclear fusion is a fundamental physical reaction of two atomic nuclei, which fuse to a single particle. The released binding energy is transformed to usable kinetic energy. For an economic fusion power plant the fusion of the hydrogen isotopes deuterium and tritium is expected to be optimal. Since positive charged particles repulse each other due to coulomb repulsion, high temperatures and densities are required to archive a high rate of fusion reactions. Under this condition of high temperature the hydrogen gas is fully ionised and such a gas of free electrons and ions is denoted as plasma state. For an efficient fusion power plant, a high rate of fusion reaction is necessary to produce enough energy to compensate the power needed to maintain the plasma temperature. For this a good confinement of particles and energy is essential. A common limiting criterion for an efficient fusion device is the triple product of electron density n_e, plasma temperature T and energy confinement time τ_E:

$$n_e \tau_E T \geq 10^{21} \mathrm{keV} \frac{\mathrm{s}}{\mathrm{m}^3} \tag{1}$$

One method to confine plasma particles are toroidal magnetic field configurations, since the magnetic field influence the movement of charges particles. Magnetic confinement is the most promising way of plasma confinement for fusion and was investigated in numerous fusion devises like ASDEX Upgrade or Wendelstein AS. The long history of fusion research illustrates the complexity of physical principles in magnetic confined fusion plasmas. To build and operate a efficient fusion power plant for stable energy production, an understanding of fundamental physical plasma processes is essential and requires a lot of theoretical and experimental research. The correct configuration of the magnetic field is critical for sufficient energy confinement and therefore for the efficient operation of a fusion power plant. Therefore diagnostics are required to find stable magnetic field configurations and to localise perturbing deviations, which can for example be caused by evolving plasma instabilities. The great advantage of the Motional Stark Effect diagnostic (MSE) is the possibility to obtain localised measurements of the magnetic field configuration in the center of the plasma, which can not be achieved with the most other diagnostics. The main disadvantages of the standard MSE-diagnostic are a strong limitation of data points and the huge effort needed to realise accurately calibrated measurements. The newly de-

veloped IMSE-diagnostic was designed to measure an entire two dimensional grid of data points with comparably little effort. First performance test in the laboratory and measurements at ASDEX Upgrade have verified the basic functionality of the IMSE-diagnostic, but have also demonstrated, that a deeper understanding of the physical principles for the IMSE diagnostic is still needed to optimise the system to the required accuracy. For the accuracy optimisation of the current IMSE-system, the greatest challenge is search for a reliable and accurate calibration method. Until now the IMSE diagnostic can only be calibrated roughly by geometrical measurements of the viewing directions inside the plasma vessel. During the tests the emission of Zeeman split H_α light from the plasma edge was observed. This was thought may to be usable for calibration. For this reason it is necessary to investigate the response of the IMSE-diagnostic to the Zeeman split H_α-edge emission, to improve the fundamental knowledge about the systems functionality and to prove if this can be used for a more accurate calibration. The focus of this thesis lies on the development of a theoretical description of the response of the IMSE diagnostic to the general Zeeman split H_α emission, the discussion of the possibility of calibration, the development of a forward model to apply the developed theory to the observation geometry at ASDEX Upgrade and finally on the interpretation of some initial measured H_α images.
The first three chapter of this thesis will introduce a overview of nuclear fusion, the standard MSE-diagnostic and some basics of polarisation optics. The Zeeman-effect and the corresponding polarisation properties of the Zeeman multiplet will be explained in chapter four. The next two chapters introduce the mathematical description of the IMSE-diagnostic and the response of the system to neutral beam emission and to the Zeeman H_α-edge emission. For the later detailed discussion of the theoretical results will be given with regard to a possible use as a calibration method. Chapter seven introduces a full simulation for the measurement with the IMSE-system at ASDEX Upgrade. The simulated results will be compared to measured data including physical interpretations.

1 Functional Principles of nuclear fusion and tokamaks

Since this work focuses on an optical diagnostic for the fusion device ASDEX Upgrade, this section introduces the physical principle of nuclear fusion, some basics on magnetic confinement and the concept of a tokamak.

1.1 The nuclear fusion process

Nuclear fusion and nuclear fission are two fundamental types of nuclear reactions, which change the composition of atomic nuclei and so the chemical element. During nuclear fusion, two lighter nuclei combine to one heavier nucleus, while nuclear fission describes the splitting of a heavy nuclei into several lighter nuclei. The history of nuclear fusion began in 1919 with the first experimental observation of a fusion reaction by Ernest Rutherford [1]. He bombarded nitrogen with α-particles and perceived the emergence of oxygen. The reaction can be described by the following reaction equation:

$$^{4}\mathrm{He} + {}^{14}\mathrm{N} \rightarrow {}^{17}\mathrm{O} + {}^{1}\mathrm{H}$$

About 20 years later Bethe and Weizsaecker [2,3] found the complex process of different fusion reactions, that explains the energy production inside the sun by fusion hydrogen. Ever since this time the idea was born to use nuclear fusion as a reliable energy source for mankind. Although the physical principle of nuclear fission was discovered later, it exposed that the implementation of nuclear fission as commercial power plant was easier to realize then for nuclear fusion. The main reason is, that achieving stable and efficient conditions for fusion power plant operation is much more difficult than for a fission reactor, which will be explained later. For a fission reactor the main challenge is the control of the chain reaction for safety, but sufficient energy production can be reached easily. To understand, why both contrary nuclear reactions can be used to reach a positive energy gain, the nuclear binding energy is important. Figure 1 illustrates the binding energy per nucleus E_B for nuclei with different mass numbers A, where mass number is the number of protons and neutrons in one nuclei.

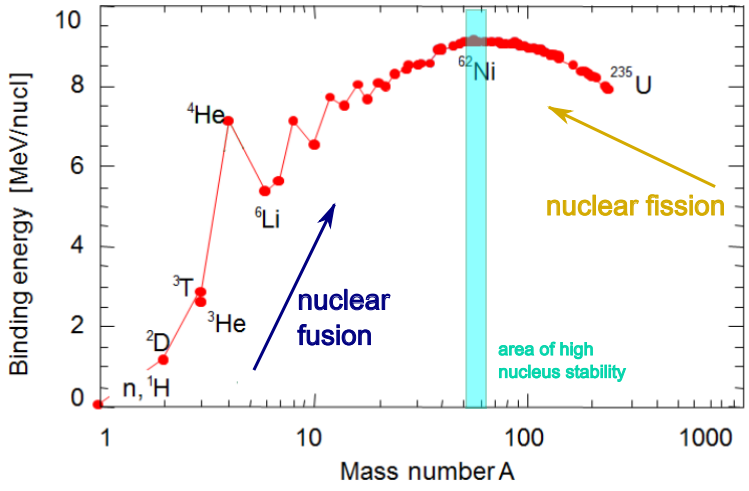

Figure 1 – Nuclear binding energy E_B per nucleus for nuclei with mass number A. Adapted to [4]

It can be seen that the binding energy has a maximum meaning exothermic reactions can be found for fusion of light nuclei and fission of heavy nuclei. The binding energy characterizes the required energy to split a entire nuclei in single protons and neutrons. Nuclear fusion and fission release nuclear binding energy until one of the produced isotope is very stable like for iron. The released energy is in the order of MeV and can be factors higher per reaction for nuclear fusion as for nuclear fission. This means less mass of starting substance is needed per energy unit for fusion.

Since nuclei are positively charged two nuclei repulse each other due to coulomb force. Only after the nuclei approach each other in order of few femtometers, the strong interaction induces the nuclei to fuse. The resulting potential of both effects is called the coulomb wall. For the fusion of two hydrogen nuclei, the potential is 1.2 MeV, which is higher then the averaged thermal energy inside the sun with roughly 1 keV. Only a huge fraction of high energetic hydrogen nuclei and a sufficient probability of tunneling through the coulomb barrier makes fusion possible under this conditions. For a fusion reactor several fusion reactions are possible, but few are efficient enough to release a sufficient amount of energy per reaction with high reaction probability. Figure 2 shows the cross sections for different fusion reactions [5,6]. For realistic temperatures in a fusion reactor of 20-50 keV, the reaction of the hydrogen isotopes deuterium ($A = 2$) and tritium ($A = 3$) will be optimal, since it has the highest reaction probability. For such temperatures gases reach a state of high ionisation called plasma due to the separation of electrons and nuclei [7].

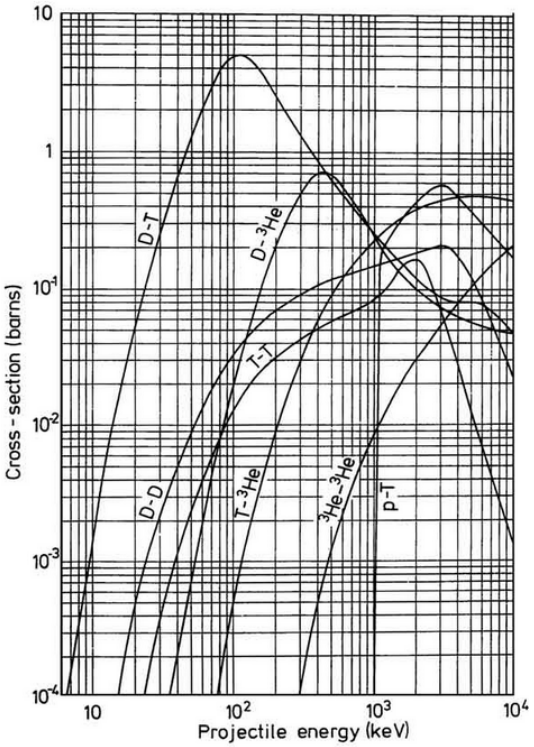

Figure 2 – Cross sections of different fusion reactions dependent on the relative kinetic energy of the reacting nuclei. (Notation: D = deuterium, T = tritium, p = proton, ^{3}He = rare helium isotope with one neutron) [6]

Deuterium and tritium fuse to a helium nucleus (α-particle) and a single neutron by releasing binding energy. For this reaction the coulomb potential is reduced to 0.36 MeV. The coulomb wall for this specific reaction is sketched in Figure 3.

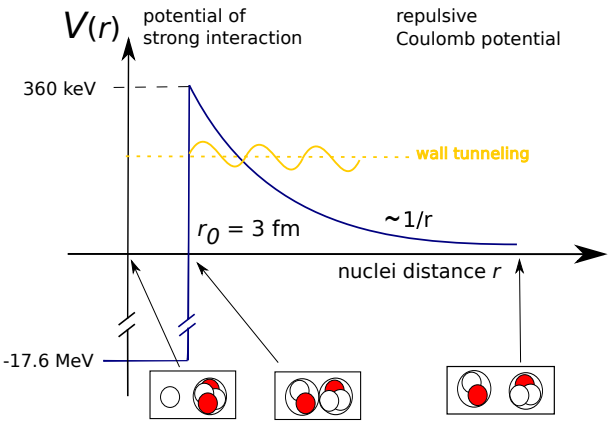

Figure 3 – Coulomb wall between a deuterium nuclei and a tritium nuclei. Adapted to [7]

The reaction equation for deuterium-tritium-fusion with binding energy values is given as follows:

$$ {}^{2}_{1}\mathrm{D}\ (13.4\mathrm{MeV}) + {}^{3}_{1}\mathrm{T}\ (14.9\mathrm{MeV}) \rightarrow {}^{4}_{2}\mathrm{He}\ (8\mathrm{MeV}) + {}^{1}_{0}\mathrm{n}\ (2.4\mathrm{MeV}) + (17.6\mathrm{MeV}) $$

The greater part (approx. 14.06 MeV) of the released binding energy of 17.6 MeV is transferred as kinetic energy to the neutron due to momentum conservation. The kinetic energy of the neutron is used to produce electricity and new tritium from metal lithium by another nuclear reaction. The kinetic energy of the α-particle is necessary to preserve the plasma temperature. The state, when the total power from the α-particles P_α is high enough to balance energy losses by convection and conduction P_{con} and by radiation P_{rad}, is called ignition. In this state of the plasma, no external heating is necessary. To describe the limit for rising ignition, the following triple product can be derived from this power balance.

$$ < n_e \tau_E T > = \frac{\frac{3}{2} P_{con}\ T^2}{\frac{1}{4} < \sigma v >\ f_d^2\ P_\alpha - P_{rad}} \geq 10^{21} \mathrm{keV} \frac{\mathrm{s}}{\mathrm{m}^3} \tag{2} $$

The equation describes the triple product of electron density n_e, the energy confinement time τ_E and the plasma temperature in dependence of the three power values P_α, P_{con} and P_{rad}. $< \sigma v >$ is the characteristic rate coefficient for the deuterium-tritium reaction and f_d is the ion dilution parameter. To reach a high electron density and a high energy confinement time, the plasma particles have to be confined long enough to achieve a sufficient rate of fusion reactions by collisions. In the sun, the confinement is dominated by the strong gravity, which is not possible on earth. To realise a fusion reactor on earth, magnetic confinement is one possibility to reach this aim. To understand the idea of magnetic confinement, single particle motions and drifts in magnetic fields and ideal magnetohydrostatic equilibria have to be explained [7].

1.2 Single particle motions and drifts in magnetic fields

Since plasma particles are electrically charged, their movement can be influenced by electric and magnetic fields. The trajectory of a particle with charge q and mass m in a electric field with field vector $\vec{E}$ and magnetic field with flux density $\vec{B}$ is determined by the Lorenz force $\vec{F}_L$. The classical equation of motion for such a particle is [7,8]:

$$\vec{F}_L = m\frac{dv}{dt} = q(\vec{E} + \vec{v} \times \vec{B}) \tag{3}$$

For further understanding the electric field is neglected due to quasi-neutrality of the plasma and the magnetic field is assumed to be constant. It is also useful to split the velocity $\vec{v}$ of the particle into a component parallel and a component perpendicular to $\vec{B}$, which means $\vec{v} = \vec{v_\perp} + \vec{v_\parallel}$. The Lorenz force, which acts perpendicular to $\vec{v}$ and $\vec{B}$ causes the charged particles to gyrate around the magnetic field lines and having constant velocity $\vec{v}_\parallel$ along the field. The frequency of this motion is cyclotron frequency ω_C:

$$\omega_C = \frac{|q|B}{m}. \tag{4}$$

The radius of the gyration r_L, denoted Larmor radius, can be derived from the force balance between the Lorenz force and the contrary acting centripetal force as follows:

$$|F_L| = |F_{centripetal}| \quad \Rightarrow \quad r_L \; = \; \frac{mv_\perp}{|q|B} \tag{5}$$

For a ion the Larmor radius r_g is larger, but the cyclotron frequency ω_C is smaller in comparison to electron due to the mass difference, if the velocity is the same. The direction of rotation around the magnetic field depends on the sign of the charge q and the center of this rotation is called the guiding center. An illustration of the gyration movement is given in figure 4.

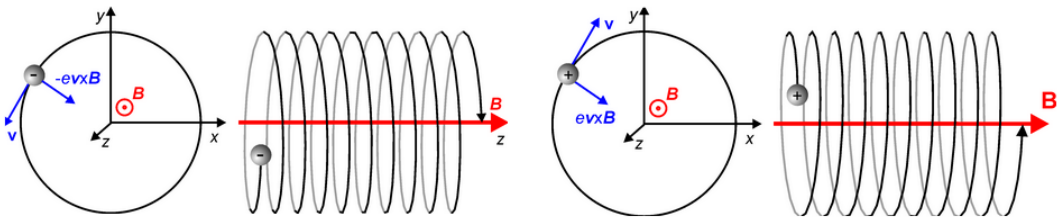

Figure 4 – Gyration movement in constant magnetic fields for a electron (left) and a ion (right) [9]

For this derivation $\vec{E}$ was neglected in formula (3). Generalising formula (3) for a arbitrarily force $\vec{F}$ acting perpendicular to the magnetic field $\vec{B}$ results in the following equation of motion:

$$\vec{F}_F = m\frac{dv}{dt} = F \; + \; q(\vec{v} \times \vec{B}) \tag{6}$$

This new force term influence the general gyration rotation, but introduces a new movement of the guiding center, called guiding center drift, perpendicular to $\vec{B}$.

The general drift velocity is then given by:

$$\vec{v}_F = \frac{\vec{F} \times \vec{B}}{qB^2} \tag{7}$$

The most important guiding center drifts in tokamak physics will be introduced in the following enumeration:

1. $\vec{E} \times \vec{B}$-drift from a perpendicular constant electric field

$$\vec{F}_{\vec{E}} = q\vec{B} \qquad \text{and} \qquad \vec{v}_{\vec{E}} = \frac{\vec{E} \times \vec{B}}{B^2} \tag{8}$$

2. $\nabla\vec{B}$-drift caused by magnetic field gradients perpendicular to $\vec{B}$, where $\mu = \frac{1}{2B} m v_\perp$ is the magnetic momentum of the particle

$$\vec{F}_{\nabla\vec{B}} = -\mu_M \nabla\vec{B} \qquad \text{and} \qquad \vec{v}_{\nabla\vec{B}} = -\mu \frac{\nabla\vec{B} \times \vec{B}}{qB^2} \tag{9}$$

3. Curvature drift caused by bending of the magnetic field lines with bending radius R_C introducing a centripetal force

$$\vec{F}_c = m v_\parallel^2 \frac{\vec{R}_c}{R_c^2} \qquad \text{and} \qquad \vec{v}_c = \frac{m v_\parallel^2}{qB^2 R_c^2} \vec{R}_c \times \vec{B} \tag{10}$$

For the curvature and the $\nabla\vec{B}$-drift the direction of the drift velocity depends on the charge of the particle, whereas the $\vec{E} \times \vec{B}$-drift is for all charged particles in the same direction.
If the plasma is described in the fluid picture, other drifts effects can appears. If the fluid pressure has a gradient perpendicular to the magnetic field $\vec{B}$, the fluid motion of a single plasma species is influenced by the diamagnetic drift with following drift velocity.

$$\vec{v}_{diag} = -\frac{\nabla p \times \vec{B}}{qnB^2} \tag{11}$$

This direction of the diamagnetic drift also depends on the particle charge. For a plasma as a mixture of electron and ion fluid with pressure $p = p_e + p_i$ the different drift directions lead to a current, which is called diamagnetic current and can be calculated as follows:

$$\vec{j}_{diag} = -\frac{\nabla p \times \vec{B}}{B^2} \tag{12}$$

1.3 Magnetic confinement and ideal magnetohydrostatic equilibrium

A hot fusion plasma can be assumed to be approximately close to a thermal equilibrium state, in which the velocity distribution of plasma particles is characterised by a Maxwellian distribution. In this case the plasma can be described in sense of thermodynamics as an ideal gas with the ideal gas law $pV = Nk_BT$. The kinetic plasma pressure can then be expressed as a sum over the different particle species with $p = \Sigma_i n_i k_B T_i$. If the plasma is confined by a magnetic field in a finite volume V a pressure gradient ∇p is introduced due to conservation of relative momentum.

If the plasma has vanishing resistivity and stationary conditions are given (i.e. plasma fluid has small velocity), the ideal magnetostatic equilibrium equation is valid in zeroth order [7, 8]:

$$\nabla p = \vec{j} \times \vec{B} \tag{13}$$

This equation shows, that the force of pressure gradient in a magnetic field is balanced by an induced current j_{diag}, which is the diamagnetic current, which was introduced in formula 12. The magnetic field, the diamagnetic current and the pressure gradient must be perpendicular to each other to archive this stable confinement conditions. It can be shown mathematically, that for magnetic field lines in torus geometry these conditions are achievable.
Remembering the single particle motion, bending of magnetic field lines to a simple torus seems logical for particle confinement, since particles gyrate around the magnetic field lines. But even if collisions are ignored, particle losses will occur due to the particle drifts. The bending of the magnetic field leads to a gradient of $\vec{B}$ in radial direction. These results in a vertical ∇B-drifts, which leads to charge separation, since the drift has opposite directions for electron and ions. The induced electric field causes a $\vec{E} \times \vec{B}$-drift pushing all charged particles radially out of the torus. To avoid particle losses due to radial drifts, a poloidal component can be added to the magnetic field. This leads to a twisting of the magnetic field lines, which then create closed and nested magnetic flux surfaces (see figure 5). Each of these flux surfaces can be related to a constant value of the magnetic flux Ψ.

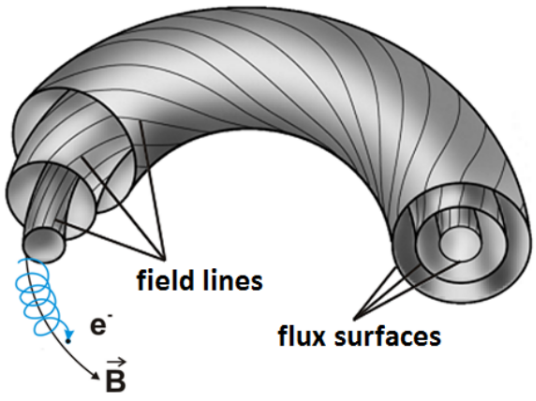

Figure 5 – Flux surfaces and magnetic field orientation for toroidal confinement. [4]

Fundamentally different concepts to add a poloidal magnetic field were developed through fusion history, which are tokamaks and stellerators. Both types will be introduced shortly:

1. **Stellerator** For a stellerator, the poloidal magnetic field component is created by external coils around the plasma vessel, which allows steady state operation. Different complex three-dimensional configurations of the magnetic field and of the coils are possible, optimised by numerical results in progressing plasma theory. In general, the descriptions of physical properties of a stellerator plasma are more difficult due to the missing axial symmetry. A stellerator also needs much more engineering effort and accuracy.

As an example, figure 6 illustrates the magnetic flux surface and the complex coil configuration for the stellerator *Wendelstein 7-X*.

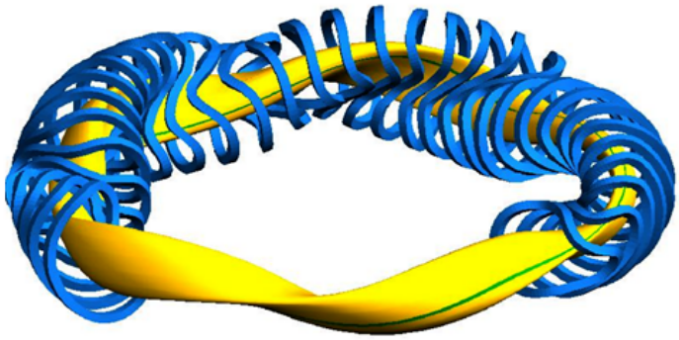

Figure 6 – Flux surface and coil configuration for the optimised stellerator *Wendelstein 7-X*. [4]

2. **Tokamak** In a tokamak, the poloidal magnetic field is generated by a high toroidal current of several MA induced by a transformator coil in the tokamak center. Therefore, only pulse operation is possible. Additionally, the high current promotes plasma instabilities, which can lead to high and sudden energy flows. Since this can result in damage of the plasma vessel, additional protection components inside the plasma vessel and a careful device operation is required. The vertical field coils are needed to produce together with the plasma current closed magnetic flux surface inside the plasma vessel. The configuration of the magnetic field in a tokamak is only two-dimensional, since the magnetic field is axial symmetric. Therefore physical descriptions of plasma properties and effects are in general simpler, just as building such devices. A picture with the relevant coils in a tokamak and the magnetic field orientation is illustrated in figure 7.

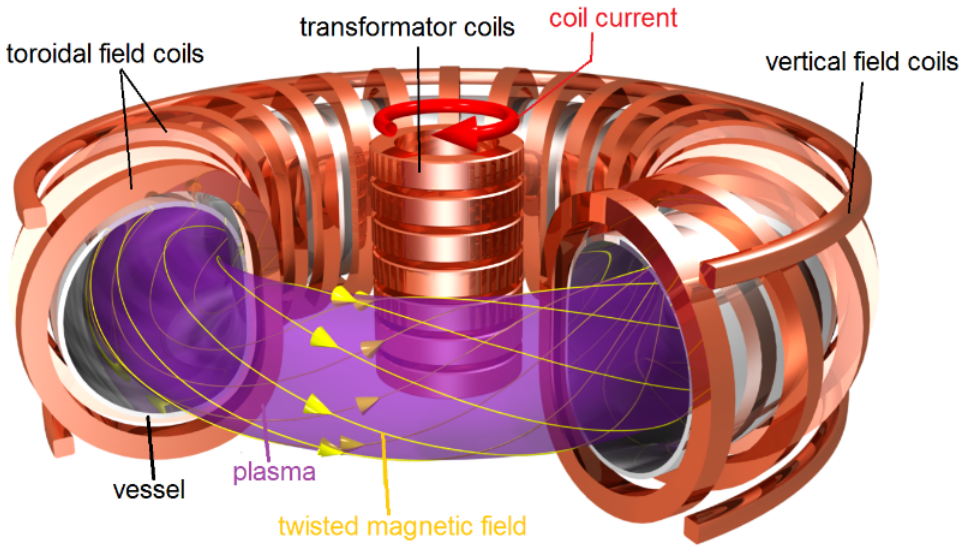

Figure 7 – Magnetic field orientation and relevant coils in a tokamak. [4]

The magnetic field configuration in a tokamak can be best described in cylindric coordinates. Since a tokamak has a axial symmetry, the function of the magnetic flux $\Psi(R, Z)$ is independent of the angle ϕ. Constant values of $\Psi(R, Z)$ describe a magnetic flux surface. Starting from the magnetostatic equilibrium equation in formula (13) a differential equation for the magnetic flux $\Psi(R, Z)$ can be found. For this it is only necessary to transform the equilibrium equation in cylindric coordinates and using basic mathematical relations. The result is the following Grad-Shafranov equation, where p is the pressure and B_ϕ the toroidal magnetic field [7].

$$R\frac{\partial}{\partial R}\left(\frac{1}{R}\frac{\partial \Psi}{\partial R}\right) + \frac{\partial^2 \Psi}{\partial Z^2} = -\mu_0 R^2 \frac{dp}{d\Psi} - \frac{1}{2}\frac{d(RB_\phi)^2}{d\Psi} \tag{14}$$

In practise it is only possible to solve the Grad-Shafranov equation numerically. Solving this equation requires boundary conditions from measurements e.g. the field outside the vessel, which can be measured at the poloidal field coils with induction measurements. Since these are only a integrated values over the magnetic profile, this will in general not give accurately the entire current density profile. The current density profile, respectively the complete configuration of the magnetic field, are of interest for understanding the most dynamic plasma phenomena in tokamaks e.g. special instabilities. To improve the results from numerical calculations, it is essential to get as much informations about the current density profile as possible from several other measurements. One of these measurements is the MSE-polarimetry, which leads to data for the local magnetic field orientation, especially the magnetic field pitch angle γ_{pitch} inside the plasma. This angle is defined by the ratio of the poloidal magnetic field B_θ and the toroidal magnetic field B_ϕ in following formula [10]:

$$\tan(\gamma_{pitch}) = \frac{B_\theta}{B_\phi} \tag{15}$$

The next chapter will introduce the MSE-system on the tokamak ASDEX Upgrade, for which the new IMSE-system is an improved modification.

2 MSE-diagnostic on ASDEX Upgrade

The MSE-method is a standard optical diagnostic to achieve informations about the magnetic field direction in tokamaks and stellerators. Results from the measurements are often used in combination with other measurements to learn more about fundamental plasma dynamic processes. This chapter will introduce the setup and the measuring principle of the MSE-system installed on ASDEX Upgrade [11–13]. Discussing advantages and disadvantages will explain the requirement for the new IMSE-system, which can be directly installed at the existing MSE-system port at ASDEX Upgrade.

2.1 The MSE-spectrum

The MSE-system measures the emission from high energy neutral hydrogen or deuterium atoms, which are injected into the tokamak plasma via neutral beam injection (NBI). Since especially the magnetic field information from the plasma center are often required, the neutral beam reaches wide inside the plasma. Inside the plasma the neutrals become excited by collisions with the plasma electrons and ions, which leads to characteristic line emission. Typically used for MSE-measurements are the Balmer-α lines. Due to the high velocity ($v \approx 0.01 \cdot c$) of the neutrals, a Lorenz electric field $\vec{E} = \vec{v} \times \vec{B}$ is introduced. This causes a splitting of the spectral lines due to the Stark effect, which dominates over the Zeeman-splitting. The light of the different optical transitions have different polarisation states. Viewing perpendicular to the beam, the spectral lines denoted with π are linear polarised parallel to the electric field, whereas the Σ-components are also linear polarised but perpendicular to the electric field. In first order a simple MSE-multiplett consists of a π^--, π^+- and a σ-component, if the quantum mechanic coupling of Stark- and Zeeman-effect is ignored. The high particle velocity also results in a Doppler-shift relative to background radiation of the entire MSE-multiplett. The neutral beam source not only produces H and D atoms, but the molecules H_2, D_2 and H_3, D_3. The heavier molecules have smaller velocities of $\sqrt{2}v$ and $\sqrt{3}v$, which results in lower values for Stark-splitting and Doppler shift. A typical MSE-spectrum therefore has three different single MSE-multipletts. A sketch of a MSE-spectrum is shown in figure 8.

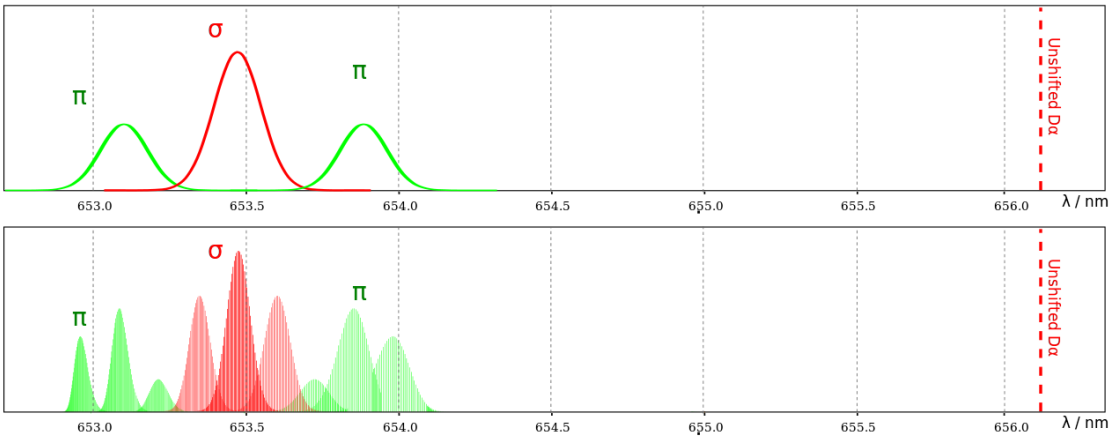

Figure 8 – Simulated results of an Doppler shifted MSE-spectrum with only main components (upper part) and with additional sub-levels (lower part). [14]

Measuring the polarisation state of different MSE-components separately would lead to informations about the magnetic field orientation, whereas the whole MSE multiplett together is unpolarised. The measurement setup will be explained in the next section [12, 13].

2.2 MSE-Setup

The emitted light from the neutral beam is transmitted first through different optics to the relevant measurement setup. Starting from the neutral beam the emitted light is reflected by a dielectric mirror, which has nearly full reflectance for the characteristic MSE wavelength range. This is important, since a normal mirror would change the polarisation direction due to different reflectance for parallel and perpendicular polarised light relative to the incident plane. Between the mirror and the plasma, a silica window (a.k.a. protection cover) and a shutter are installed to protect the dielectric mirror against contamination and damages through plasma heat. After the mirror, the light is transferred by some lenses to the setup for polarimetric measurements. At this position the IMSE-system can be installed. The path of the emitted light through the optics on ASDEX Upgrade is illustrated in figure 9.

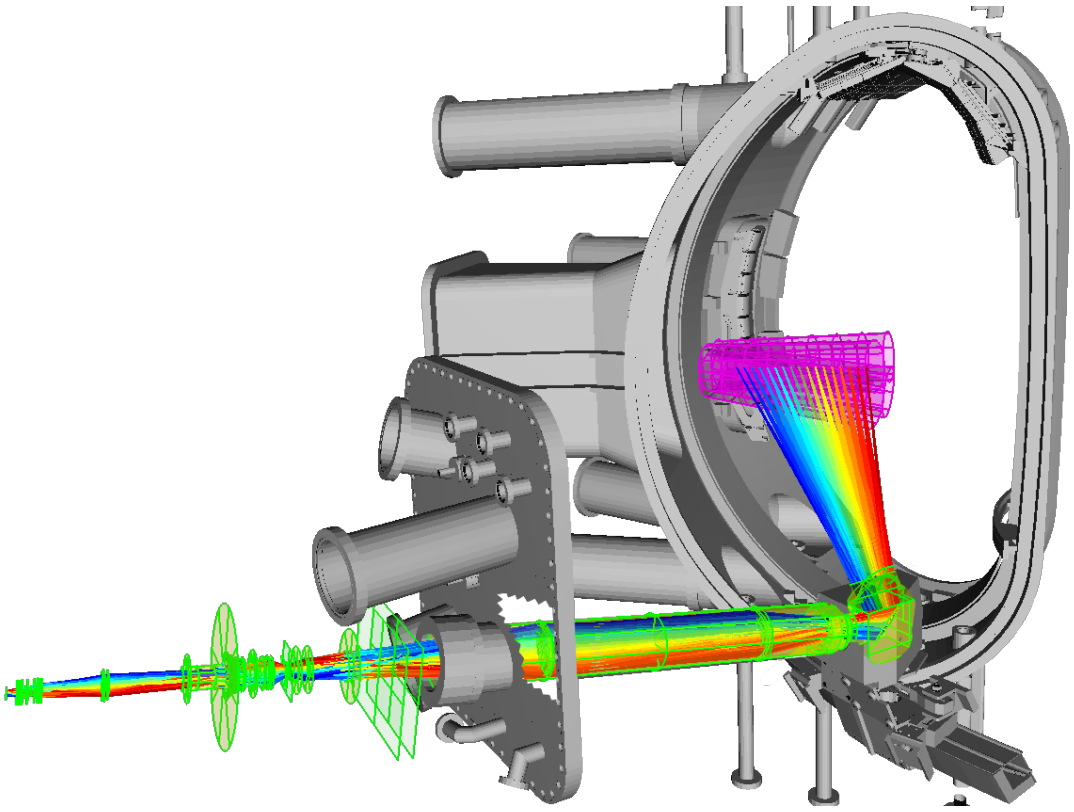

Figure 9 – Geometry of the MSE-diagnostic on ASDEX Upgrade [15]

The following section explains the standard MSE measurement [11,12]. To separate the polarisation state in standard MSE-measurements, each of the different viewing directions (MSE channel) require a very narrow and tunable interference filters with spectral width under 0.3 nm to separate the MSE-components. To measure the polarisation of the separated MSE-components for a fixed viewing direction, a modulated polarimeter is used. This modulated polarimeter consists of two piezoelectric modulators (PEM) and a linear polariser. A PEM introduces a time modu-

lated phase delay to the light wave. The both PEMs are rotated by 22.5° to each other and have two different modulation frequencies ω_1 and ω_2. Both PEMs together encode the polarisation direction of the incoming linear polarised light wave in the two modulated phase delays. The linear polariser converts the phase modulations into amplitude modulations of the light intensity. The polarisation direction can be achieved from the ratio of these amplitudes for the different modulation frequencies. Therefore some more electrical components like digitisers are necessary. Since the amplitude of intensity variation is only a weak signal, an amplifier is also needed to increase the signal strength. From the polarisation direction the magnetic pitch angle γ_{pitch} can de calculated, if the system is sufficiently well calibrated. The setup as explained in this section lead to some advantages and disadvantages for the MSE-diagnostic [12].

The main advantage of any MSE-system and also the new IMSE-diagnostic is the possibility of pitch angle measurements in the plasma center if the system is calibrated sufficiently. On the other hand, the standard MSE-method has some meaningful disadvantages:

1. A spectral discrimination of the different MSE-components with narrow filter is only possible for a sufficiently high motional Stark splitting, which requires in general magnetic field over 1 T.

2. Since the strength of the Doppler shift varies along the neutral beam, each viewing direction requires a different narrow filter. This also allows only a fixed energy of the neutral beam, because changing the beam energy would also effect the strength of the Doppler-shift.

3. Only the measurement of a strong limited number of data points is practical, since each viewing direction requires the complete polarimetric setup as explained in this section.

4. For each MSE channel a complicated individual calibration is necessary to achieve results with sufficient accuracy

Especially the strong limit of data points and the expensive need of many optical and electrical components have lead to the idea of building the IMSE-system, which avoids these intrinsic problems. To understand the measuring principle of the IMSE-system some physical basics about polarisation are needed. These are introduced in the next chapter.

3 Physical Basics of polarisation for optical devices

With the aim of investigating the response of the polarimetric IMSE-system to the H_α-edge emission in ASDEX Upgrade, a comprehension of the general polarisation properties of light is necessary. This chapter will explain the different types of polarisation and the physical principle of birefringence. Afterwards, the Stokes-Müller formalism is introduced to give a general characterisation of basic optical components and their influence on arbitrary polarisation states. These are required to describe the measuring principle of the IMSE-sytem mathematically, which is described later.

3.1 Characterisation of different types of polarisation

An arbitrary polarisation state of an electromagnetic wave can be described by the polarisation ellipse [16, 17]. The ellipse is traced out by the time evolving electric field vector $\vec{E}$ on a fixed point in space. The resulting polarisation ellipse is defined by the half-axes a and b and can be represented by the polarisation angle θ and the ellipticity angle χ. The reference frame for polarisation description in this chapter is given with the coordinates x,y and z. Figure 10 illustrates the polarisation ellipse for this reference frame.

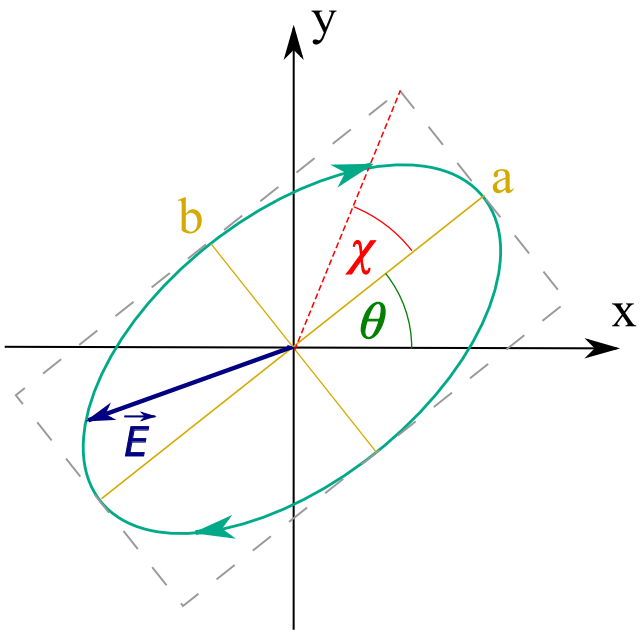

Figure 10 – Polarisation ellipse in the reference frame (x,y) with polarisation angle θ and ellipticity χ. [16]

Starting with this general characterisation, the following three types of polarisation can be differentiated:

1. Pure linear polarisation ($\chi = 0°$): The electric field vector, changing its strength and sign periodically, lies along the the half-axis a. The orientation of the plane in which the $\vec{E}$-field lies relative to a fixed reference frame (x,y), is given by the polarisation angle θ. The polarisation ellipse is a straight line for this case.

2. Pure circular polarisation ($\chi = \pm 45°$): The electric field has a constant strength (i.e. polarisation ellipse is a circle) and rotates with constant angular velocity in the reference frame (x,y) perpendicular to the waves propagation direction. The sign of χ relates to the rotational direction of $\vec{E}$. Viewing parallel but opposite to the propagation direction, the light is left circularly polarised ($\chi = 45°$) if $\vec{E}$ rotates anticlockwise, and right circularly polarised ($\chi = -45°$) if $\vec{E}$ rotates clockwise. Since there is no linear part of polarisation θ is irrelevant.

3. Elliptical polarisation: In all other cases the light is partly linear and circular polarised, so that the strength and the direction of the electric field vector oscillates periodically in the (x,y)-frame. The greater the absolute value of χ, the greater the circularly polarised part. The sign of χ indicates the direction of rotation. The angle θ gives the direction, in which the linear part is polarised and $|\vec{E}|$ has its maximum.

A wave with an arbitrary polarisation state can be constructed by two independent linear waves. The polarisation planes of these waves are orientated perpendicular to each other and the waves have a constant phase difference ϕ_P. If the phase delay between these is a multiple of π the resulting wave is linear polarised with polarisation orientation depending on the amplitude ratio. To create circular polarisation the amplitudes have to be identical and the phase delay is $\pi/2$. In each other case the polarisation is elliptical. In the next section a more mathematically way to characterise polarisation is introduced.

3.2 Stokes-Müller fomalism and discription of optical components

Definition of Stokes vectors

In applied physics another way of describing the polarisation of light is commonly employed because of its link to measurable quantities. This is the Stokes-Müller-Formalism, where each polarisation state can be described by four real values, which are summarized as the Stokes vector $\vec{s}$ defined as follows:

$$\vec{s} = \begin{pmatrix} s_0 \\ s_1 \\ s_2 \\ s_3 \end{pmatrix} = \begin{pmatrix} I \\ I p_{tot} \cos(2\theta)\cos(2\chi) \\ I p_{tot} \sin(2\theta)\cos(2\chi) \\ I p_{tot} \sin(2\chi) \end{pmatrix} = \begin{pmatrix} \langle E_x^2 + E_y^2 \rangle_t \\ \langle E_x^2 - E_y^2 \rangle_t \\ \langle 2E_x^2 E_y^2 \cos(\phi_P) \rangle_t \\ \langle 2E_x^2 E_y^2 \sin(\phi_P) \rangle_t \end{pmatrix} = \begin{pmatrix} P_{0°} + P_{90°} \\ P_{0°} - P_{90°} \\ P_{45°} - P_{135°} \\ P_{RHC} - P_{LHC} \end{pmatrix} \tag{16}$$

The Stokes vector depends on θ and χ and the total intensity I of the polarised light. The total degree of polarisation p_{tot} describes the ratio between polarised intensity and the total intensity of the light and can be defined as in formula (17). Formula (17) also introduces the ratio of linear polarised light p_{lin} and circular polarised light p_{circ} relative to the total intensity I.

$$p_{tot} = \frac{\sqrt{s_1^2 + s_2^2 + s_3^2}}{s_0} \qquad p_{lin} = \frac{\sqrt{s_1^2 + s_2^2}}{s_0} \qquad p_{cyrc} = \frac{|s_3|}{s_0} \tag{17}$$

An alternative way to calculate the Stokes vectors uses the time averaged amplitudes of $\vec{E}$ in x- and y-direction and their relative phase ϕ_P. To obtain the Stokes vectors experimentally, the

luminous power P_ε of the light after passing an a ideal polariser at angle ε has to be measured, where $\varepsilon = 0°$ is orientated in x-direction. P_{LHC} and P_{RHC} are the luminous power of the left-handed and right-handed part of the polarised light. After characterising polarisation states with Stokes vectors, the following section introduces the Müeller matrices to describe optical components.

Definition of Müller matrices

To analyse the functional principle of a polarimetric system it is essential to describe the effect of optical components on the state of polarisation [16, 18]. Therefore each optical component is characterised by a Müller matrix $\mathbf{M}$ connecting the input $\vec{S}_{in}$ and output $\vec{S}_{out}$ polarisation state of a passing light wave the by following relation:

$$\vec{S}_{out} = \mathbf{M} \cdot \vec{S}_{in} \tag{18}$$

Several optical components, which are used as components for the IMSE-system, and their corresponding Müeller matrices will be explained more in detail is the following passage.
An ideal polariser with optical axis rotated by the angle θ_A relative to the x-direction of the reference (x,y)-frame transforms arbitrary polarised light into linear polarised light ($\chi = 0$) with polarisation angle $\theta = \theta_A$. In general a linear polariser also reduces the intensity. The corresponding Mueller matrix for an ideal polariser is:

$$\mathbf{M}^P(\theta_A) = \frac{1}{2}\begin{pmatrix} 1 & \cos(2\theta_A) & \sin(2\theta_A) & 0 \\ \cos(2\theta_A) & \cos^2(2\theta_A) & \sin(2\theta_A)\,\cos(2\theta_A) & 0 \\ \sin(2\theta_A) & \cos(2\theta_A)\,\sin(2\theta_A) & \sin^2(2\theta_A) & 0 \\ 0 & 0 & 0 & 0 \end{pmatrix} \tag{19}$$

To introduce a phase delay ϕ between the ordinary and the extraordinary part of a electromagnetic wave, a delay plate can be used. The separation of a light wave into an ordinary and an extraordinary wave, if a electromagnetic wave passes through a birefringent crystal, is a result of a crystal optical anisotropy. This anisotropy can be characterised by the optical axis of the material, which is defined along the direction, where this separation is not introduced. The ordinary wave has the electric field vector perpendicular to the plane generated by the incident direction of the incoming light wave and the vector in direction of the optical axis. The electric field vector lies inside this plane. The ordinary and the extraordinary wave pass through the crystal with different velocities, which can be expressed by different refractive indices. The difference of the refractive indices result in a phase delay between the ordinary and the extraordinary component of the light wave. For a delay plate with optical axis rotated at angle θ_A relative to the x-direction in the (x,y)-reference frame, the Müller matrix is given as follows:

$$\mathbf{M}^D(\theta_A, \phi) = \begin{pmatrix} 1 & 0 & 0 & 0 \\ 0 & \cos^2(2\theta_A) + \sin^2(2\theta_A)\,\cos(\phi) & \sin(2\theta_A)\,\cos(2\theta_A)\,(1+\cos(\phi)) & -\sin(2\theta_A)\,\sin(\phi) \\ 0 & \sin(2\theta_A)\,\cos(2\theta_A)\,(1+\cos(\phi)) & \sin^2(2\theta_A) + \cos^2(2\theta_A)\,\cos(\phi) & \cos(2\theta_A)\,\sin(\phi) \\ 0 & \sin(2\theta_A)\,\sin(\phi) & -\cos(2\theta_A)\,\sin(\phi) & \cos(\phi) \end{pmatrix} \tag{20}$$

An universal explicit formula to calculate the phase delay between ordinary and extraordinary wave components introduced by a birefringent uniaxial and plane-parallel delay plate was found by *Veiras et al.* [19], see equation (21). This formula was derived without any use of approximations. The important plate parameters are the thickness L, the angle between the optical axis and the plate interface ρ, and the refractive indices n_O and n_E for an ordinary and an extraordinary ray passing the birefringent media. The incident wave is characterized by the wavelength λ, the incident angle α ($0° \leq \alpha < 90°$) and the angle δ ($0° \leq \delta < 360°$) between the plane of incidence and the projection of the optical axis on the plate interface. The complete geometry is illustrated in Figure 11. The plates surrounding media has the refractive index n_M and the parameter $S_V = n_E^2 \sin^2(\rho) + n_O^2 \cos^2(\rho)$ is introduced for clarity.

$$\phi = \frac{2\pi L}{\lambda}\left(\left(n_O^2 - n_M^2 \sin^2(\alpha)\right)^{\frac{1}{2}} + \frac{1}{S_V}(n_M(n_O^2 - n_E^2)\sin(\rho)\cos(\rho)\cos(\delta)\sin(\alpha)) - \frac{n_O\{n_E^2 S_V - [n_E^2 - (n_E^2 - n_O^2)\cos^2(\rho)\sin^2(\delta)]n_M^2\sin^2(\alpha)\}^{\frac{1}{2}}}{S_V}\right) \tag{21}$$

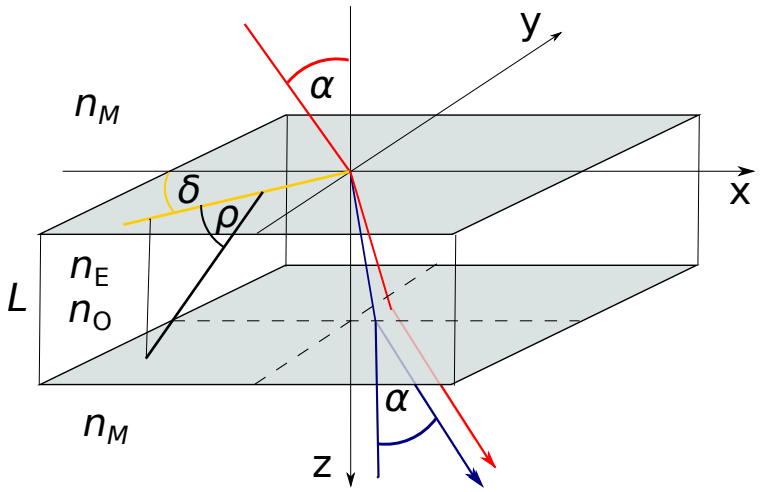

Figure 11 – Ordinary (red) and extraordinary (blue) transmission through a unaxial plane-parallel birefringent plate with refractive indices n_E and n_O and optical axis (black) surrounded by an isotropic medium [19].

There are two special delay plates, which are not a component of the IMSE-system, but used to create defined polarisations states. These are needed to realise accurate measurements in laboratory to test the response of the IMSE-system to elliptical polarised light. These special wave plates are the 'half-wave'-plate and the 'quarter-wave'-plate, which both have the optical axis at $\rho = 45°$. For a fixed wavelength λ, a special delay plate material with n_O and n_E and perpendicular incident angle ($\alpha = 0$), the plate thickness L can be selected to introduce a fixed phase delay ϕ_F between the ordinary and the extraordinary wave. For a half-wave plate this phase delay is $\phi_F = \pi$ and the corresponding Müller matrix is:

$$\mathbf{M}^D(\theta_A, \pi) = \begin{pmatrix} 1 & 0 & 0 & 0 \\ 0 & \cos(4\theta_A) & \sin(4\theta_A) & 0 \\ 0 & \sin(4\theta_A) & -\cos(4\theta_A) & 0 \\ 0 & 0 & 0 & -1 \end{pmatrix} \tag{22}$$

The half-wave plate rotates the polarisation angle of the incoming wave ($\theta \longrightarrow \theta + 2\theta_A$) in dependence of the optical axis orientation θ_A and switches the rotation direction of the circular polarised part (sign change of ellipticity χ). As for all delay plates, the total intensity is conserved [18].

The quarter-wave plate gives a phase delay $\phi_F = \pi/2$ with resulting Mueller matrix:

$$\mathbf{M}^D(\theta_A, \pi/2) = \begin{pmatrix} 1 & 0 & 0 & 0 \\ 0 & \cos^2(2\theta_A) & \sin(2\theta_A)\cos(2\theta_A) & -\sin(2\theta_A) \\ 0 & \sin(2\theta_A)\cos(2\theta_A) & \sin^2(2\theta_A) & \cos(2\theta_A) \\ 0 & \sin(2\theta_A) & -\cos(2\theta_A) & 0 \end{pmatrix} \tag{23}$$

$$\mathbf{M}^D(0, \pi/2) = \begin{pmatrix} 1 & 0 & 0 & 0 \\ 0 & 1 & 0 & 0 \\ 0 & 0 & 0 & 1 \\ 0 & 0 & -1 & 0 \end{pmatrix} \qquad \mathbf{M}^D(\pi/4, \pi/2) = \begin{pmatrix} 1 & 0 & 0 & 0 \\ 0 & 0 & 0 & -1 \\ 0 & 0 & 1 & 0 \\ 0 & 1 & 0 & 0 \end{pmatrix} \tag{24}$$

A quater-wave plate at $\theta_A = 0$ or $\theta_A = 45°$ switches s_3 with s_2 or s_1. In the case of fully linear polarised light with polarisation orientation θ as input to a quarter-wave plate with $|\theta - \theta_A| = 45°$ the wave is total circularly polarised afterwards.

4 Zeeman effect and H_α-edge emission

In high magnetic field like in ASDEX Upgrade the shell energy levels of atoms are split due to the Zeeman effect. During the plasma start up the Zeeman emission from the plasma edge introduces a measurable signal at the IMSE-system. This leads to idea that this emission is maybe useful for a in-situ calibration of the IMSE-system. If the neutral beam afterwards is activated the emission from the motional stark effect dominates and the Zeeman effect from the plasma edge is not measurable with the IMSE-system cause of the actual geometry of the MSE-system. Having the calibration idea in mind, this chapter describes the atomic processes leading to the splitting of the H_{alpha}-emission in the plasma edge. Since the IMSE-measurement is based on the polarisation states of the emission, the polarisation properties of the H_α-Zeeman emission are important. The spectral H_α-line is the brightest spectral line in the entire hydrogen spectrum. With a wavelength of 656.28 nm, the emitted light lies in the visible range and has a characteristic red colour.

4.1 H_α-Zeeman effect in strong magnetic fields

In magnetic fields the energy levels of an atomic shell splits due to the influence of the magnetic field to the orbital angular momentum and the spin of the electron. As a consequence more optical transitions can be observed in spectral measurements. As this work focuses on H_α-emission, only single electron systems are of interest. [10, 17, 20]

For a general description of atomic quantum states, the electronic quantum numbers are introduced here. The principal quantum number n relates to the energy shell of the electron (H_α-transition: n=3 $\rightarrow$ n=2). The orbital angular momentum of the electron is described by the vector $\vec{L}$, its orbital quantum number l and the magnetic quantum number m_l. In the same way vectors and quantum numbers can be introduced for the spin angular momentum ($\vec{S}$, s, m_s) and the total angular momentum ($\vec{J}$, j, m_j). In absence of external fields the orbital angular momentum and the electron spin are coupled ($\vec{J} = \vec{L}+\vec{S}$).
In pure magnetic fields, a splitting of atomic quantum levels is caused by the linear Zeeman effect. The general case, historically named anomalous Zeeman effect, includes the spin-orbital coupling. The normal Zeeman effect ignores the electron spin and therefore is only valid if the spins of several electrons add to vanishing total Spin. This never happens for single electron systems like hydrogen or deuterium atoms.

The Energy splitting ΔE is linearly proportional to the magnetic field $|\vec{B}|$ and can be calculated as follows:

$$\Delta E = g_j \mu_B |\vec{B}| \tag{25}$$

with the Bohr magneton $\mu_B = e\hbar/2m_0$ and g-factor g_j. The g-factor for the case of spin-orbital coupling can be calculated from the quantum numbers by following relation [20]:

$$g_j = 1 + \frac{j(j+1) - l(l+1) + s(s+1)}{2j(j+1)} \tag{26}$$

Optical transitions between different energy levels are only possible, if the selection rule $\Delta m_j = 0, \pm 1$ is valid. In strong magnetic fields the electron spin angular momentum can decoupled from the electron orbit angular momentum. Is this case the former description is not valid any more. The decoupling happens, if the coupling between external field and orbital angular momentum or spin angular momentum is stronger then the coupling between electron spin and its angular momentum. The effect is called the Paschen-Back effect. The magnetic field limit for the decoupling increases with the proton number and is therefore relatively small for hydrogen and deuterium. For hydrogen and its isotopes the limit is at around 0.3 T [10]. For H_α-emission from the tokamak edge plasma the system is entirely decoupled, since typical strength of magnetic fields is over 2 T. In the decoupled regime the orbital angular momentum and the spin angular momentum are independently quantised. The energy splitting is given as sum of both independent effects with:

$$\Delta E = (g_l \Delta m_l + g_m \Delta m_s)\ \mu_B\ |\vec{B}| \tag{27}$$

The g-factor for the orbital angular momentum is $g_l = 1$ and for the spin angular momentum $g_s = 2.0023$. For optical transitions the selection rule with regard to the angular momentum is then $\Delta m_l = 0, \pm 1$. On the other hand the electron spin is conserved ($\Delta m_s = 0$) in the Paschen-Back regime, because of the impossibility of spin-reversal for optical transitions. The result is a splitting of one spectral line into three lines, denoted as Zeeman multiplett [20]. The corresponding values for the energy splitting are:

$$\Delta E = 0 \quad \text{and} \quad \Delta E = \pm \mu_B\ |\vec{B}| \tag{28}$$

With the energy splitting, it is possible to calculate the wavelength of the three Zeeman split H_α lines dependent on the magnetic field strength in the Paschen-Back regime. This is shown in Figure 12. The calculated value is needed later as input parameter for the simulation of the IMSE-system and to realise realistic test measurements.

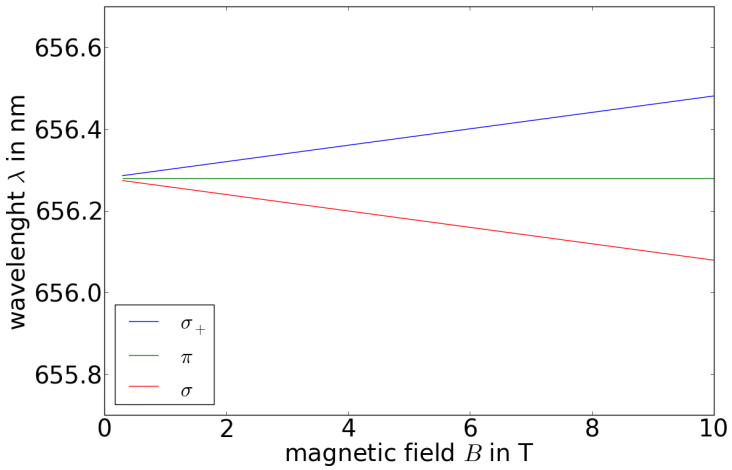

Figure 12 – Zeeman splitting for the H_α-line (656.28 nm) in the Paschen-Back regime

4.2 Polarisation properties of the H_α-Zeeman multiplett

The three components of the Zeeman multiplett have different polarisation states. A description of these polarisation states is needed to understand the response of the IMSE-system to the Zeeman split H_α edge emission. For $\Delta m_l = 0$ the electric field vector $\vec{E}$ of the emitted wave oscillates parallel to the external magnetic field $\vec{B}$. This component in the spectrum is named π-component and vanishes observing in direction parallel to $\vec{B}$, because there is no wave emission in this direction. By observation perpendicular to $\vec{B}$ this component shows linear polarisation. For the lateral components (σ-lines) with $\Delta m_l = \pm 1$ the electric field vector $\vec{E}$ rotates perpendicular to $\vec{B}$, so the polarisation state observed in magnetic field direction is circular. In perpendicular observation to the magnetic field the σ-components are linear polarised within the same polarisation plane (same polarisation angle), which is perpendicular to the polarisation plane of the π-component. The component $\sigma^\pm$ belongs to $E \pm \Delta E$ transitions. The wave of the component σ^+ with higher frequency is right-handed polarised relative to the direction of the magnetic field, whereas σ^- is left-handed polarised. For an overview the different polarisation states of the Zeeman multiplett for perpendicular and parallel observation are sketched in Figure 13. [10,20].

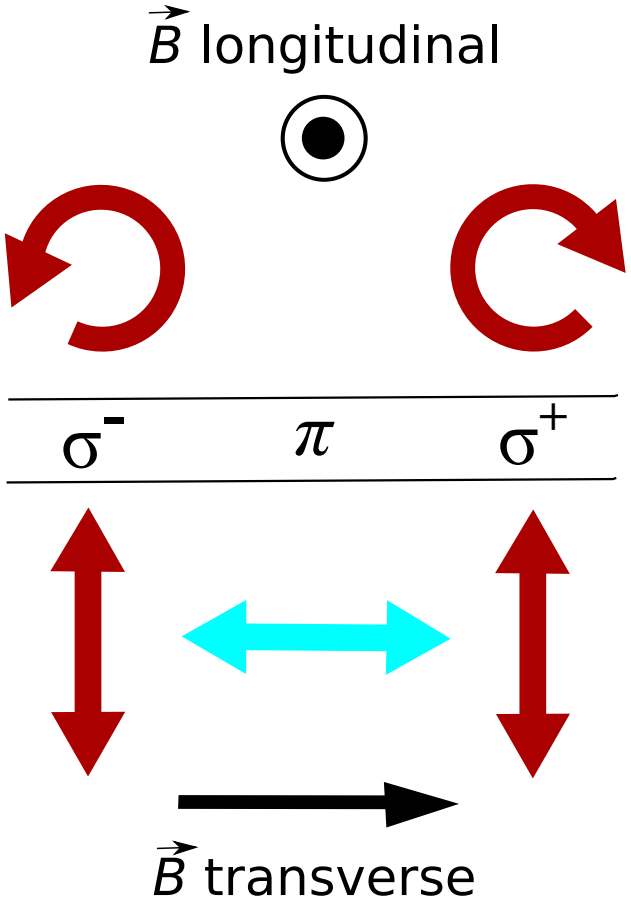

Figure 13 – Polarisation states of the Zeeman multiplett for observation parallel and perpendicular to the magnetic Field [10].

So far the polarisation states of the Zeeman multiplett were only described as observed parallel and perpendicular to the magnetic field. For the diagnostic geometry at ASDEX Upgrade, the H_α-Zeeman emission from the plasma edge is not observed parallel or perpendicular. Therefore a more general description of the polarisation states is needed. For an observer with line-of-sight in $\vec{d}_z$-direction the angle γ is defined as angle between $\vec{d}_z$ and magnetic field $\vec{B}$. In a fixed normalised Cartesian coordinate system (see Figure 14) with $\vec{d}_x \times \vec{d}_y = \vec{d}_z$ the polarisation angle β is the projection of the magnetic field vector $\vec{B}$ onto the plane generated by $\vec{d}_x$ and $\vec{d}_y$. In general there is a degree of freedom of defining the polarisation angle, because the coordinate system can be rotated around $\vec{d}_z$, but relative to the polarisation plane of the observed light wave . To make polarisation angles comparable a fixed reference frame must be chosen, which means that also $\vec{d}_x$ and $\vec{d}_y$ have fixed directions [21].

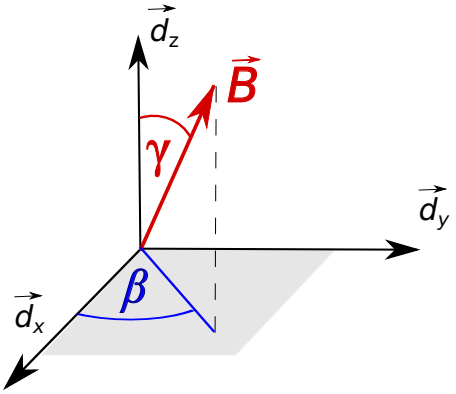

Figure 14 – Definition of the coordinate system for an observer with line of sight in direction $\vec{d}_z$ [21]

The angle γ and the polarisation angle β can then be calculated using the following vector identities:

$$\cos(\gamma) = \frac{\vec{B} \cdot \vec{d}_z}{|\vec{B}|} \qquad \tan(\beta) = \frac{\vec{B} \cdot \vec{d}_x}{\vec{B} \cdot \vec{d}_y} \tag{29}$$

To describe the response of polarimetric measurements to the H_α Zeeman multiplett, it is useful to describe the polarisation states of the different Zeeman components with Stokes vectors. The Stokes vectors can be calculated with following formulas [21, 22]:

$$s^\pi = I^\pi \begin{pmatrix} \sin^2(\gamma) \\ s_1 \\ s_2 \\ 0 \end{pmatrix} \qquad s^{\sigma^\pm} = I^{\sigma^\pm} \begin{pmatrix} 1 + \cos^2(\gamma) \\ -s_1 \\ -s_2 \\ \mp s_3 \end{pmatrix} \tag{30}$$

In formula (30) $2I^{\sigma^\pm} = I^\pi$ are component irradiances and stokes parameter are defined by $(s_1, s_2, s_3) = (\sin^2(\gamma)\cos(2\beta), \sin^2(\gamma)\sin(2\beta), 2\cos\gamma)$. Observing each of the Zeeman components separately, the component is fully polarised. If the entire Zeeman multiplett is observed together ignoring wavelength the resulting light is unpolarised, which is the same as for the MSE multiplett. In following ratio between linear and circular polarised parts of the different Zeeman

components are explained more in detail. The π-component has only linear polarisation, but is fully polarised, so the degrees of polarisation are $p^{\pi}_{tot} = p^{\pi}_{lin} = 1$ and $p^{\pi}_{circ} = 0$. The σ-components are also fully polarised $p^{\sigma^{\pm}}_{tot} = 1$, but the ratio of linear and circular polarisation changes with γ. This is illustrated in figure 15.

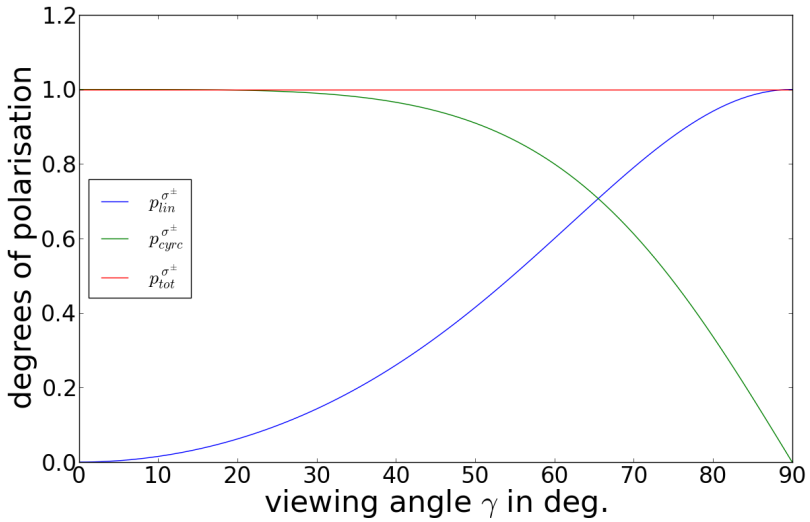

Figure 15 – Degree of polarisation and ratio of linear and circular polarised part for a σ-component depending on viewing angle to the magnetic field γ.

For $0° < \gamma < 90°$ the $\sigma^{\pm}$-components are elliptically polarised. Since the angle γ determines the ratio between the linear and the circular polarised part, it is directly related to the ellipticity χ of the polarisation state. The conversion between both angles is given by the following relation:

$$\tan(2\chi^{\pm}) = \frac{\mp 2\cos(\gamma)}{\sin^2(\gamma)} \tag{31}$$

4.3 Emergence of Zeeman H_α emission at the plasma edge

The main information required for this thesis from atomic processes in the plasma is the spatial distribution of excited hydrogen particles in the plasma edge, since this is important for the development of a forward model later. The Zeeman-split H_α emission in the plasma edge is mainly caused by the recycling of hydrogen atoms from the plasma. Due to different transport mechanisms is the plasma like anomalous transport the hydrogen ions drift into the direction of the plasma edge, where the electron temperature T is lower. In this region they become neutralised by electron capture on and near the wall or limiter, where they slow done and then drift slowly back inside the plasma. There they are ionised and rejoin. Due to the high temperature in the center, the plasma is fully ionised and the density of neutral hydrogen particles n_H vanishes, so no emission from bounded electrons is possible in that region. Near the wall or limiter, the ion density n_i and the electron density n_e decrease due to decreasing electron temperature T_e and the neutral particle density n_H increases (see Figure 16). The main excitation mechanism for the hydrogen neutrals are collisions. Since the particles in the limiter shadow or near the wall are very slow, collision rates are small and therefore also the density of excited neutral

hydrogen atoms n_{H^*}. Both effects together explain, why the H_α emission has its maximum in a small layer close to the last close flux surface and in the middle between plasma edge and wall. For observation of H_α-edge emission near the limiter (see Figure 37) the distribution of n_{H^*} is different. For this case, the density of excited hydrogen particles n_{H^*} is maximal for a position very close to the limiter, where the density decreases dramatically in a very narrow layer. This is caused by a high collision rate due to the high electron density n_e and temperature T_e in front of the limiter [23, 24].

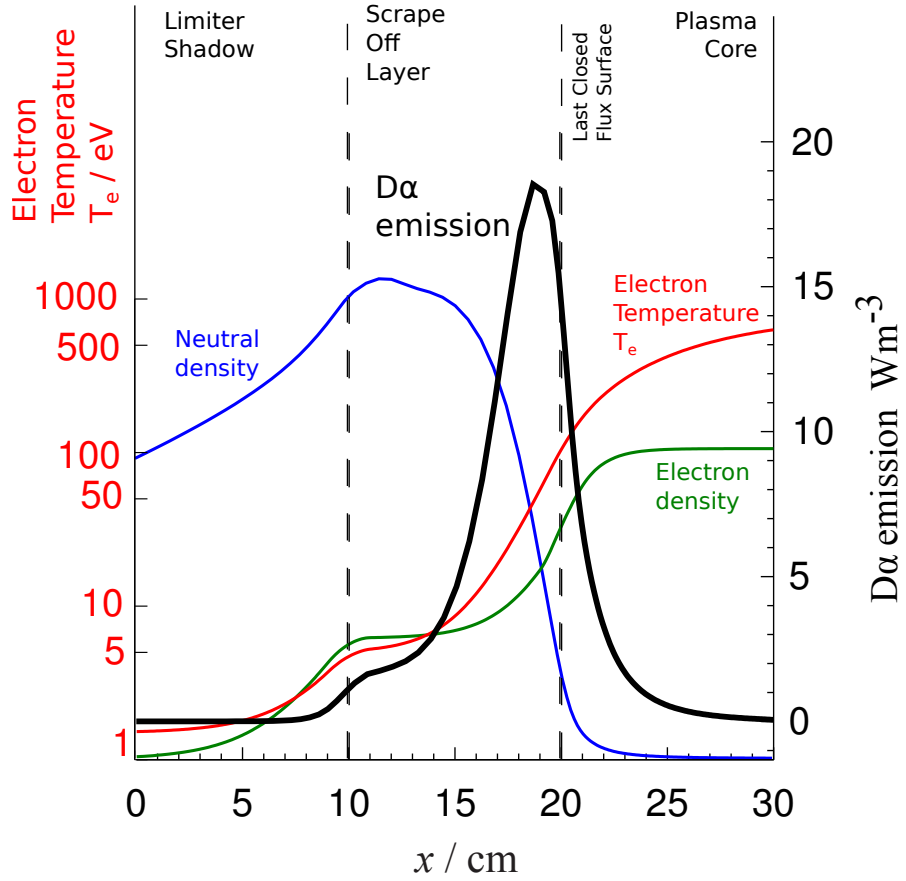

Figure 16 – Plasma cross section plot for intensity of D_α-emission, neutral density, electron density and electron density [24].

5 Standard IMSE-Diagnostic

After the description of the relevant basics in polarisation optics and the standard MSE-diagnostic, this chapter explains the measuring principle of the new IMSE-system. Therefore the basic components of the IMSE-diagnostics will be explained followed by the mathematical description of the system. This also includes the response of the IMSE-diagnostic to the MSE-spectrum and the main features of data evaluation. Based on the mathematical characterisation of the IMSE-diagnostic in this chapter, a theoretical description of the response of the IMSE-system to the Zeeman edge emission can be derived later.

5.1 IMSE-Setup and measuring principle

In chapter 3 it was described that the measurement of the entire MSE-multiplett from the neutral-beam emission with a normal polarimeter leads to no results, since the polarisation integral of the MSE-spectrum over wavelength is always unpolarised. Therefore, a normal MSE-diagnostic requires narrow spectral filters to extract the polarisation state of the individual MSE-components. Since the MSE-spectrum changes along the neutral beam due to Doppler shift and changes of magnetic field each spatial data point needs different filters and a separate calibration. In addition with the need of several electrical devices for each spatial point this leads to high costs and a severe limitation of data points.
To avoid this problem the IMSE-System was invented, which is a modified version of a simple imaging polarimeter. It can measure the line-integrated polarisation information of an entire two-dimensional data array in one measurement. The number of data point for this system is then mainly limited by the fringe resolution, which is approximately 1/6 CCD-camera resolution. The camera has 240 times 320 pixel. To understand the measuring principle of the IMSE-system, it is useful to explain a simple imaging polarimeter first. The simple polariser consists of a displacer plate and a polariser, which are placed between two lenses. The schematic setup of simple polariser is illustrated in Figure 17.

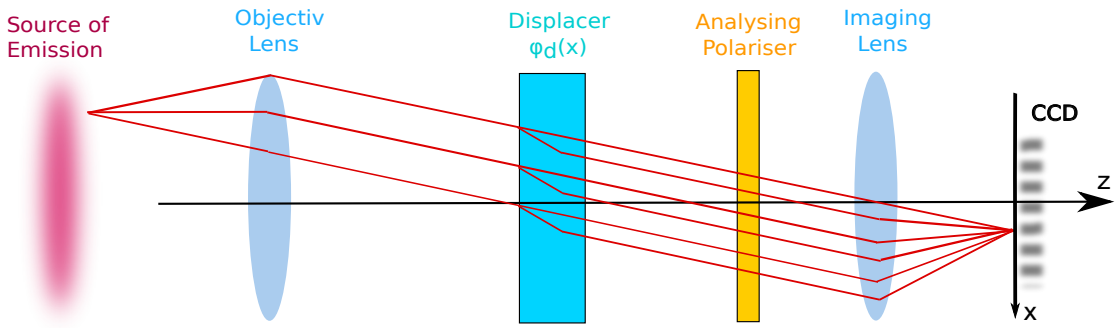

Figure 17 – Schematic setup of a simple imaging polariser

The displacer is a birefringent plate introducing a phase delay $\phi_D(x)$ between the ordinary and the extraordinary wave. This phase delay depends on the incident angle of the incoming wave to the plate. Since the incident angle is different for each viewing direction the phase delay is changing across the plate in one direction (defined as x-direction). The polariser transforms this phase delay change to an interference pattern, which is recorded by a CCD-camera. The polarisation angle θ of the incident light changes the ratio of the ordinary and extraordinary wave and so effect the amplitude $I \propto 1 + \cos(2\theta)$ of the resulting fringes (i.e. oscillations along across the image). The polarisation information is then encoded in the amplitude of the fringes, which proceed across the image in x-direction. The number of fringes mainly depend on the thickness of the displacer plate. The number of fringes are important, because they also determine the resolution of the measurement. Only if the variation of the polarisation across the image is small against the fringes oscillation, the imaging polarimeter has a sufficient resolution.
Measuring the entire MSE-spectrum from the neutral-beam emission with such a simple polarimeter, the total interference pattern would vanish, since the fringes of the σ-component and the π-components interfere destructively (i.e. having a phase difference of 180°), see Figure 18 (left). This reflects the fact, that the entire MSE-multiplett is unpolarised.

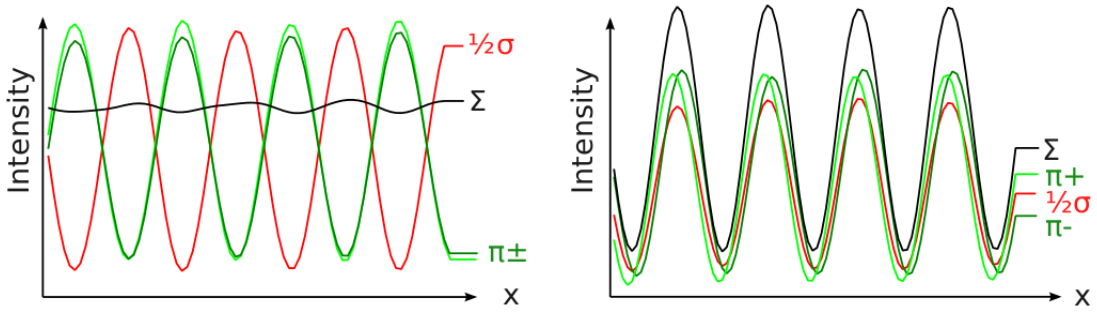

Figure 18 – Test measurements for the fringes in x-direction of the entire MSE-multiplett:
Left: contructive interference of the fringes for a setup without delay plate
Right: constructive interference due to phase delay from used delay plate [25]

For the standard MSE-diagnostic a spectral discrimination of the several components is achieved by using different narrow interference filters. For the IMSE-system spectral discrimination is achieved by implementing a delay plate between the displacer and the polariser in the setup of a simple imaging polarimeter. This plate introduces a phase delay ϕ_W to each incoming waves, which depends on the wavelength and the thickness of the plate, but is approximately constant across the image. As a result the phase difference of the fringes introduced from the σ-component and the π-components shifted relative to each other. Choosing the correct delay plate would reduce the phase difference to zero and the fringes then interfere constructively, see Figure 18 (right). For this the delay-plate has to meet essential requirements. It needs to be relatively thick, so that the absolute phase delay is in order of thousands wavelengths. Only in this case is the dependence of the fringe phase on the wavelength sufficiently large. Secondly choosing a suitable plate thickness with regard to the wavelength difference of the MSE-components will shift the phase difference between the σ-component and the π-components to achieve constructive interference. This is one reason the diagnostic is optimized to measure the MSE-spectrum.

The Zeeman H_α emission has a different energy splitting and circular polarised fractions, so the IMSE-system may give a different response. Since the MSE-spectrum in general is more complex than described by only three superior components, a thick delay plate reduces the amplitude of the fringes by an unknown factor ξ due to interference of the MSE sub-levels. The factor ξ is denoted as spectral contrast and is an unknown quantity, which must be eliminated. To separate the polarisation information from the spectral contrast a second displacer is added between the objective lens and the displacer in a way to produce a phase delay $\phi_S(y)$ in y-direction and therefore fringes, which are orthogonal to the former fringes. To avoid a perturbation of the optimized phase difference between the fringes, this displacer is not allowed to introduce a net phase delay, which is constant over the image. Such a special displacer is named a Savart plate and practically consists of two displacer plates with orthogonal orientated optical axes.
An facultative optical component in the IMSE-system is the ferroelectric-liquid crystal plate (FLC-plate) located between objective lens and Savart plate. The optical property of this plate is the same as a quarter-wave plate, but its optical axis can be switched by applying a voltage. If the FLC-plate is switched off, it does not change the physical principle of the IMSE-diagnostic. In the activated case the FLC-plate can be used to measure small ellipticity effects of the MSE-polarisation that might lead to deviations of the polarisation angle.

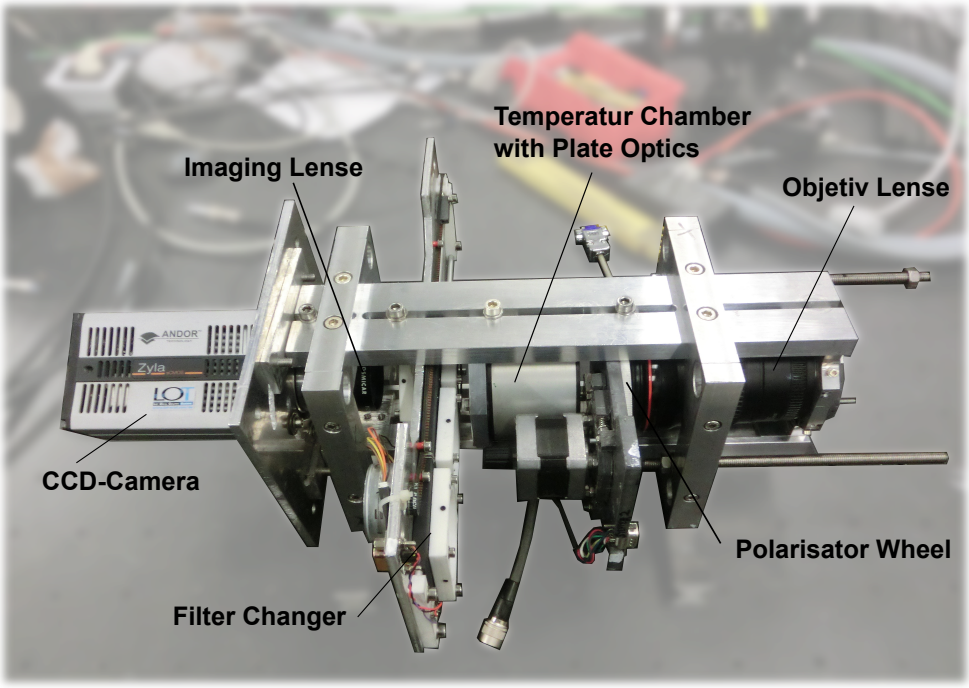

Figure 19 – Photo of the IMSE-System

A photo of the IMSE-Setup is shown in Fig. 19. All optical plates are fixed in a closed metal chamber. An external controllable heating system is used to stabilise the temperature within the chamber and so the optical properties of the optics and especially of the FLC-plate. Different types of filter can be fixed in the filter changer and changed via software control. Measuring the MSE-spectrum a filter is used to suppress perturbing emission from charge-exchange transitions

and from the plasma edge. For the Zeeman H_α edge-emission another filter is required. The polarisation wheel has partly simple a hole for normal measurement and another hole with a polariser film. Its function is to measure the intrinsic contrast of the system leading to derivations of the polarisation angle. This effect is a result of small, but for high accuracy important variation, of the Savart plates thickness and of surface irregularities. All of these technical components of the IMSE-system are built into a stable metal construction, that can be applied on the MSE-port at ASDEX Upgrade [25–27]. In the next section the entire MSE-system will be described mathematically.

5.2 Mathematical description of the IMSE-diagnostic

The following section will give the entire mathematical description of the IMSE-system. The first part of the calculation is identical for the MSE- and the Zeeman-spectrum. However, it is important to understand this calculation to derive the response for the several spectra later and to make sure that all approximations are still valid for the general case. The figure 20 illustrates schematically the setup of the IMSE-System with the important optical components needed to consider the full characterisation of the IMSE-system.

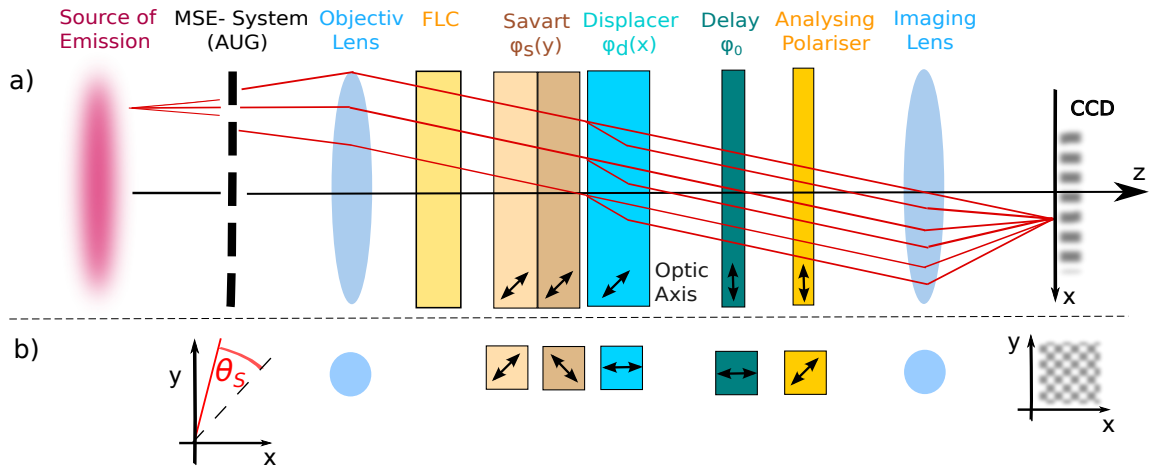

Figure 20 – Schematic setup of the IMSE-System including optic axis orientation [26]:
a) View from above with optical axis orientation relative to the plate surface
b) View in z-direction with orientation of the optical axis relative to the (x,y)-plane

Definition of the system coordinates for the IMSE-system

The systems coordinates x and y are defined in the orientation of the CCD-Camera. The notation of the corresponding polar coordinates is (R_I, δ_I) with $\delta_I = 0°$ orientated in x-direction. Knowing the focal length of the imaging lens $f_i = 50$ mm and the pixel size on the CCD-camera (Δx = Δy = 19.8 µm), R_I can be substituted by the incident angle α_I with following relations:

$$\begin{aligned} x &= \cos(\delta_I)\ R_I = \cos(\delta_I)\ \sin(\alpha_I)\ f_i \\ y &= \sin(\delta_I)\ R_I = \sin(\delta_I)\ \sin(\alpha_I)\ f_i \end{aligned} \tag{32}$$

The calculated values of the angles α_I and δ_I for the CCD-camera are shown in figure 21.

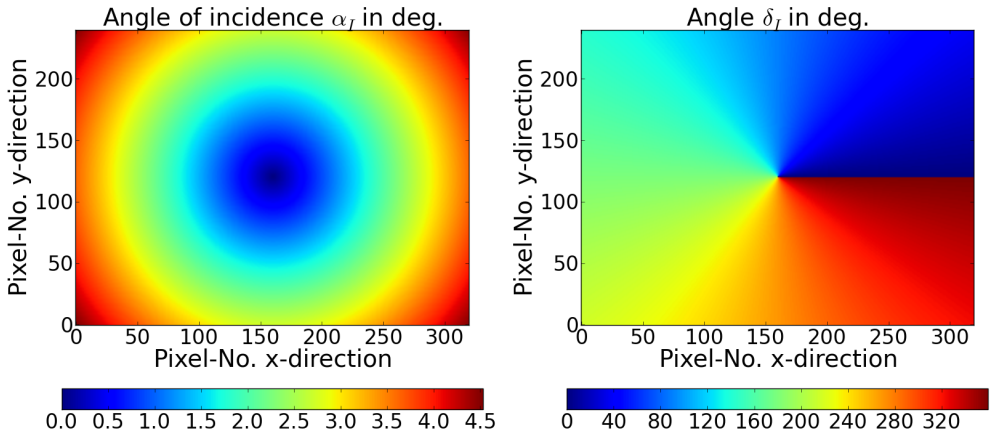

Figure 21 – Calculated values of the incident angle (left) and of the system angle (right) for the 320 × 240 pixel of the CCD-camera

The IMSE-System measures polarisation relative to the Savart-plate, that is rotated 45° anti-clockwise relative to (x,y). Therefore, it is reasonable to define the polarisation angle θ_S of the incoming light in such a way that $\theta_S = 0°$ is aligned in (x+y)-direction (see Fig. 20b).

Calculation of the IMSE image equation

The response of the IMSE-System to arbitrarily polarised light with a single wavelength λ can be described by using the Stokes-Müller formalism (section 3.1). Each optical element is denoted by a Müller matrix $\mathbf{M}$ and the polarisation state of the input light is given by the Stokes vector $\vec{s}$. The orientations of the plates optical axes are:

1. FCL plate at $\theta_S = 0°$ (FLC-Off) or $\theta_S = -45°$ (FLC-On)
2. Savart plate with thickness $L_S = 7.6$ mm at $\theta_S = 0°$ introducing phase delay ϕ_S
3. Displacer plate with thickness $L_D = 5.4$ mm at $\theta_S = -45°$ with phase delay ϕ_D
4. Delay plate with thickness $L_W = 1.2$ mm at $\theta_S = -45°$ gives phase delay ϕ_W
5. Polariser at $\theta_S = 0°$

The displacer plate and the delay plate have the same orientation relative to θ_S and are directly adjecent in the IMSE-system. They can be denoted together by one Müller matrix:

$$\mathbf{M}(-45°, \phi_W + \phi_D) = \mathbf{M}(-45°, \phi_W) \cdot \mathbf{M}(-45°, \phi_D) \tag{33}$$

The entire description of the IMSE-System in Stokes-Müller formalism is then given by matrix multiplication of the Müller matrices for the single components. $\vec{S}$ is the stokes vector after the light with polarisation state $\vec{s}$ has passed the complete system. The complete equation for the entire IMSE-system is:

$$\vec{S} = \mathbf{M}^P_{Polariser}(0°) \cdot \mathbf{M}^D_{Displacer+Delay}(-45°, \phi_W + \phi_D) \cdot \mathbf{M}^D_{Savart}(0°, \phi_S) \cdot \mathbf{M}^D_{FLC} \cdot \vec{s} \tag{34}$$

To include different settings of the FLC-plate to the theoretical description, the Stokes vector $\hat{\vec{s}}$ is introduced. $\hat{\vec{s}}$ gives only the response of the FLC-plate to the input stokes vector $\vec{s}$ and is defined as follows:

$$\hat{s} = \mathbf{M}_{FLC}^{D} \cdot \vec{s} \tag{35}$$

The different modi of the FLC-plate are represented by the following Müeller matrices,

$$\mathbf{M}_{FLC}^{No} = \begin{pmatrix} 1 & 0 & 0 & 0 \\ 0 & 1 & 0 & 0 \\ 0 & 0 & 1 & 0 \\ 0 & 0 & 0 & 1 \end{pmatrix} \quad \mathbf{M}_{FLC}^{Off} = \begin{pmatrix} 1 & 0 & 0 & 0 \\ 0 & 1 & 0 & 0 \\ 0 & 0 & 0 & 1 \\ 0 & 0 & -1 & 0 \end{pmatrix} \quad \mathbf{M}_{FLC}^{On} = \begin{pmatrix} 1 & 0 & 0 & 0 \\ 0 & 0 & 0 & -1 \\ 0 & 0 & 1 & 0 \\ 0 & 1 & 0 & 0 \end{pmatrix} \tag{36}$$

where $\mathbf{M}_{FLC}^{No}$ means, that the FLC-plate is removed from the IMSE-system. The matrices $\mathbf{M}_{FLC}^{Off}$ and $\mathbf{M}_{FLC}^{On}$ are describing the switched off and the switched on modi.

Considering the Müller matrices of the different IMSE-components and using the introduced FLC-plate notation, equation 34 ca be rewritten as:

$$\vec{S} = \frac{1}{2} \begin{pmatrix} 1 & 1 & 0 & 0 \\ 1 & 1 & 0 & 0 \\ 0 & 0 & 0 & 0 \\ 0 & 0 & 0 & 0 \end{pmatrix} \begin{pmatrix} 1 & 0 & 0 & 0 \\ 0 & \cos(\phi_W + \phi_D) & 0 & \sin(\phi_W + \phi_D) \\ 0 & 0 & 0 & 0 \\ 0 & -\sin(\phi_W + \phi_D) & 1 & \cos(\phi_W + \phi_D) \end{pmatrix} \begin{pmatrix} 1 & 0 & 0 & 0 \\ 0 & 1 & 0 & 0 \\ 0 & 0 & \cos(\phi_S) & \sin(\phi_S) \\ 0 & 0 & -\sin(\phi_S) & \cos(\phi_S) \end{pmatrix} \begin{pmatrix} \hat{s_0} \\ \hat{s_1} \\ \hat{s_2} \\ \hat{s_3} \end{pmatrix} \tag{37}$$

The CCD-camera measures only absolute intensity. The intensity on the CCD-camera is given by the intensity component of the resulting Stokes vector $S_0 = I_{Image}$. The resulting equation is called image equation of the IMSE-system, where all phase delay and all four Stokes parameter are a function of the system coordinates x and y:

$$\begin{aligned} 2I_{Image} = \hat{s_0} \quad &+ \quad \hat{s_1} \cos(\phi_W + \phi_D) \\ &- \quad \hat{s_2} \sin(\phi_W + \phi_D) \sin(\phi_S) \\ &+ \quad \hat{s_3} \sin(\phi_W + \phi_D) \cos(\phi_S) \end{aligned} \tag{38}$$

Calculation of phase delay for the IMSE-plates

To calculate the phase delays of the individual plates, equation (21) is used. The incident angle α_I on the plates is lower than 5° across the image (see Fig. 21), so terms in order of $\sin^2(\alpha_I)$ will be ignored. Operating in air the refractive index of the surrounding media is $n_M = 1$, and therefore equation (21) simplifies to:

$$\phi = \frac{2\pi L}{\lambda} \left(n_O - \frac{n_O \; n_E}{\sqrt{S_V}} + \frac{n_O^2 - n_E^2}{S_V} \; \sin(\rho)\cos(\rho)\cos(\delta_I)\sin(\alpha_I) \right) \tag{39}$$

All birefringent plates of the IMSE-system are made of α-barium borate (αBBO). The refractive indices of αBBO for the ordinary and the extraordinary wave are a function of the wavelength λ. In the small wavelength ranges for MSE- and H_α edge-emission, the refractive indices can

be assumed as constant values with $n_O = 1.666$ and $n_E = 1.549$ [28]. In the case of $\Delta N = n_O - n_E << n_O, n_E$ it is possible to approximate the constant term (i.e. independent of α_I) in Equation (39):

$$\phi = \frac{2\pi L}{\lambda}\left(\frac{\Delta N}{2} + \frac{n_0^2 - n_E^2}{S_V}\ \sin(\rho)\cos(\rho)\cos(\delta_I)\sin(\alpha_I)\ \right) \tag{40}$$

The delay plate with has the optical axes parallel to the plate surface ($\rho = 0°$), therefore it introduces a constant phase delay ϕ_W, whereas the displacer plate ($\rho = 45°$) causes an incident angle dependent phase delay ϕ_D. The phase delays of the displacer plate and the delay plate are:

$$\phi_W = \frac{2\pi L_W}{\lambda}\left(\frac{\Delta N}{2}\right) \tag{41}$$

$$\phi_D = \frac{2\pi L_D}{\lambda}\left(\frac{\Delta N}{2} + \frac{n_O^2 - n_E^2}{n_0^2 + n_E^2}\ \cos(\delta_I)\sin(\alpha_I)\ \right) \tag{42}$$

The Savart plate consists of two displacer plates ($\rho = 45°$) of the same thickness $\frac{L_S}{2}$ and with orthogonal orientated optical axes, i.e. one lies at $\delta_I + 45°$ and the other at $\delta_I - 45°$. The second plate is assumed to add a negative phase delay. Contrary to the single displacer plate the Savart plate gives no constant phase delay and for a wave with perpendicular incident ($\alpha_I = 0°$) it introduces no delay at all. The phase delay of the Savart plate is given by:

$$\begin{aligned}\phi_S = &\frac{2\pi\frac{L_S}{2}}{\lambda}\left(\frac{\Delta N}{2} + \frac{n_0^2 - n_E^2}{n_0^2 + n_E^2}\ \cos\left(\delta_I - \frac{\pi}{4}\right)\sin(\alpha_I)\ \right) \\ &-\frac{2\pi\frac{L_S}{2}}{\lambda}\left(\frac{\Delta N}{2} + \frac{n_0^2 - n_E^2}{n_0^2 + n_E^2}\ \cos\left(\delta_I + \frac{\pi}{4}\right)\sin(\alpha_I)\ \right)\end{aligned} \tag{43}$$

A short rearranging of equation 43 results in the following total phase delay for the Savart plate:

$$\phi_S = \frac{2\pi L_S}{\sqrt{2}\lambda}\left(\frac{n_0^2 - n_E^2}{n_0^2 + n_E^2}\ \sin(\delta_I)\sin(\alpha_I)\ \right) \tag{44}$$

Replacing the wavelength λ by the frequency ω, the vacuum light velocity c with $\lambda\omega = 2\pi c$ and using the geometrical relations in equation (32), the phase delays can be expressed as directly proportional to the system coordinates x and y:

$$\phi_S = c_\alpha \omega y \qquad (\phi_W + \phi_D) = c_\beta \omega x + c_\gamma \omega \tag{45}$$

This is only true, when second-order terms of the incident angle are ignored. Taking the second-order term into account would only lead to a negligible dependence of the phase delay in second-order of x and y (see Fig. 22).

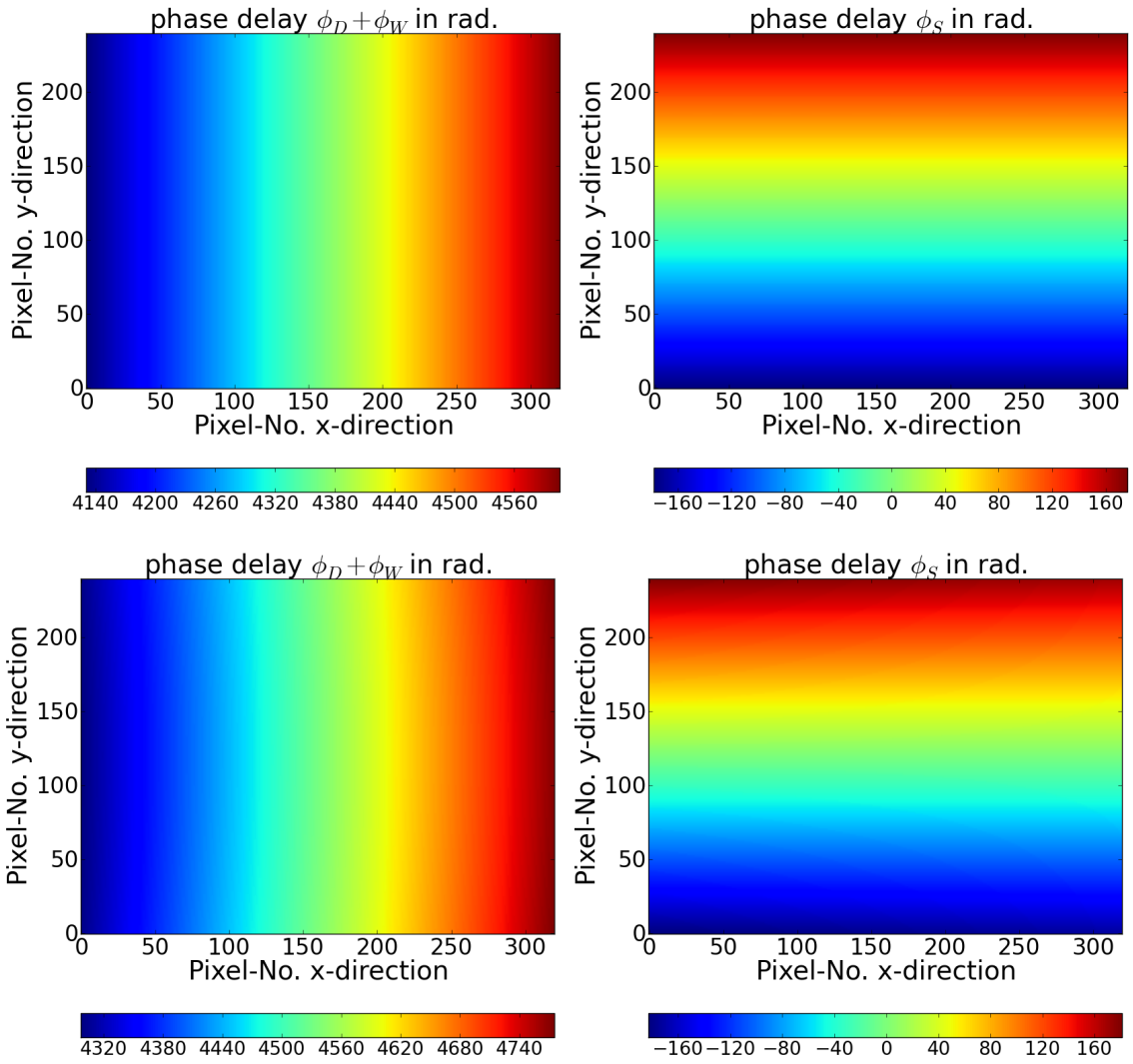

Figure 22 – Calculation of the phase delays as example for H_α-emission ($\lambda = 656.28$ nm):
- Upper part: phase delay with use of system specific constants ignoring second-order of incident angle
- Lower part: phase delay without approximations including second-order of incident angle

The prefactors in the phase delay terms in equations (41), (42) and (44) are collected in the three specific system constants c_α, c_β and c_γ with $N^2 = (n_0^2 - n_E^2)/(n_0^2 + n_E^2)$:

$$\begin{aligned} c_\alpha &= \frac{L_S\ N^2}{\sqrt{2}\ c\ f_i} = 2.6 \cdot 10^{-11} \\ c_\beta &= \frac{L_D\ N^2}{c\ f_i} = 2.6 \cdot 10^{-11} \\ c_\gamma &= \frac{\Delta N}{c}\left(L_W + \frac{1}{2}L_D\right) = 1.5 \cdot 10^{-12} \end{aligned} \tag{46}$$

The complete image equation (38) for a single wavelength or frequency ω with substituted phase delays and introduced system constants can be written as:

$$\begin{aligned} 2I_{Image}(\hat{\vec{s}},\omega) = \hat{s_0} &+ \hat{s_1}\cos(c_\beta\omega x + c_\gamma\omega) \\ &- \hat{s_2}\sin(c_\beta\omega x + c_\gamma\omega)\sin(c_\alpha\omega y) \\ &+ \hat{s_3}\sin(c_\beta\omega x + c_\gamma\omega)\cos(c_\alpha\omega y) \end{aligned} \tag{47}$$

$$\begin{aligned} = \hat{s_0} &+ \hat{s_1}\cos(\omega(c_\beta x + c_\gamma)) \\ &+ \frac{1}{2}\hat{s_2}\cos(\omega(c_\beta x + c_\gamma + c_\alpha y)) \\ &- \frac{1}{2}\hat{s_2}\cos(\omega(c_\beta x + c_\gamma - c_\alpha y)) \\ &+ \frac{1}{2}\hat{s_3}\sin(\omega(c_\beta x + c_\gamma + c_\alpha y)) \\ &+ \frac{1}{2}\hat{s_3}\sin(\omega(c_\beta x + c_\gamma - c_\alpha y)) \end{aligned} \tag{48}$$

This section introduced the theoretical description leading to the interference pattern on the CCD-camera. The following section explains how the polarisation information can be extracted from the measured interference image during the data evaluation process.

5.3 Principle of evaluation of the polarisation information from IMSE measurements

As long as the fringe oscillations along the picture are very fast in comparison to the change of the stokes components, it is possible to extract the stokes components (and so the polarisation angle) from the image. Therefore a two-dimensional Fourier transformation is applied to the IMSE image. In the general case, the Fourier image of the IMSE interference pattern shows seven Fourier components, since the image equation can be expressed as sum of seven different complex exponential functions as written in following equation, where 0 and $\pm$ characterises the sign of the dependence of Fourier component I(x,y) to the coordinates x and y. For example $I(+,-)$ is the Fourier component proportional to the exponential function $e^{i(x-y)}$.

$$I_{Image} = I(0,0) + I(+,0) + I(-,0) + I(+,+) + I(+,-) + I(-,+) + I(+,+) \tag{49}$$

An example for an Fourier image with the sever Fourier components is illustrated in Figure 23 (right). The seven Fourier components then are given by the following relations:

$$\begin{aligned} I(0,0) &= \frac{1}{2}\hat{s_0} \\ I(\pm,0) &= \frac{1}{4}\hat{s_1}e^{i\omega(\pm c_\beta x \pm c_\gamma)} \\ I(\pm,\pm) &= \frac{1}{8}(\hat{s_2} \mp i\hat{s_3})e^{\pm i\omega(c_\beta x + c_\gamma + c_\alpha y)} \\ I(\pm,\mp) &= -\frac{1}{8}(\hat{s_2} \pm i\hat{s_3})e^{\pm i\omega(c_\beta x + c_\gamma - c_\alpha y)} \end{aligned}$$

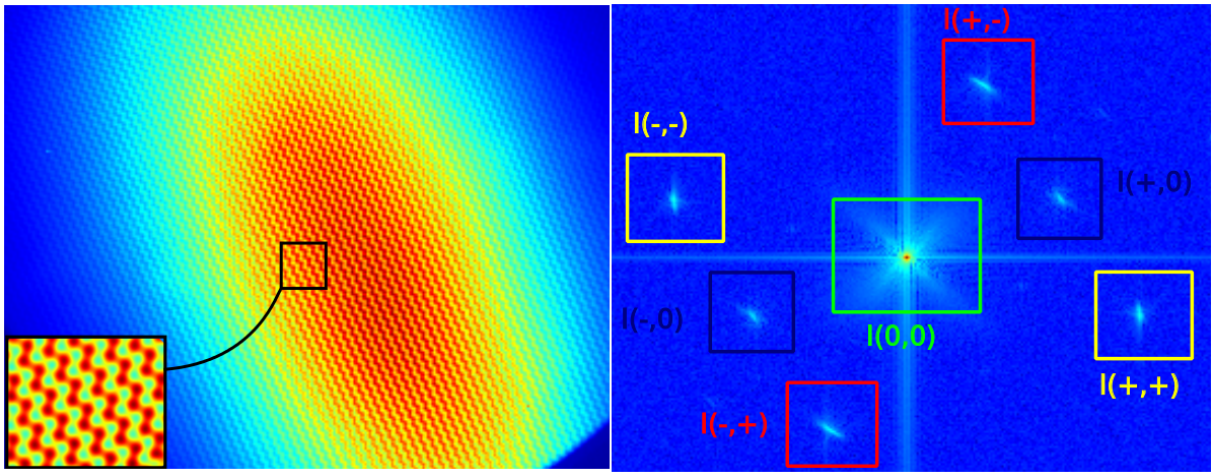

Figure 23 – IMSE image with fringes from measured neutral beam emission (left) and example of a Fourier image with the seven Fourier components (right). [14].

Cutting out a Fourier component in the Fourier image and applying the inverse two-dimensional Fourier transformation results in a two-dimensional, in general imaginary, array containing the information of the one Fourier component across the entire image. Taking the absolute value gives the real amplitude of this component, which is independent of the frequency ω. The amplitudes of the Fourier components can be calculated by $|I(x,y)| = \sqrt{I^*(x,y)I(x,y)}$ resulting in:

$$\begin{aligned} |I(0,0)| &= \frac{1}{2}|\hat{s_0}| \\ |I(\pm,0)| &= \frac{1}{4}|\hat{s_1}| \\ |I(\pm,\pm)| = |I(\mp,\mp)| &= \frac{1}{8}\sqrt{\hat{s_2}^2 + \hat{s_3}^2} \end{aligned} \tag{50}$$

The frequency independence is important especially for measuring the MSE-multiplett, since due to the Doppler-shift the wavelength is not fixed and in general not accurately known. For the IMSE-system without FLC-plate ($\hat{s_2} = s_2$ and $\hat{s_3} = s_3$) and with off-switched FLC-plate ($\hat{s_2} = s_3$ and $\hat{s_3} = -s_2$) the amplitudes are identical, so the general measuring principle is not influenced by the FLC-plate. For measuring emission with only a single frequency a separation of s_2 and s_3 is impossible without the FLC-plate, but if the measured light is fully linear polarised ($\chi = 0$ and $s_3 = 0$) or has only negligible ellipticity, the polarisation angle relative to the Savart plate can be achieved using the following relation:

$$\tan 2\theta_S = \frac{|s_2|}{|s_1|} = \frac{2|I(+,+)|}{|I(+,0)|} \tag{51}$$

Switching the FLC-plate on ($\hat{s_1} = -s_3$ and $\hat{s_3} = s_1$) allows to measure the absolute value of the ellipticity independently from the polarisation angle.

$$|\tan 2\chi| = \frac{\sqrt{s_1^2 + s_2^2}}{|s_3|} = \frac{2|I(+,+)|}{|I(+,0)|} \tag{52}$$

If during a measurement the FLC-plate switches faster on than the polarisation state can change significantly in time, a measurement of θ_S for an arbitrary polarisation state is possible by eliminating the ellipticity during the data evaluation, allowing a complete measurement of $\vec{s}$.

5.4 Response of the IMSE-System to the MSE multiplett

Until now the response of the IMSE-system to arbitrarily polarised light of a single wavelength was described mathematically. For the response of the system to the entire MSE-spectrum the calculation will be extended to several wavelength. To describe the characteristic response of the IMSE-system to the MSE-spectrum it is sufficient to neglect the complexity of the MSE-spectrum (see figure 8) and consider only the three superordinate MSE-components. Determining the central σ-component to have frequency $\omega^\sigma = \omega_0$ and the polarisation angle θ_S, the two lateral $\pi^\pm$-components can be denoted with the frequencies $\omega^{\pi^\pm} = \omega_0 \pm \Delta\omega$ and the polarisation angle $\theta_S + 90°$. The stokes vectors of the simplified MSE-multiplett with parameters $(s_1, s_2, s_3) = (\cos(2\theta_S), \sin(2\theta_S), 0)$ are:

$$s^\sigma = I^\sigma \begin{pmatrix} 1 \\ s_1 \\ s_2 \\ s_3 \end{pmatrix} \qquad s^{\pi^\pm} = \tfrac{1}{2} I^\pi \begin{pmatrix} 1 \\ -s_1 \\ -s_2 \\ -s_3 \end{pmatrix} \tag{53}$$

Since the $\pi^\pm$-components of the MSE-spectrum are entirely linear polarised the Stokes vectors s^{π^+} and s^{π^-} are identical ignoring possible intensity variations e.g. due to filters. In general the σ-component can show very small ellipticity which is ignored as it does for not influence the results fundamentally. The image on the CCD-camera is the sum of the images for each of the three MSE-components, since the phase of single emission events from different MSE-components are statistically independent with random pahse. The total image-equation for the MSE-multiplett can be simply calculated using the trigonometric addition theorems. The result is the following image equation for the MSE-multiplett:

$$\begin{aligned} 2I^{MSE}_{Image} &= 2I_{Image}(\hat{s}^\sigma, \omega_0) + 2I_{Image}(\hat{s}^{\pi^-}, \omega_0 - \Delta\omega) + 2I_{Image}(\hat{s}^{\pi^+}, \omega_0 + \Delta\omega) \\ &= I^\sigma + I^\pi \\ &+ \hat{s_1}\xi_0 \ \cos(\omega_0(c_\beta x + c_\gamma)) \\ &+ \frac{1}{2}\hat{s_2}\xi_+ \cos(\omega_0(c_\beta x + c_\gamma + c_\alpha y)) - \frac{1}{2}\hat{s_2}\xi_- \cos(\omega_0(c_\beta x + c_\gamma - c_\alpha y)) \\ &+ \frac{1}{2}\hat{s_3}\xi_+ \cos(\omega_0(c_\beta x + c_\gamma + c_\alpha y)) + \frac{1}{2}\hat{s_3}\xi_- \cos(\omega_0(c_\beta x + c_\gamma - c_\alpha y)) \end{aligned} \tag{54}$$

The total image-equation is similar to the image-equation (48) for a single wavelength with factors ξ_0, ξ_- and ξ_+.

These are the spectral contrast defined as follows:

$$\begin{aligned} \xi_0 &= I^\sigma - I^\pi \cos(\Delta\omega(c_\beta x + c_\gamma)) \\ \xi_+ &= I^\sigma - I^\pi \cos(\Delta\omega(c_\beta x + c_\gamma + c_\alpha y)) \\ \xi_- &= I^\sigma - I^\pi \cos(\Delta\omega(c_\beta x + c_\gamma - c_\alpha y)) \end{aligned} \tag{55}$$

For the center of the image (incident angle $\alpha_I \approx 0^\circ$ and $x, y \approx 0$) or a thin displacer and Savart plate the spectral contrast functions are approximately equal and can be reduced to the constant function ξ (independent of x and y), which is denoted as spectral nett contrast:

$$\xi = I^\sigma - I^\pi \cos(c_\gamma \Delta\omega) \tag{56}$$

The spectral nett contrast influences the signal strength of the measurement and is therefore desired to be maximal. It is optimised to the MSE-multiplett (i.e. a given $\Delta\omega$) by selecting a suitable c_γ, which is related to the thickness of the delay plate L_W (see equation (46). If the net delay is removed from the IMSE-system, c_γ an ξ are zero and the fringes for the σ- and π-components interfere destructively resulting in the vanishing of the interference pattern on the CCD-camera. For the Zeeman multiplett this optimisation is not valid, since the frequency splitting is different. As long as the MSE emission from the neutral-beam comes from atomic states with statistical population, the intensity ratio is $I^\sigma = I^\pi = 1$. A deviation from the statistical population e.g. for small neutral-beam densities, may decrease the spectral nett contrast and the absolute intensity, but the polarisation information is not strongly affected. To obtain the polarisation angle from the measured CCD-image, the demodulation of the seven Fourier components by two-dimensional Fourier transformation is again performed and leads to the following Fourier components:

$$\begin{aligned} I(0,0) &= \frac{1}{2}(I^\sigma + I^\pi) \\ I(\pm,0) &= \frac{1}{4}\xi_0 \hat{s_1} e^{i\omega(\pm c_\beta x \pm c_\gamma)} \\ I(\pm,\pm) &= \frac{1}{8}\xi_+ (\hat{s_2} \mp i\hat{s_3}) e^{\pm i\omega(c_\beta x + c_\gamma + c_\alpha y)} \\ I(\pm,\mp) &= -\frac{1}{8}\xi_- (\hat{s_2} \pm i\hat{s_3}) e^{\pm i\omega(c_\beta x + c_\gamma - c_\alpha y)} \end{aligned} \tag{57}$$

The resulting amplitudes are:

$$\begin{aligned} |I(0,0)| &= \frac{1}{2}(I^\sigma + I^\pi) \\ |I(\pm,0)| &= \frac{1}{4}\xi_0 |\hat{s_1}| = \frac{1}{4}\xi_0 |s_1| \\ |I(\pm,\pm)| &= \frac{1}{8}\xi_+ \sqrt{(\hat{s_2})^2 + (\hat{s_3})^2} = \frac{1}{8}\xi_+ |s_2| \\ |I(\pm,\mp)| &= \frac{1}{8}\xi_- \sqrt{(\hat{s_2})^2 + (\hat{s_3})^2} = \frac{1}{8}\xi_- |s_2| \end{aligned} \tag{58}$$

The argument for the influence of the FLC-plate is the same as in case of a single frequency (no FLC: $\hat{s_2} = s_2$ and $\hat{s_3} = s_3 = 0$ / FLC-Off: $\hat{s_3} = -s_2$ and $\hat{s_2} = s_3 = 0$).
For the MSE-spectrum the amplitudes $|I(\pm,\pm)|$ and $|I(\pm,\mp)|$ are slightly different due to a small asymmetry of the contrast functions. The relation between the polarisation angle θ_S and the fringe amplitudes is:

$$\tan 2\theta_S \approxeq \frac{\xi_+}{\xi_0} \cdot \frac{|s_2|}{|s_1|} = \frac{2|I(+,+)|}{|I(+,0)|} \tag{59}$$

The small difference between ξ_0 and ξ_+ results in an error of the polarisation angle depending on y. The difference of ξ_0 and $\xi_\pm$ is caused by two effects. The first is the general different dependence of the spectral contrast function on the system coordinates x and y according to equation (55). Secondly the $\xi_\pm/\xi_0$ -ratio is also effected by the intrinsic contrast of the Savart plate caused by surface irregularities. Test measurements and simple simulations have approved following relation to give more precise results for the polarisation angle, since the error increases only in second order of y.

$$\tan^2 2\theta_S \approxeq \frac{\xi_+ \, \xi_-}{\xi_0^2} \cdot \frac{|s_2|^2}{|s_1|^2} = \frac{4|I(+,+)||I(+,-)|}{|I(+,0)|^2} \tag{60}$$

Taking the entire MSE-spectrum into account only leads to small deviations of the error assumption and the spectral contrast functions whereas the fundamental principle of data evaluation remains. The response of the IMSE-system to the MSE-spectrum was well proven in numeric simulations and experiments on ADEX Upgrade and leads to errors in order of $\Delta\theta_S \approx 0.2\,^\circ$. It still remains the question of an in-situ calibration method to improve and simplify the measurement. In the next chapter the response of the IMSE-system to the Zeeman-emission is described with the aim to discuss the possibility of calibration theoretically and independently of installation on a special fusion device.

6 Theoretical description of the IMSE-system measuring the Zeeman multiplett

Since experiments have shown a measurable signal of the IMSE-system observing Zeeman split H_α-emission from the plasma edge, the question emerges if this can be used to calibrate or improve the IMSE-measurement. For a discussion of this, the following chapter will introduce a general theoretical description of the response of the IMSE-system to Zeeman-emission based in the same way of calculation as in the former chapter. The main differences are caused by the existence of non vanishing circular polarisation for the two $\sigma^{\pm}$-components and a MUCH smaller energy splitting the for the MSE-spectrum. The first section will give a theoretical description of the IMSE-system measuring Zeeman-emission. It is followed a discussion if the IMSE-system in contemporary configuration (i.e. with regard to used optical plates) is suitable for calibration. The last section investigates possibilities to optimise the IMSE-system for Zeeman calibration and MSE-measurements at the same time by changing the intrinsic system parameters.

6.1 Derivation of equations for data evaluation

In the former calculation for the MSE multiplett the Stokes vectors of the $\pi^{\pm}$-components are identical ($s^{\pi^-} = s^{\pi^+}$). This symmetry breaks for the $\sigma^{\pm}$-components of the Zeeman multiplett due to different signs of the non-vanishing ellipticity $\mp\chi$ leading to new terms in the total image-equation. Ignoring line-broadening effects, a complete description of IMSE-systems response to the Zeeman multiplett is possible, since the Zeeman multiplett only consists of three components in strong magnetic fields like in ASDEX Upgrade. The frequencies of the three Zeeman components are defined as $\omega^{\pi} = \omega_0$ and $\omega^{\sigma^{\pm}} = \omega_0 \pm \Delta\omega$. The polarisation angle for the linear π-component is defined relative to the Savart plate as θ_S. The major polarisation axis of the elliptical $\sigma^{\pm}$-components is orthogonal to the polarisation direction of the π-component and therefore has polarisation angle $\theta_S + 90°$ and the ellipticity $\mp\chi$. Since the ellipticity varies with observation direction characterised by the angle γ relative to the magnetic field, the following notation of the Stokes vectors with the Stokes parameters $(s_1, s_2, s_3) = (\sin^2(\gamma)\cos(2\theta_S), \sin^2(\gamma)\sin(2\theta_S), 2\cos\gamma)$ is used in this calculation:

$$s^{\pi} = I^{\pi} \begin{pmatrix} \sin^2(\gamma) \\ s_1 \\ s_2 \\ 0 \end{pmatrix} \qquad s^{\sigma^{\pm}} = I^{\sigma^{\pm}} \begin{pmatrix} 1+\cos^2(\gamma) \\ -s_1 \\ -s_2 \\ \mp s_3 \end{pmatrix} \tag{61}$$

The derivation of the corresponding geometry was already explained in section 4.2 and is described explicitly in [21]. To consider the possibility of filter effects and non-statistical state population the calculation starts from arbitrary intensity values I^{π}, I^{σ^+} and I^{σ^-}. The influence of such effects is minor interest for a general discussion but important for a full simulation in the next chapter. In general total intensity values are insignificant and only the ratios of this three values is important. In ideal case of statistical state population and for a filter with constant transmittance over the Zeeman-multiplett, this ratio is fixed to $2I^{\sigma^{\pm}} = I_{\pi}$.

For the MSE calculation the stokes vectors behind the FLC-plate were inserted to the image equation. Proceeding in the same way for the Zeeman multiplett leads to the following ansatz for the entire image equation, where for clarity $\hat{x} = c_\beta x + c_\gamma$ and $\hat{y} = c_\alpha y$ are defined.:

$$2I^{Zeeman}_{Image} = 2I(\hat{s}^{\pi}, \omega_0) + 2I(\hat{s}^{\sigma^-}, \omega_0 - \Delta\omega) + 2I(\hat{s}^{\sigma^+}, \omega_0 + \Delta\omega) \tag{62}$$

$$\begin{aligned}
&= \hat{s}_0^{\pi} + \hat{s}_0^{\sigma^+} + \hat{s}_0^{\sigma^-} \\
&+ I^{\pi}\hat{s}_1^{\pi}\cos(\omega_0\hat{x}) + (I^{\sigma^+}\hat{s}_1^{\sigma^+} + I^{\sigma^-}\hat{s}_1^{\sigma^-})\,\cos(\Delta\omega\hat{x})\cos(\omega_0\hat{x}) - (I^{\sigma^+}\hat{s}_1^{\sigma^+} - I^{\sigma^-}\hat{s}_1^{\sigma^-})\,\sin(\Delta\omega\hat{x})\sin(\omega_0\hat{x}) \\
&+ \frac{1}{2}\Big(I^{\pi}\hat{s}_2^{\pi} + (I^{\sigma^+}\hat{s}_2^{\sigma^+} + I^{\sigma^-}\hat{s}_2^{\sigma^-})\,\cos(\Delta\omega(\hat{x}+\hat{y})) + (I^{\sigma^+}\hat{s}_3^{\sigma^+} - I^{\sigma^-}\hat{s}_3^{\sigma^-})\;\sin(\Delta\omega(\hat{x}+\hat{y}))\Big)\cos(\omega_0(\hat{x}+\hat{y})) \\
&- \frac{1}{2}\Big(I^{\pi}\hat{s}_2^{\pi} + (I^{\sigma^+}\hat{s}_2^{\sigma^+} + I^{\sigma^-}\hat{s}_2^{\sigma^-})\,\cos(\Delta\omega(\hat{x}-\hat{y})) - (I^{\sigma^+}\hat{s}_3^{\sigma^+} - I^{\sigma^-}\hat{s}_3^{\sigma^-})\;\sin(\Delta\omega(\hat{x}-\hat{y}))\Big)\cos(\omega_0(\hat{x}-\hat{y})) \\
&+ \frac{1}{2}\Big(I^{\pi}\hat{s}_3^{\pi} + (I^{\sigma^+}\hat{s}_3^{\sigma^+} + I^{\sigma^-}\hat{s}_3^{\sigma^-})\,\cos(\Delta\omega(\hat{x}+\hat{y})) - (I^{\sigma^+}\hat{s}_2^{\sigma^+} - I^{\sigma^-}\hat{s}_2^{\sigma^-})\;\sin(\Delta\omega(\hat{x}+\hat{y}))\Big)\sin(\omega_0(\hat{x}+\hat{y})) \\
&+ \frac{1}{2}\Big(I^{\pi}\hat{s}_3^{\pi} + (I^{\sigma^+}\hat{s}_3^{\sigma^+} + I^{\sigma^-}\hat{s}_3^{\sigma^-})\,\cos(\Delta\omega(\hat{x}-\hat{y})) + (I^{\sigma^+}\hat{s}_2^{\sigma^+} - I^{\sigma^-}\hat{s}_2^{\sigma^-})\;\sin(\Delta\omega(\hat{x}-\hat{y}))\Big)\sin(\omega_0(\hat{x}-\hat{y}))
\end{aligned}$$

Theoretical description for the IMSE-system to measure the polarisation angle θ_S

For the single wavelength and the MSE case the image equation was rearranged and afterwards the different modes of the FLC-plate were investigated. This strategy is complicated for the Zeeman-Multiplett due to the symmetry break. Assuming the FLC-plate is replaced from the IMSE-system, the components from the stokes vectors can be replaced ($\hat{s}_2^{\pi} = s_2^{\pi}$ and $\hat{s}_2^{\sigma^{\pm}} = s_2^{\sigma^{\pm}}$). With some mathematically effort it is possible to show, that the FLC-Off case would lead to the same conclusions at the end, which is skipped here for clarity, but the FLC-On case will be discussed later in this section. Inserting the Stokes vectors as defined in (61) the image equation can be rewritten as:

$$\begin{aligned}
2I^{Zeeman} &= I^{\pi}\sin^2(\gamma) + (I^{\sigma^+} + I^{\sigma^-})\cdot(1+\cos^2(\gamma)) \\
&+ s_1\xi_0\cos(\omega_0\hat{x}) + s_1\kappa_0^S\sin(\omega_0\hat{x}) \\
&+ \frac{1}{2}\left(s_2\xi_+ - s_3\eta_+\right)\cos(\omega_0(\hat{x}+\hat{y})) \\
&- \frac{1}{2}\left(s_2\xi_- + s_3\eta_-\right)\cos(\omega_0(\hat{x}-\hat{y})) \\
&- \frac{1}{2}\left(s_3\kappa_+^c - s_2\kappa_+^s\right)\sin(\omega_0(\hat{x}+\hat{y})) \\
&- \frac{1}{2}\left(s_3\kappa_-^c + s_2\kappa_-^s\right)\sin(\omega_0(\hat{x}-\hat{y}))
\end{aligned} \tag{63}$$

In this equation the factors ξ_0, ξ_+ and ξ_- are analogous to the MSE case im equation (55) the spectral contrast functions for the linear part of the Zeeman polarisation, whereas the new factors η_0, η_+ and η_- denote spectral contrast for the circular polarised part. Since the π-component is always linear polarised, no η_0 occurs in the image equation for the Zeeman emission. The spectral functions are mainly influenced by the frequency splitting $\Delta\omega$ and the system parameter c_γ, which is included in $\hat{x}$.

The spectral functions for the linear and circular polarisation are defined as follows:

$$\begin{aligned}
\xi_0^Z &= I^\pi - (I^{\sigma^+} + I^{\sigma^-})\cos(\Delta\omega\hat{x}) \\
\xi_\pm^Z &= I^\pi - (I^{\sigma^+} + I^{\sigma^-})\cos(\Delta\omega(\hat{x} \pm \hat{y})) \\
\eta_0 &= (I^{\sigma^+} + I^{\sigma^-})\sin(\Delta\omega\hat{x}) \\
\eta_\pm &= (I^{\sigma^+} + I^{\sigma^-})\sin(\Delta\omega(\hat{x} \pm \hat{y}))
\end{aligned} \tag{64}$$

The factors κ_0, $\kappa_\pm^c$ and $\kappa_\pm^s$ image equation (38) occur as a result of different intensities for the $\sigma^\pm$-components, e.g if filter are used. If no unexpected effect causes a asymmetry of the intensities, these five factors become zero for an ideal filter. In this thesis they are denoted as filter factors and are defined by the following equations:

$$\begin{aligned}
\kappa_0^S &= (I^{\sigma^+} - I^{\sigma^-})\sin(\Delta\omega\hat{x}) \\
\kappa_\pm^C &= (I^{\sigma^+} - I^{\sigma^-})\cos(\Delta\omega(\hat{x} \pm \hat{y})) \\
\kappa_\pm^S &= (I^{\sigma^+} - I^{\sigma^-})\sin(\Delta\omega(\hat{x} \pm \hat{y}))
\end{aligned} \tag{65}$$

For the Zeeman-multiplett the different Fourier components can be demodulated by using the two-dimensional Fourier transform and the corresponding inverse Fourier transform, which is the same procedure as for the MSE multiplett. The exponential terms of the Fourier components are only changed by the smaller frequency splitting in comparison to the MSE, so again seven Fourier components are given in the Fourier picture calculated from the interference pattern, which was measured by the CCD camera. The Fourier components are given by:

$$\begin{aligned}
I(0,0) &= \frac{1}{2}(I^\pi \sin^2(\gamma) + (I^{\sigma^+} + I^{\sigma^-}) \cdot (1 + \cos^2(\gamma)) \\
I(\pm,0) &= \frac{1}{4}s_1^Z(\xi_0 \mp i\kappa_0^S)e^{\pm i\omega\hat{x}} \\
I(\pm,\pm) &= \frac{1}{8}((s_2\xi_+ - s_3\eta_+) \mp i(s_2\kappa_+^S - s_3\kappa_+^C))e^{\pm i\omega(\hat{x}+\hat{y})} \\
I(\pm,\mp) &= -\frac{1}{8}((s_2\xi_- + s_3\eta_-) \mp i(s_2\kappa_-^S + s_3\kappa_-^C))e^{\pm i\omega(\hat{x}-\hat{y})}
\end{aligned} \tag{66}$$

If the filter functions are zero, because an ideal filter was used, the factors in front of the exponential term become real values. Again, it is possible to calculate the amplitudes of the Fourier components. This results in following equations for the amplitudes:

$$\begin{aligned}
|I(0,0)| &= \frac{1}{2}|(I^\pi \sin^2(\gamma) + (I^{\sigma^+} + I^{\sigma^-}) \cdot (1 + \cos^2(\gamma))| \\
|I(\pm,0)| &= \frac{1}{4}|s_1|\sqrt{(\xi_0)^2 + (\kappa_0^S)^2} \\
|I(\pm,\pm)| &= \frac{1}{8}\sqrt{(s_2\xi_+ - s_3\eta_+)^2 + (s_2\kappa_+^S - s_3\kappa_+^C)^2} \\
|I(\pm,\mp)| &= \frac{1}{8}\sqrt{(s_2\xi_- + s_3\eta_-)^2 + (s_2\kappa_-^S + s_3\kappa_-^C)^2}
\end{aligned} \tag{67}$$

The corresponding complete amplitudes consists of a square root over two terms. The first term contains the stokes vectors weighted with the linear and circular spectral functions, whereas the

second term describes the influence of intensity asymmetry in the $\sigma^{\pm}$-components. For the Zeeman emission the antisymmetric ellipticity introduces a difference between the amplitude of the symmetric Fourier components $|I(\pm.\pm)|$ and the antisymmetric Fourier components $|(I\pm,\mp)|$ due to different signs in the first term. Assuming the κ-factors to be small by using an approximately ideal filter the total intensity symmetry of the $\sigma^{\pm}$-components leads to the following simplification of the Fourier amplitudes:

$$\begin{aligned} |I(0,0)| &= \frac{1}{2}|(I^{\pi}\sin^2(\gamma) + (I^{\sigma^+} + I^{\sigma^+}) \cdot (1+\cos^2(\gamma))| \\ |I(\pm,0)| &= \frac{1}{4}|s_1^Z||\xi_0^Z| \\ |I(\pm,\pm)| &= \frac{1}{8}|s_2\xi_+ - s_3\eta_+| \\ |I(\pm,\mp)| &= \frac{1}{8}|s_2\xi_- + s_3\eta_-| \end{aligned} \tag{68}$$

For $\gamma \approx 90°$ (i.e. vanishing ellipticity for the $\sigma^{\pm}$-components) the Fourier amplitudes show a periodicity in θ_S with 90°. This is the same as for the MSE measurement, since the MSE multiplett in fully linear polarised. For smaller values of γ, this symmetry breaks for $|I(\pm,\pm)|$ and $|I(\pm,\mp)|$ and the periodicity of these amplitudes are only in 180° of θ_S. The corresponding illustration is given in Figure 24.

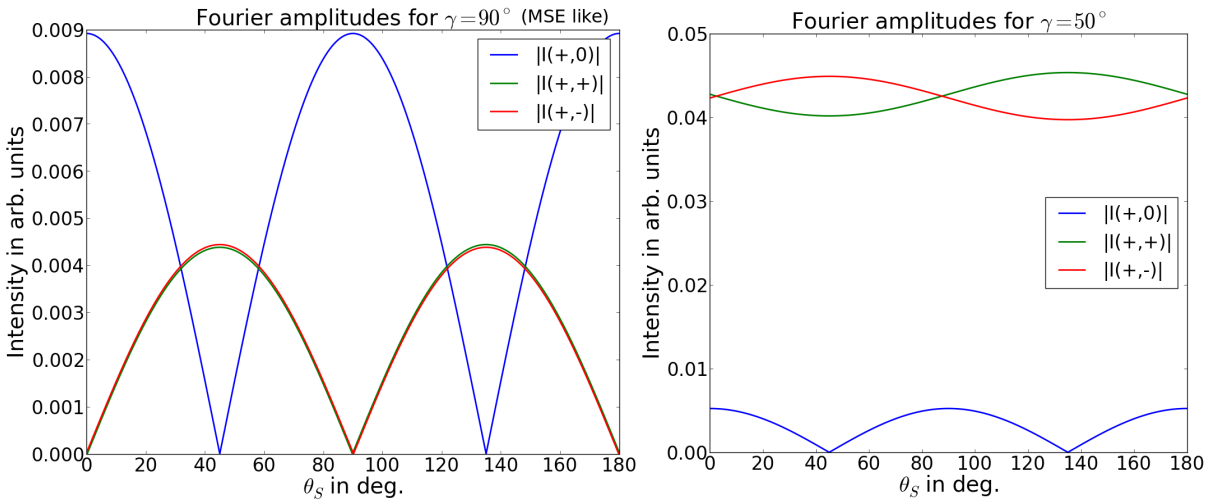

Figure 24 – Fourier amplitudes dependent on the polarisation angle θ_S for different values of γ.

In the limiting case of small ellipticity for the $\sigma^{\pm}$-components ($s_3 \approx 0$) or if the delay plate thickness is optimised to the Zeeman splitting ($\eta_+, \eta_- \approx 0$), the relations analogue as for the MSE case in (59) or (60) may be used to achieve sufficiently accurate results for the polarisation angle. This will be investigated in detail later in this chapter. For the general case of non-negligible ellipticity, the equations (59) or (60) can lead to a large error. For this reason a new equation must be found for data evaluation of the polarisation angle in the Zeeman case.
Taking the absolute value to get the amplitude is the standard method during data evaluation and leads to the loose of the sign information of $\tau = s_2\xi_+ - s_3\eta_+$. This has no physical reason

and is only a mathematically artefact. Therefore, a analysis is needed to find a new evaluation equation. Assuming $\xi_{\pm} \approx \xi_0$ and $\eta_{\pm} \approx \eta_0$, the following cases must be differentiated:

1. $s_2\xi_0 \leq s_3\eta_0$: This case is given if the circular polarisation has a strong influence and the spectral function for circular polarisation η_0 is strong against the spectral function for linear polarisation ξ_0. In this case the amplitudes can be written as follows:

$$|I(\pm,\pm)| = \frac{1}{8}(s_3\xi_0 - s_2\eta_0) \quad \text{and} \quad |I(\pm,\mp)| = \frac{1}{8}(s_3\xi_0 + s_2\eta_0)$$

   The polarisation angle can now be obtained by following equation:

$$\tan 2\theta_S = \frac{s_2}{s_1} \approx \frac{|I(+,-)| - |I(+,+)|}{|I(+,0)|} \tag{69}$$

2. $s_2\xi_0 > s_3\eta_0$: This case is valid for small weighted ellipticity and the amplitudes can be written as follows:

$$|I(\pm,\pm)| = \frac{1}{8}(s_2\xi_0 - s_3\eta_0) \quad \text{and} \quad |I(\pm,\mp)| = \frac{1}{8}(s_2\xi_0 + s_3\eta_0)$$

   The polarisation angle can the be calculated by the following relation:

$$\tan 2\theta_S = \frac{s_2}{s_1} \approx \frac{|I(+,-)| + |I(+,+)|}{|I(+,0)|} \tag{70}$$

Since ξ_0, ξ_+ and ξ_- as well as η_0, η_+ and η_- are slightly different in y, the error of θ_S is assumed to be a function of y and to become small for the center of the picture ($y \longrightarrow 0$).

Derivation of the IMSE-response with activated FLC-plate

Before the new equations are discussed more in detail for the current setup of the IMSE-system and with the aim to realise calibration, the influence of the interlaced FLC-plate will be investigated. Starting from the complete image equation (62) the calculation for the interlaced FLC-plate ($\hat{s_1} = -s_3$ and $\hat{s_3} = s_1$) can be performed the same way as in the former section. The resulting image equation for the interlaced FLC-plate is given as follows:

$$\begin{aligned}
2I_{Image}^{Zeeman} &= I^{\pi}\sin^2(\gamma) + (I^{\sigma^+} + I^{\sigma^+}) \cdot (1 + \cos^2(\gamma)) \\
&+ s_3\kappa_0^S\cos(\omega_0\hat{x}) - s_3\eta_0\sin(\omega_0\hat{x}) \\
&+ \frac{1}{2}\left(s_2\xi_+^Z - s_1\kappa_+^s\right)\cos(\omega_0(\hat{x}+\hat{y})) \\
&- \frac{1}{2}\left(s_2\xi_-^Z + s_1\kappa_-^s\right)\cos(\omega_0(\hat{x}-\hat{y})) \\
&+ \frac{1}{2}\left(s_1\xi_+^Z + s_2\kappa_+^s\right)\sin(\omega_0(\hat{x}+\hat{y})) \\
&+ \frac{1}{2}\left(s_1\xi_-^Z - s_2\kappa_-^s\right)\sin(\omega_0(\hat{x}-\hat{y}))
\end{aligned} \tag{71}$$

The Fourier components and the corresponding amplitudes can then be calculated as follows:

$$\begin{aligned} I(0,0) &= \frac{1}{2}(I^{\pi}\sin^2(\gamma) + (I^{\sigma^+} + I^{\sigma^+}) \cdot (1+\cos^2(\gamma)) \\ I(\pm,0) &= \frac{1}{4}s_3(\kappa_0^S \mp i\eta_0)e^{\pm i\omega\hat{x}} \\ I(\pm,\pm) &= \frac{1}{8}((s_2\xi_+ - s_1\kappa_+^S) \mp i(s_1\xi_+ + s_2\kappa_+^S))e^{\pm i\omega(\hat{x}+\hat{y})} \\ I(\pm,\mp) &= -\frac{1}{8}((s_2\xi_- - s_1\kappa_-^S) \pm i(s_1\xi_- + s_2\kappa_-^S))e^{\pm i\omega(\hat{x}-\hat{y})} \end{aligned} \tag{72}$$

$$\begin{aligned} |I(0,0)| &= \frac{1}{2}|(I^{\pi}\sin^2(\gamma) + (I^{\sigma^+} + I^{\sigma^+}) \cdot (1+\cos^2(\gamma))| \\ |I(\pm,0)| &= \frac{1}{4}|s_3|\sqrt{(\kappa_0^S)^2 + (\eta_0)^2} \\ |I(\pm,\pm)| &= \frac{1}{8}\sqrt{(s_2\xi_+ - s_1\kappa_+^S)^2 + (s_1\xi_+ + s_2\kappa_+^S)^2} \\ |I(\pm,\mp)| &= \frac{1}{8}\sqrt{(s_2\xi_- - s_1\kappa_-^S)^2 + (s_1\xi_- + s_2\kappa_-^S)^2} \end{aligned} \tag{73}$$

The amplitudes of the Fourier components for the interlaced FLC-plate are different from the former case. The amplitudes $|I(\pm,0)|$ are independent of s_1 or s_2 and therefore also independent of the polarisation angle θ_S. The amplitudes $|I(\pm,\pm)|$ and $|I(\pm,\mp)|$ are not effected by a spectral contrast function for circular polarisation η_- and η_+, but $|I(\pm,0)|$ are influenced by η_0.

If the filter factors are vanish the amplitudes simplify to following equations:

$$\begin{aligned} |I(0,0)| &= \frac{1}{2}|(I^{\pi}\sin^2(\gamma) + (I^{\sigma^+} + I^{\sigma^+}) \cdot (1+\cos^2(\gamma))| \\ |I(\pm,0)| &= \frac{1}{4}|s_3^Z||\eta_0| = \frac{1}{4}|\eta_0||2\cos(\gamma)| \\ |I(\pm,\pm)| &= \frac{1}{8}|\xi_+|\sqrt{(s_1^Z)^2 + (s_1^Z)^2} = \frac{1}{8}|\xi_+||\sin^2(\gamma)| \\ |I(\pm,\mp)| &= \frac{1}{8}|\xi_-|\sqrt{(s_1^Z)^2 + (s_1^Z)^2} = \frac{1}{8}|\xi_-||\sin^2(\gamma)| \end{aligned} \tag{74}$$

All Fourier amplitudes are independent of the polarisation angle θ_S. The same statement is valid for the MSE measurement, where the FLC-plate can be used to measure small ellipticity effects of the MSE components. In general, the absolute intensity of the Fourier amplitudes is unknown, which makes a division of the amplitudes necessary to eliminate the absolute intensity. The relation between the Fourier amplitudes and the ellipticity χ of the $\sigma^{\pm}$-components are given by equation (75).

$$\tan(2\chi) = \frac{2\cos(\gamma)}{\sin(\gamma)^2} = \varepsilon\frac{2|I(\pm,0)|}{|I(\pm,\pm)|} \tag{75}$$

The ratio of the spectral functions $\varepsilon = |\xi_+|/|\eta_0|$ in equation (75) depends on the system configuration. Theoretically the factor can be roughly estimated from the energy splitting and the thickness of the delay plate. Small changes of this factor effect the amplitudes strong enough

to make accurate measurement of the ellipticity for the Zeeman-emission impractical. Figure 25 illustrates the amplitudes as a function of γ for different values of ε.

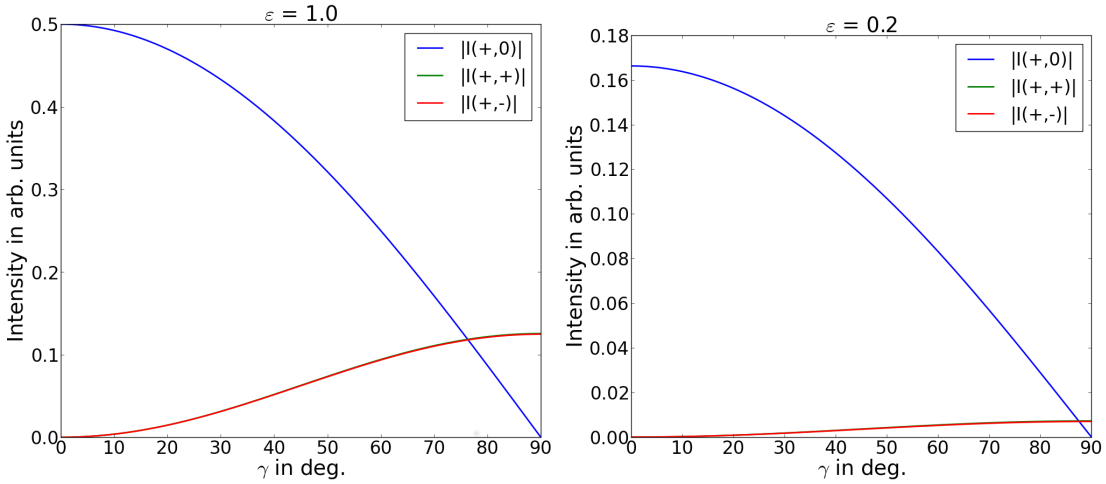

Figure 25 – Dependence of the Fourier amplitudes for γ variation and different values of ε.

6.2 Theoretical analysis of the current IMSE-system measuring Zeeman-emission

In this section the response of the IMSE-diagnostic to Zeeman-emission for contemporary system configuration will be investigated. This means, that the delay plate has a thickness $L_W = 1.2\,mm$ leading to a value for the system parameter $c_\gamma \approx 1.5 \cdot 10^{-12}$ sm^{-1}. All other system parameters are the same a introduces in section 5.2. The following discussion is focused on the dependence of the systems response to the polarisation angle θ_S, viewing angle γ and the pixel position x and y on the CCD-camera. The value of the magnetic field strength is therefore also assumed to have a fix value of $|\vec{B}| = 2$ T, which is a realistic order of magnitude for ASDEX Upgrade. This leads also to a fixed value for the Zeeman splitting of $\Delta\lambda \approx 0.04$ nm. For this condition the values of the spectral functions only changing across the image due to change of x and y. For $x = 0$ mm and $y = y_{max} = 3.17$ mm (i.e. a position at the edge of the picture at the CCD-camere), the spectral functions depends on the system coefficient c_γ as shown in Figure 26. The value of c_γ for the current IMSE-system is marked by the black dashed line. Changes in x would only lead to a small deviation of the spectral functions, which is not important for the following discussion. The value of y was chosen to be maximal to illustrate the maximal difference between the several spectral functions, since for $y = 0$ mm the relations $\eta_\pm = \eta_0$ and $\xi_\pm = \xi_0$ are valid. Figure 26 shows, that for the current configuration (black dashed line) of the IMSE-system $\eta_0 \gg \xi_0$. This means that the circular polarised part of the Zeeman emission is weighted very strong by the system in comparison to the linear part, which contains the relevant information about the polarisation angle. For a reasonable measurement or calibration this ratio of the spectral functions in therefore problematic. To improve the spectral function ratio a optimisation by changing system parameters is possible. This will be discussed later in this chapter.

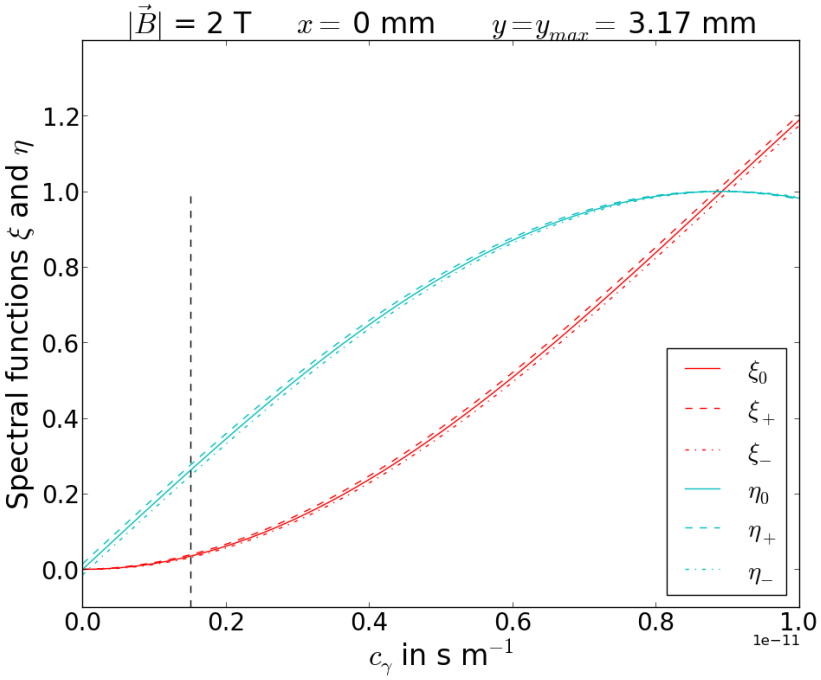

Figure 26 – Spectral functions for different values of the system coefficient c_γ. The black dashed line illustrates the current value of the system (i.e. with the delay plate used for the MSE measurement).

In the next step it is necessary to consider which of equation (69) or (70) is valid to obtain the polarisation angle θ_S for the given system configuration. Figure 27 shows the value of the term $\tau = s_3\eta_0 - s_2\xi_0$ as a function of the polarisation angle θ_S and the viewing angle γ, since the sign of τ can be seen as the determining criteria.

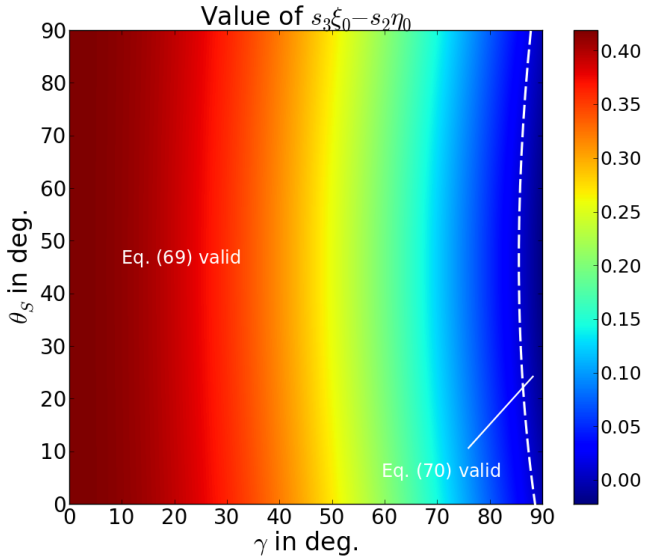

Figure 27 – Value of the parameter τ for the current IMSE-system configuration in dependence of the polarisation angle θ_S and angle γ . The value determines if equation (69) or (70) must be used for data evaluation.

If τ is positive, equation (69) must be used, whereas for a negative value of τ equation (70) is relevant. The results in Figure 27 show, that equation (69) will give the correct θ_S for all $\gamma \leq 87°$. Only for $\gamma > 87°$, which means nearly vanishing circular polarisation for the σ-components, the other equation is useful. Since η_0 is large against ξ_0, equation (69) is expected to give better results than using the equations (59) and (60) as for the MSE-case. Those equations (59) and (60) will only lead to sufficiently accurate results, if the σ-components are entirely linear polarised. The dependence of the sign of τ from γ and the ratio of the spectral functions is problematic for measurements, since it determines the data evaluation and can only be estimated for a fixed system configuration.

To investigate the accuracy of θ_S calculated from measured data by equation (69) in dependence of x, y and γ, short numerical calculations are useful. For this θ_{Exact} is defined as true value for the polarisation angle. It is used to calculate Stokes vectors and Fourier components. From the Fourier components θ_{Result} is then calculated with (69) and represents the measured value in this simple simulation. This model ignores errors introduced by the real demodulation process with two-dimensional Fourier transform and from noise in the measured data, but is useful to understand the intrinsic influence of different parameter for the measurement. These other effects will be considered in the next chapter dealing with a full simulation of the IMSE-system measuring the Zeeman-edge emission at ASDEX Upgrade. If equation (69) does not introduce an error, the relation between θ_{Exact} and θ_{Result} is as presented in Figure 28. The value of θ_{Result} is only defined in the interval $[0°, 45°]$, since the arctangent of a positive amplitude is used for data evaluation. For the real measurement or a calibration with the IMSE-system this ambiguity does not cause a problem, since the orientation of the polarisation can be roughly estimated geometrically. For the MSE measurement deviations from this ideal case are periodic with 90° due to the periodicity of the amplitudes. For the Zeeman emission the periodicity of both is for 180°.

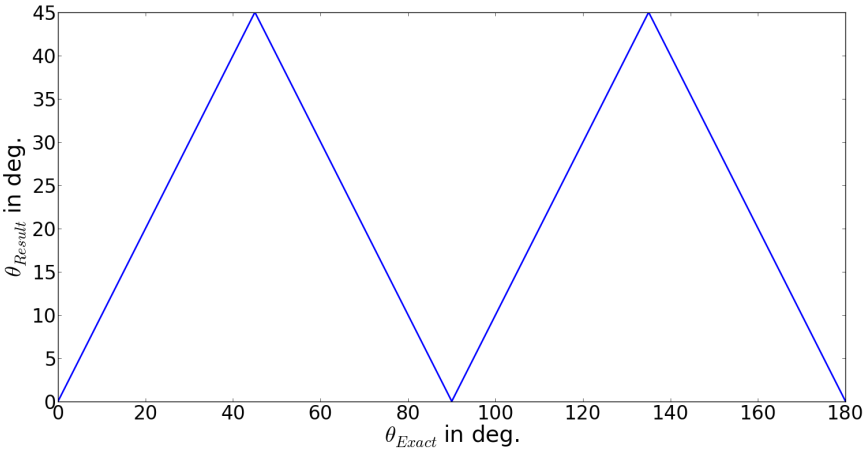

Figure 28 – Dependence between real polarisation angle θ_{Exact} and measured polarisation angle θ_{Result} for an ideal measurement with vanishing error.

For following theoretical calculation, the viewing angle γ is varied over the full range of possible values, whereas three different values for y are selected with $y_{max} = 3.17$ mm characterising the edge of the image. Since changing x will not influence the results here, the value is fixed to $x = 0$. The results are illustrated in Figure 29.

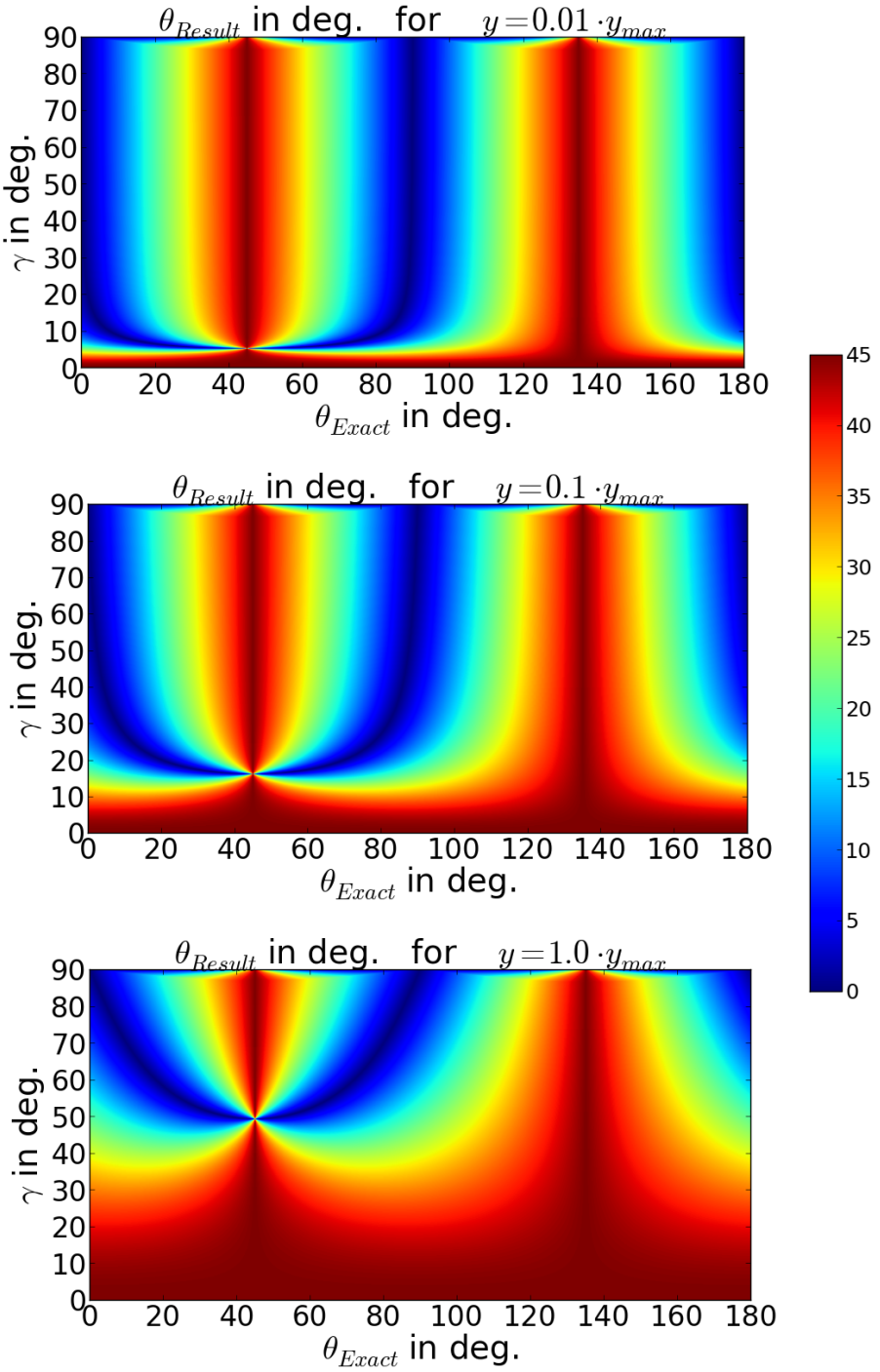

Figure 29 – Simulated measurement value for the polarisation angle θ_{Result} in dependence of the exact input value θ_{Exact} and the observation angle γ for different values of y. The simulated values are valid for the current configuration of the IMSE-system.

In the case of small γ, which means viewing direction nearly parallel to the magnetic field or nearly full circular polarisation of the $\sigma^{\pm}$-components, the information about the polarisation angle θ_s is entirely lost in all cases. This effect is enhanced by the high weighing of circular polarisation against the linear parts induced by the spectral functions. For $\gamma \leq 87°$ the calculation with equation (69) gives wrong results as explained is the former section. In this range (70) is needed. The results show, that with increasing y the calculated value for θ_S become useless. This effect is strong and only for very small y the accuracy is sufficient. For smaller values of γ, the deviations between the exact and the calculated value of the polarisation angle θ_S become lager, which comes from the increasing ellipticity of the $\sigma^{\pm}$-components with decreasing γ. All this causes, that the reasonable data points are strictly restricted to a small area around $y = 0$ mm, which means for perpendicular incident angle ($\alpha_I = 0°$) on the Savart plate. For the real IMSE-system, it is not necessarily true that perpendicular incident is really given for the center of the picture. A small deviation may exist due to setup accuracy. Secondly, for a reasonable calibration a averaging about several data points is needed in real experiments to reduce noise effects, which is avoided by the strong limitation of useful data points. In summary it can be said, that the sensitivity of the measurement to the polarisation angle θ_S is low under contemporary system conditions. Only for nearly perpendicular observation ($\gamma = 90°$) the polarisation angle can be measured well enough with using equation (70) during data evaluation. A reasonable calibration with the aim of $\Delta\theta_s < 0.05°$ by observing the Zeeman edge emission with the current system configuration is general not realisable, since total perpendicular observation is rarely the case. For this reason a analysis will show later, if changing the intrinsic system parameter can prepare the IMSE-system for a sufficient calibration of the system by measuring the Zeeman edge emission for a wider range of observation angles γ. Before optimisation possibilities are discussed the next section will illustrate influences of variations of the intensity ratios.

6.3 Influence of non-statistic population of atomic states and filter effects

In the former section the intensity ratios of the Zeeman emission were assumed to be ideal with $I^{\pi} = 2I^{\sigma^{\pm}}$. This assumption is not valid it general, especially due to the filter used to select the Zeeman multiplett from backround emission. For the narrow frequency splitting of the Zeeman emission, the transmittance over this small wavelength range increases or decreases mostly monotonic. It can assumed that filters therefore are introducing a asymmetry for the intensity of the $\sigma^{\pm}$-components, but not effect the intensity ration between the $\sigma^{\pm}$- and the π-component strongly. The following Figure 30 illustrates the results for two different cases of asymmetric intensity ratios for $y = 0.1 \cdot y_{max}$. This allows a comparison to the result from Figure 29 (middle part), where all other conditions are identically. In the of Figure 30 the intensity values are $I^{\pi} = 1.0$, $I^{\sigma^+} = 0.45$ and $I^{\sigma^-} = 0.55$ for the upper part and $I^{\pi} = 1.0$, $I^{\sigma^+} = 0.40$ and $I^{\sigma^-} = 0.60$ in the lower part. Over the entire range of γ the intensity asymmetry causes a additional deviation between θ_{Result} and θ_{Exact}. The strength of this deviation increases with increasing asymmetry. In comparison to the deviation introduced by γ, asymmetry effects are in practice mostly small. Only for perpendicular observation ($\gamma \approx 45°$) the influence of the filter to the measurement become relevant. The total transmittance of used filters is only important for the signal strength, but has no influence here.

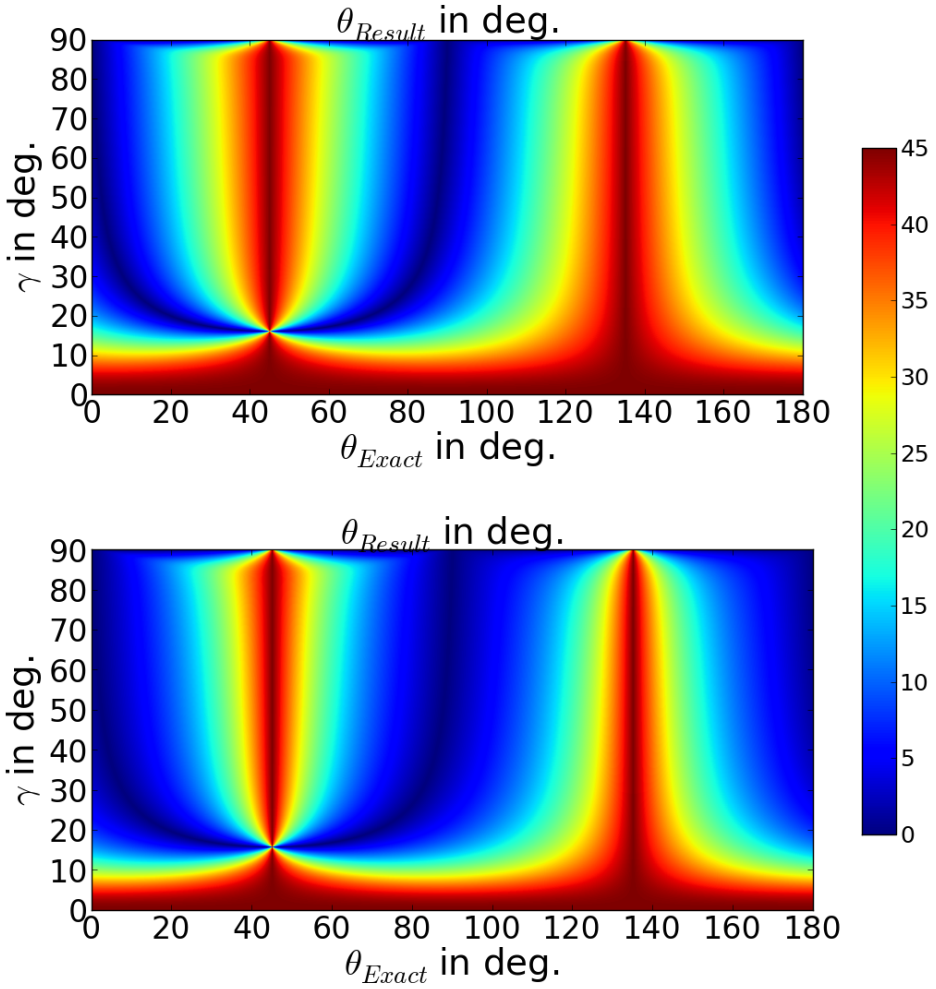

Figure 30 – Simulated measurement value for the polarisation angle θ_{Result} in dependence of the exact input value θ_{Exact} and the observation angle γ for fixed $y = 0.1 \cdot y_{max}$. The simulated values are valid for the current configuration of the IMSE-system. The following intensity ratios are used:
- Upper part: $I^{\pi} = 1.0$, $I^{\sigma^+} = 0.45$ and $I^{\sigma^-} = 0.55$
- Lower part: $I^{\pi} = 1.0$, $I^{\sigma^+} = 0.40$ and $I^{\sigma^-} = 0.60$

The second ratio, which can be influenced, is the ration between I^{π} and $I^{\sigma} = I^{\sigma^+} + I^{\sigma^-}$. In general this can happen due to non-statistical population of the atomic states. Figure 31 shows two different cases for this scenario, where all other parameters are fixed as for the former considerations. In both cases $I^{\pi} = 1.0$, whereas $I^{\sigma} = 0.9$ in the upper and $I^{\sigma} = 0.8$ in the lower case. The intensity of the $\sigma^{\pm}$-components are symmetric ($I^{\sigma^+} = I^{\sigma^-}$). A smaller value for I^{σ}/I^{π} leads to an improvement of the measurement, since the influence of the perturbing circular polarisation of the $\sigma^{\pm}$-components decreases stronger relative to linear polarisation information, which is also included in the π-component. That the area with useless results for high γ expands to lower values is a effect of shifting values of τ. This means, that the range of γ, in which the wrong data evaluation equation is used becomes wider. Data evaluation for the Zeeman emission is especially complicated if τ is closed to zero, because which equation must be used can only be estimated from theory. All cases in which τ has the same sign over the full range of γ and θ_S are therefore non problematic. For real experiments non-statical state population are more

important for MSE-measurements, since plasma edge hydrogen neutral are commonly follow a statistical population. For neutral beam emission a non-statistical population of the atomic states is possible [29, 30]. For only small deviations from this the effect to the measurement is weak and can be neglected in general. From the last section it remains the problem, that the IMSE-system in the current configuration is gives inaccurate results. The next section will introduce a possibility to optimise the system for the Zeeman emission and then discuss, how efficient such an optimisation is.

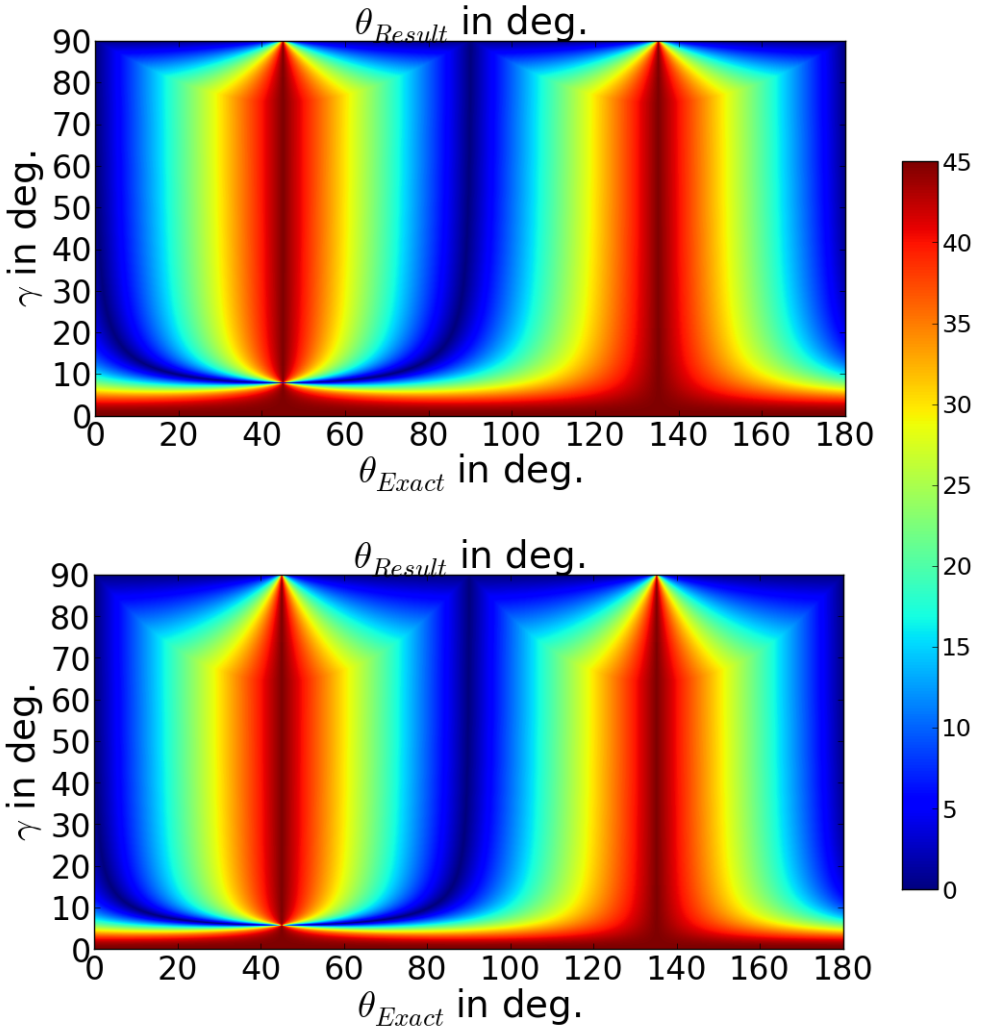

Figure 31 – Simulated measurement value for the polarisation angle θ_{Result} in dependence of the exact input value θ_{Result} and the observation angle γ for fixed $y = 0.1 \cdot y_{max}$. The simulated values are valid for the current configuration of the IMSE-system. The following intensity ratios are used:
- Upper part: $I^{\pi} = 1.0$, $I^{\sigma^+} = 0.45$ and $I^{\sigma^-} = 0.45$
- Lower part: $I^{\pi} = 1.0$, $I^{\sigma^+} = 0.40$ and $I^{\sigma^-} = 0.40$

6.4 Optimisation of the IMSE-system for measuring Zeeman emission by changing intrinsic system parameters

In the last section theoretical investigations have shown, that for the current IMSE-system a reasonable calibration utilizing the Zeeman edge emission is impossible due to low sensitivity of the system to the linear polarisation information of the Zeeman multiplett. The main reason therefore is given by the unsuitable ratio of the spectral contrast functions ξ_0 and η_0. In this section the spectral contrast functions will be optimised by changing the relevant system parameters.

Since the spectral functions in general depend on the values of x and y a entire optimisation for all points on the CCD-camera is impossible. In the following section the system will be optimised for $x = 0\ mm$ and $y = 0\ mm$ and afterwards the influence of different pixel positions (i.e. incident angles) will be investigated. The main deviations for the measured polarisation angle θ_S are caused by the circular polarised part of the $\sigma^{\pm}$-components. Since the polarisation states of the Zeeman multiplett are fixed by the unchangeable viewing geometry, the only way to reduce the influence of the perturbing circular polarisation is to minimize the absolute value of spectral function for circular polarisation η_0. For the same conditions the spectral function for the linear polarisation ξ_0 will be selected as high as possible. The relevant parameter for this optimisation are the magnetic field strength $|\vec{B}|$ and the system parameter c_γ. A rough range of 1.7 - 2.7 T for the magnetic field strength is predefined by operation conditions of the fusion device. As result c_γ must be the variable parameter for optimisation. Since the refractive indices for the plate material αBBO is fixed and the thickness of the displacer plate L_D is not allowed to be changed for accuracy of the measurement, only the delay plate thickness L_W can be optimised to Zeeman emission. Figure 32 shows in dependence of $|\vec{B}|$ and L_W the parameter area, in which η_0 vanishes and ξ_0 becomes maximal. Both requirements are fulfilled simultaneously, if $c_\gamma \Delta\omega = (2k-1)\cdot\pi$, where k is positive natural number.

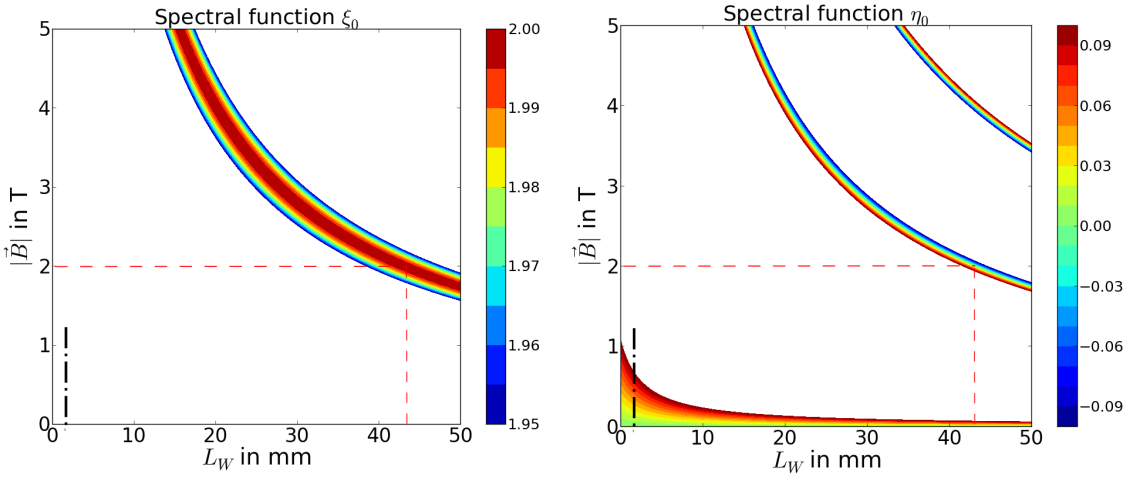

Figure 32 – Parameter area for optimisation of the spectral contrast functions ξ_0 and η_0 in dependence of the magnetic field strength $|\vec{B}|$ and the thickness of the delay plate L_W. The black dashed line marks the delay plate thickness for the current diagnostic and the red dashed line the plate thickness for optimisation to $|\vec{B}| = 2$ T.

According to Figure 32 a delay plate thickness of $L_W = 43$ mm is required to optimise the system for a magnetic field strength with $|\vec{B}| = 2$ T. This large value is a result of the small energy splitting from Zeeman effect in comparison with the MSE splitting range. The figure 32 also illustrates a strong dependence between the strength magnetic field and the required delay plate thickness, so for a 2.5 T the thickness must be only 32 mm. In conclusion the system optimisation is only valid for a small range of the magnetic field strength $|\vec{B}|$, which is problematic for calibration. The effect of small deviations from the optimised plate thickness will be discussed later. The use of thick delay plates also decrease the absolute intensity and contrast due to absorption and susceptibility to intrinsic crystal defects perturbing the measured signal. For the optimised system with $L_W = 43$ mm and $|\vec{B}| = 2$ T it is necessary, to find the correct evaluation equation. To investigate this, Figure 33 illustrates the value of τ in dependence of the angles θ_S and γ.

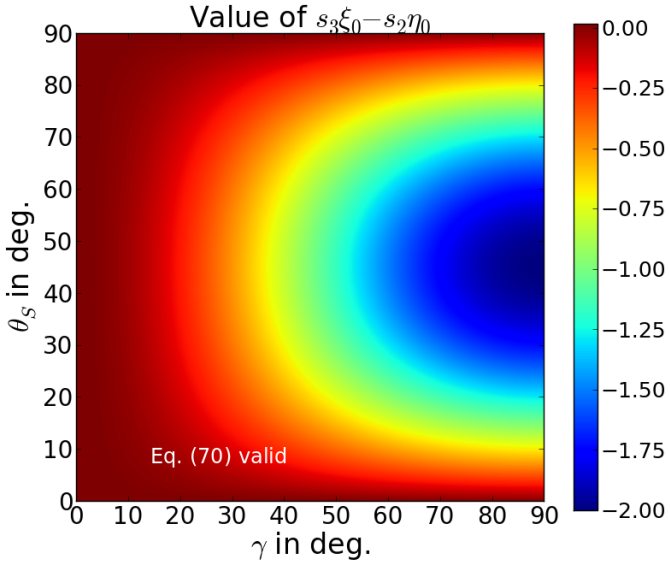

Figure 33 – Value of the parameter τ for the theoretically optimised IMSE-system configuration in dependence of the polarisation angle θ_S and angle γ . The value determines if equation (69) or (70) must be used for data evaluation.

Figure 33 shows that τ is mainly negative, which means that equation (70) must be used for data evaluation. For small values of γ this equation will not give the correct value, but viewing directions parallel to the magnetic field are general problematic cause of the high dominance of circular polarisation. Analogous to the former case of the current IMSE-system configuration an identical plot as in Figure 29 is now shown in Figure 34 for the optimised IMSE-system. For the optimised IMSE-system the error for the polarisation angle introduced by changes of y is much smaller, so a larger area on the CCD-camera give accurate data for calibration and allow a averaging about several data points for signal-to-noise optimisation. For γ over 30° the entire CCD-picture is usable and only for small γ the information about polarisation angle θ_S is totally lost.

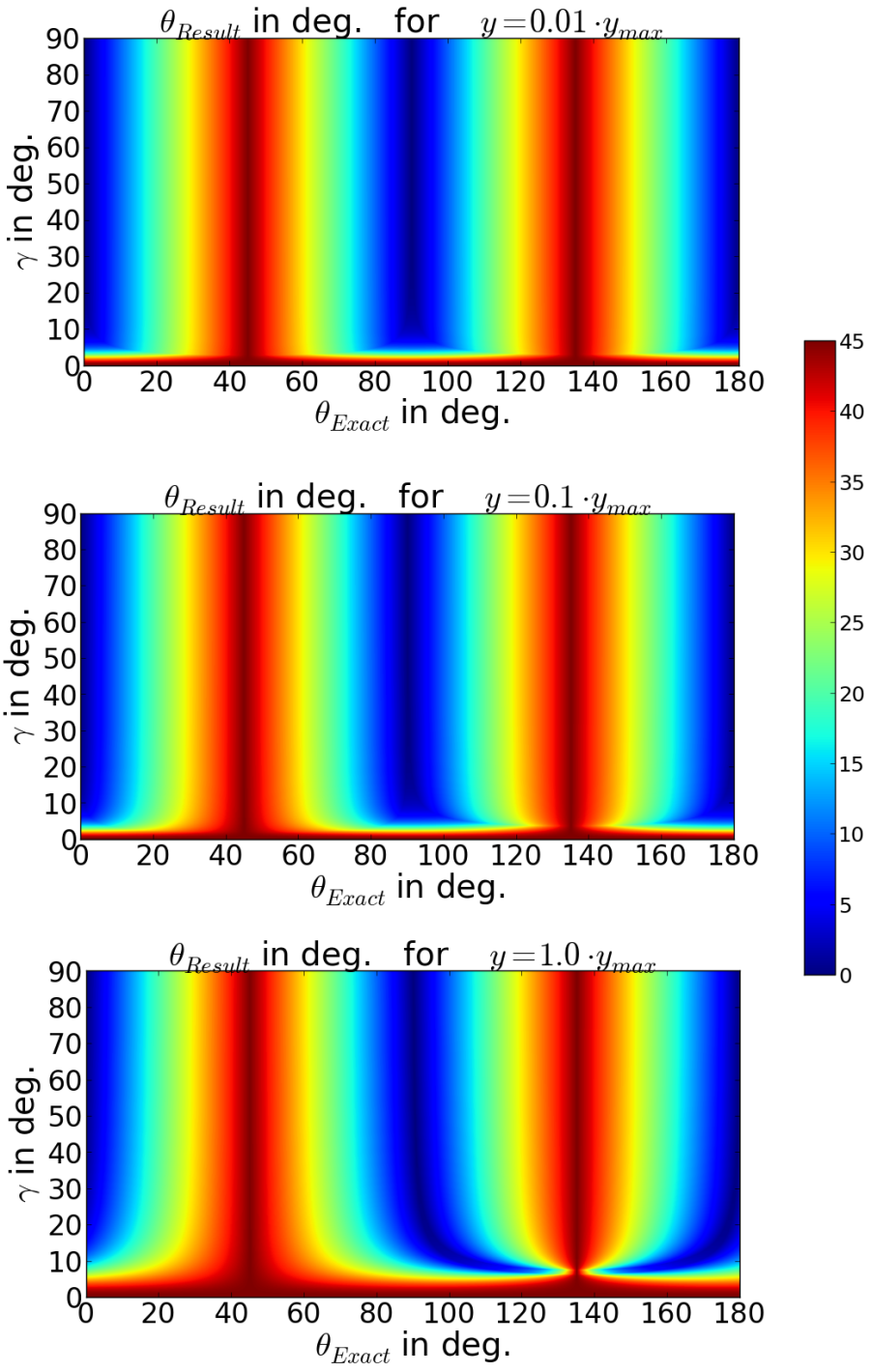

Figure 34 – Simulated measurement value for the polarisation angle θ_{Result} in dependence of the exact input value θ_{Result} and the observation angle γ for different values of y. The simulated values are valid for the theoretically optimised configuration of the IMSE-system.

Before the influence of magnetic field variation to the optimised IMSE-system is investigated, the use of standard equation for data evaluation as for the MSE-multiplett can be proven, since the circular polarisation is nearly full repressed due to optimisation by vanishing η_0.

For $y = 0.1 \cdot y_{max}$ the Figure 35 illustrates the data evaluation with equation (59) for the upper part and with equation (60) for the lower part. For both equation used here the results have the same high accuracy for $\gamma > 20°$ as for the introduces equation (70) for the Zeeman emission.

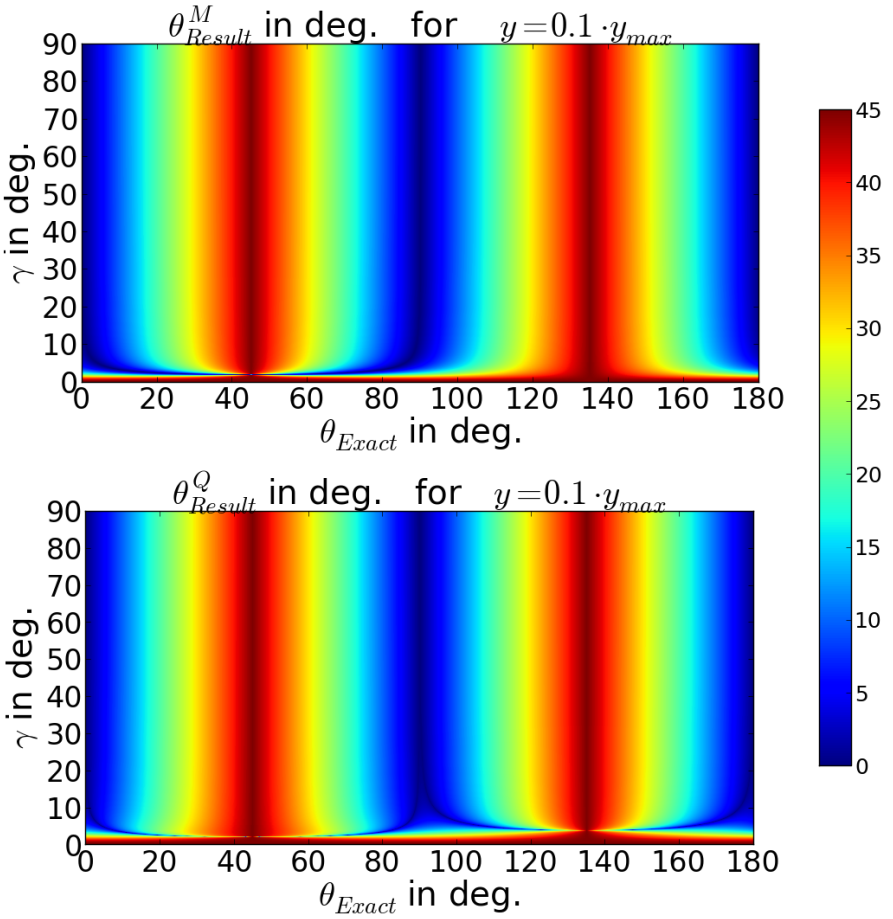

Figure 35 – Simulated measurement value for the polarisation angle θ_{Result} as a function of the exact input value θ_{Exact} and the observation angle γ. Polarisation angle θ_{Exact} obtained with equation (59) (upper part) and equation (60) (lower part).

It was already mentioned, that after the results in Figure 32 small deviations in the magnetic field strength can change the spectral functions ξ_0 and η_0 strongly and therefore adjust the system away from optimisation. To investigate this effect, small variations of the magnetic field strength ($|\vec{B}| = 2.02$ T and $|\vec{B}| = 1.95$ T) were introduced to the theoretical calculation, whereas $y = 0.1 \cdot y_{max}$ are assumed as fixed. The results are shown in Figure 36.
The results in Figure 36 illustrate, that small magnetic field changes are enough to decrease accuracy of the measurement dramatically for $\gamma < 45°$. For this condition optimisation of the IMSE-system is general limited by a narrow range of magnetic field values, which was already expected. Since the magnetic field varies spatial inside a tokamak and also for different pulses, a system optimisation as investigated in this section seems not to be a useful improvement.

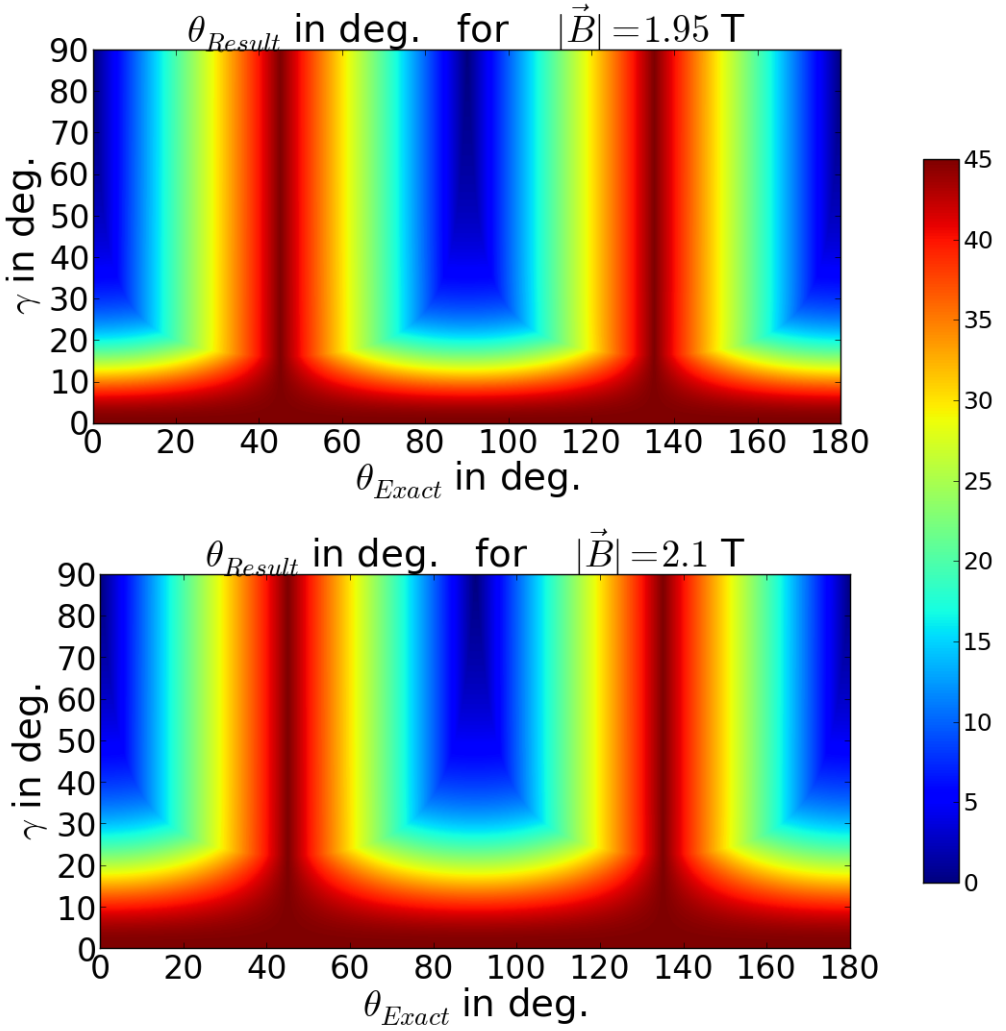

Figure 36 – Simulated measurement value for the polarisation angle θ_{Result} in dependence of the exact input value θ_{Exact} and the observation angle γ for different values of the magnetic field strength $\vec{B}|$. Polarisation angle θ_{Result} obtained with equation (70)d.

Again only for high values of γ the accuracy of the measurement is weakly affected, so that for nearly perpendicular observation a real increase of the accuracy for the measured polarisation angles can be achieved. Under condition of nearly perpendicular observation relative to the magnetic field direction a system optimisation might be useful. In general the system optimisation will not make a calibration of the IMSE-system more realistic as for the current IMSE-system. The general effect of filters and non-statistical distribution are the same for the optimised IMSE-system as for the current setup. Since the optimised system is strongly sensitive to different parameter changes, the effect of unsuitable filter will be stronger for this case. The main conclusions of the theoretical investigation in this chapter are shortly summarized at this point:

1. In general for a wide range of observing angles the influence of the circular polarised part of polarisation decreases the sensitivity of the measurement for the polarisation angle strongly. Under this conditions accurate data are limited to a small area of the CCD, where

the incident angle of the light wave is almost perpendicular. Since data evaluation requires an averaging about several pixels to decrease noise perturbations, a sufficient measurement for calibration can not be achieved.

2. For the IMSE-system with current system parameters the circular polarisation is strongly weighted by the spectral contrast function of the system in comparison to the information of the linear polarisation. This enhances the effect mentioned in point 1. A change of the delay plate thickness influences the ratio of the spectral functions and can be used to optimise the system by making the circular spectral function to vanish. The optimised system gives theoretically accurate results for a wide range of γ and y. However, the optimisation is only valid for a narrow interval of values for the magnetic field strength and small deviations effect the measurement strong enough, that the accuracy is too small for calibration. Only for small values of γ might a system optimisation be useful.

3. In general, the effect of small filter asymmetry over the Zeeman-multiplett is low in comparison to the other influences mentioned before. The effect only becomes dominant for the optimised IMSE-system and for nearly perpendicular observation. A decreasing of the I^{π}/I^{σ} ratio will not increase the error of the polarisation angle θ_S and is therefore of minor interest.

4. A realistic chance of calibration of the IMSE-system at a tokamak is only given for vanishing circular polarisation by nearly perpendicular observation. Under this condition a system and filter optimisation is useful to improve the accuracy of the measurement.

7 Simulations for the IMSE - diagnostic installed on tokamak ASDEX Upgrade

In the last chapter the general response of the IMSE-system to Zeeman H_α-emission was calculated and physically interpreted. This chapter investigates the response of the IMSE-system to the Zeeman H_α-edge emission if it is installed at the MSE-port at ASDEX Upgrade. To compare measured data with theoretical assumptions a forward model was written using the open source coding language *Python*. The last chapter has shown, that the polarisation angle can not be extracted accurately enough for calibration. A forward model is an alternative way to realise calibration, if a fitting of the simulates data to the measured data is possible. The following chapter starts with an overview of the main input data for the simulation. Afterwards the basic program structure is introduced with regard to the approximations used. A discussion of the main simulations results follows, which are interpreted in comparison to measured data.

7.1 Input data for simulation

Magnetic field data from static equilibrium

To simulate the stokes vectors of the Zeeman emission from the plasma edge, the direction of the magnetic field is needed. The data of the magnetic field are obtained from the CLISTE equilibrium code (CompLete Interpretive Suite for Tokamak Equilibria) [31]. The CLISTE-code solves the Grad-Shafranov equation (14) numerically to find a sufficient poloidal flux function $\Psi(R, z)$ for each pulse in ASDEX Upgrade during data evaluation. The following Grad-Shafranov equation was already introduced in section 1.3:

$$R\frac{\partial}{\partial R}\left(\frac{1}{R}\frac{\partial \Psi}{\partial R}\right) + \frac{\partial^2 \Psi}{\partial Z^2} = -\mu_0 R^2 \frac{dp}{d\Psi} - \frac{1}{2}\frac{d(RB_\phi)^2}{d\Psi} \tag{76}$$

To solve this equation the total derivations of the pressure and the toroidal field on the right side are linearised by the two fixed functions Λ, Υ dependent on Ψ. They are also basis functions for the toroidal field current j_ϕ. The parametrisation is then given by:

$$\frac{\partial p}{\partial \Psi} = \Sigma_i c_i \Upsilon_i(\Psi) \qquad \frac{\partial B_\phi}{\partial \Psi} = \Sigma_i k_i \Lambda_i(\Psi) \tag{77}$$

Based on the currents in the poloidal field coils and a fixed in-vessel structure the code calculates a toroidal current density profile for j_ϕ by setting the parameters c_i and k_i. The current density is compared to measured data from external magnetic field diagnostics. The iterative code varies the parameter c_i and k_i to optimise the fit of j_ϕ between measured data and code results by minimise the least square error. The Code also outputs other parameters like the magnetic field $\vec{B}(R, \phi, Z)$ for the calculated equilibrium. The given results are especially accurate for the outer plasma edge, where the measured boundary conditions for the code are well known. An example for such a two-dimensional poloidal flux function is illustrated in Figure 37. Here $\Psi_{Norm.}(R, Z)$ is the normalised flux function where $\Psi_{Norm.}(R, Z) = 0.0$ denotes the magnetic axis and $\Psi_{Norm.}(R, Z) = 1.0$ the last closed flux surface determined by the separatrix inside the vessel.

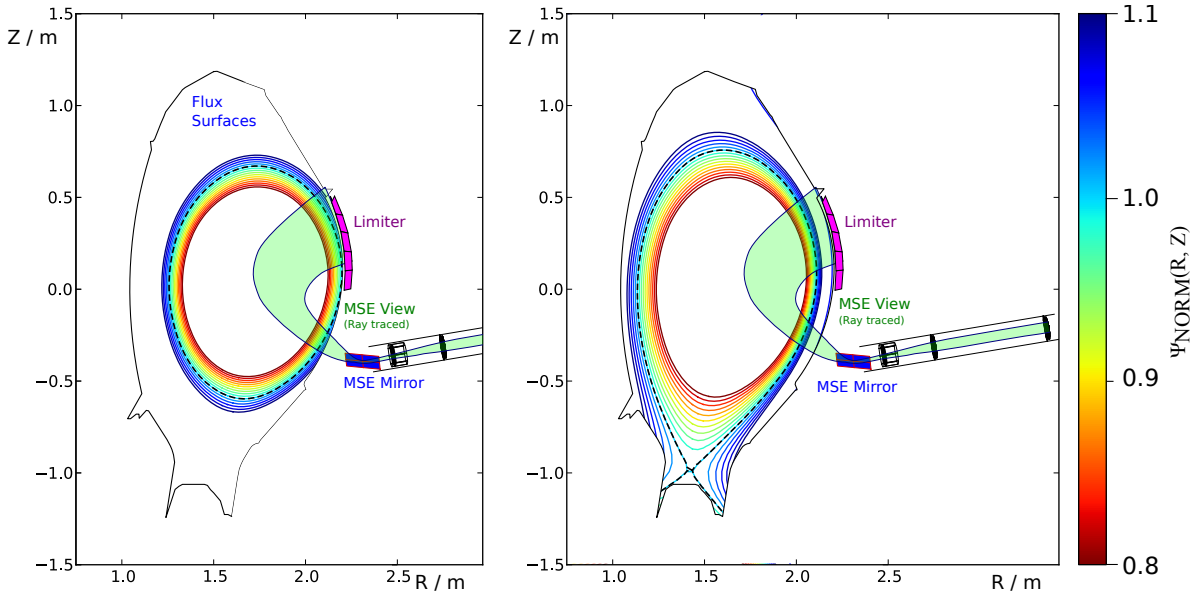

Figure 37 – Exemplary structure of the normalised two-dimensional flux surfaces $\Psi_{Norm.}(R, Z)$ at ASDEX Upgrade calculated by the equilibrium code CLISTE for limiter configuration (left) and seperatix configuration (right)

Viewing geometry of the camera

The second data set needed for simulation is the viewing direction of the IMSE-system relative to the magnetic field. Since the IMSE-system is mounted at the MSE-optics, the emission passes through different optics before it is measured by the IMSE-system (Figure 9). All these optics, especially the mirror and the protection cover, influence the polarisation angle, which means that there is a difference between the global defined polarisation angle for the tokamak and the polarisation angle measured by the IMSE-system. The program will calculate the polarisation angle first for the global tokamak frame and the influence of the MSE optics is added afterwards. Therefore, each pixel on the camera, where i and j is the pixel-number in x-direction and y-direction, can be related to a viewing vector $\vec{v}_{ij}$ pointing from the surface of the mirror into the plasma vessel. To measure the vectors $\vec{v}_{ij}$, a normal picture was taken with the CCD-camera at the end off the MSE-optics. In-vessel components, which are accurately identifiable on this calibration picture, serve as fixed markers and their coordinates inside the tokamak were measured geometrically. Together with the reflection point of the image on the mirror $\vec{x}_O$, which is approximately assumed to be the same point for all pixels, the viewing vectors were calculated and the remaining viewing vectors were interpolated. Figure 38 shows the calibration pictures. The left part shows a photo with the marked calibration points. These are the same points observed with the IMSE-diagnostic through the MSE optics in the right picture. A geometric calculation of the intersection points of the viewing lines and the neutral beam also allows a rough of the absolute polarisation direction. However, this is not nearly accurate enough for the IMSE, so a new way of calibration is required, which can be done in-situ during operation and has a higher accuracy.

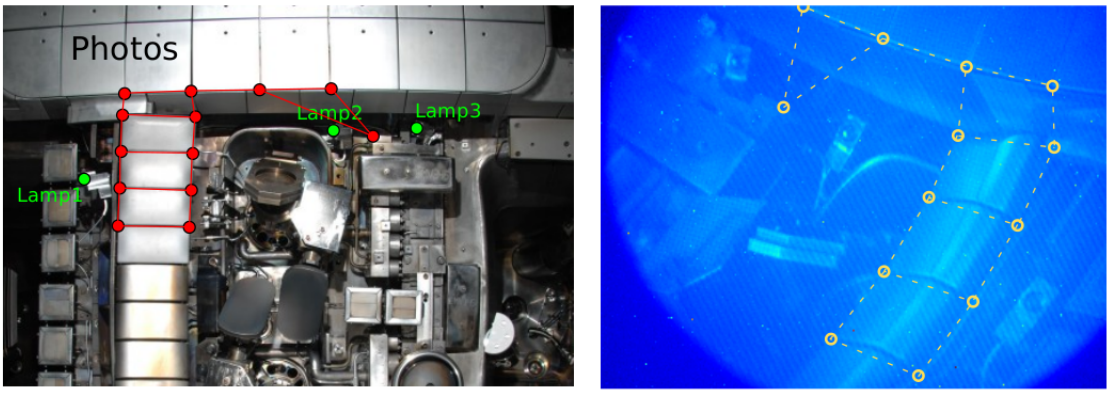

Figure 38 – Photo with marked calibration points at the vessel surface (left) and picture taken with the CCD-camera through the MSE-optics with identical calibration points (right).

Intensity distribution of the H_α-Zeeman-edge emission

For a complete simulation, the intensity distribution and the position of the Zeeman H_α-edge emission must be known. In principle, the absolute intensity is not important for the measurement, because it will be eliminated during data evaluation, but since the IMSE-system measures the polarisation line integrated along each viewing direction, the measured polarisation angle depends on the three-dimensional intensity distribution. For the standard measurement with the IMSE-system, the source of emission is well localised, since the neutral beam position is known. In contrast to the beam emission, the position of the Zeeman H_α-edge emission changes during the ramp-up phase as shown in Figure 39. Only for the case, where the emission is strongly localised near the limiter (upper right part in Figure 39), an intensity distribution can be roughly decided. For the other cases several other measurements are needed to find a sufficient three-dimensional intensity distribution, since the line integrated data from the IMSE-system do not include information about the intensity distribution in the third dimension. For this reason the simulation and measurements in this thesis are focused on data, where the emission is localised at the limiter. In zero order the intensity distribution can assumed as a thin layer at the plasma edge, which means that the emission is represented by only one point for each viewing line with similar value of $\Psi_{Norm.}(R, Z)$. The next order is an exponential decay of the emission in direction of decreasing $\Psi_{Norm.}(R, Z)$ due to reionisation of the recycled hydrogen neutrals. In principle, the intensity distribution on a fixed flux surface is not important, because their is no line integration in this direction and the total intensity distribution over the measured picture is irrelevant for the measurement. Nevertheless, it is possible to model a full intensity distribution for the limiter case using Gaussian and linear functions for a fixed flux surface. The program includes these different intensity models, where several variable parameters e.g. for the number of points per viewing direction and for the slope of the exponential decay. For a very narrow thin layer or a very strong exponential decay, the changes of the polarisation angle along the line of sigh are very small, so only for high accuracy e.g. for a calibration, the intensity distribution must be accurately known. For a rough physical simulation, this is not of high importance. The viewing lines also intersect with the plasma edge a second time directly in front of the mirror.

Especially for the limiter case, it can be assumed that the influence of possible Zeeman-emission from this position is small against the strong intensity from near the limiter. Therefore, it is totally neglected in the simulation.

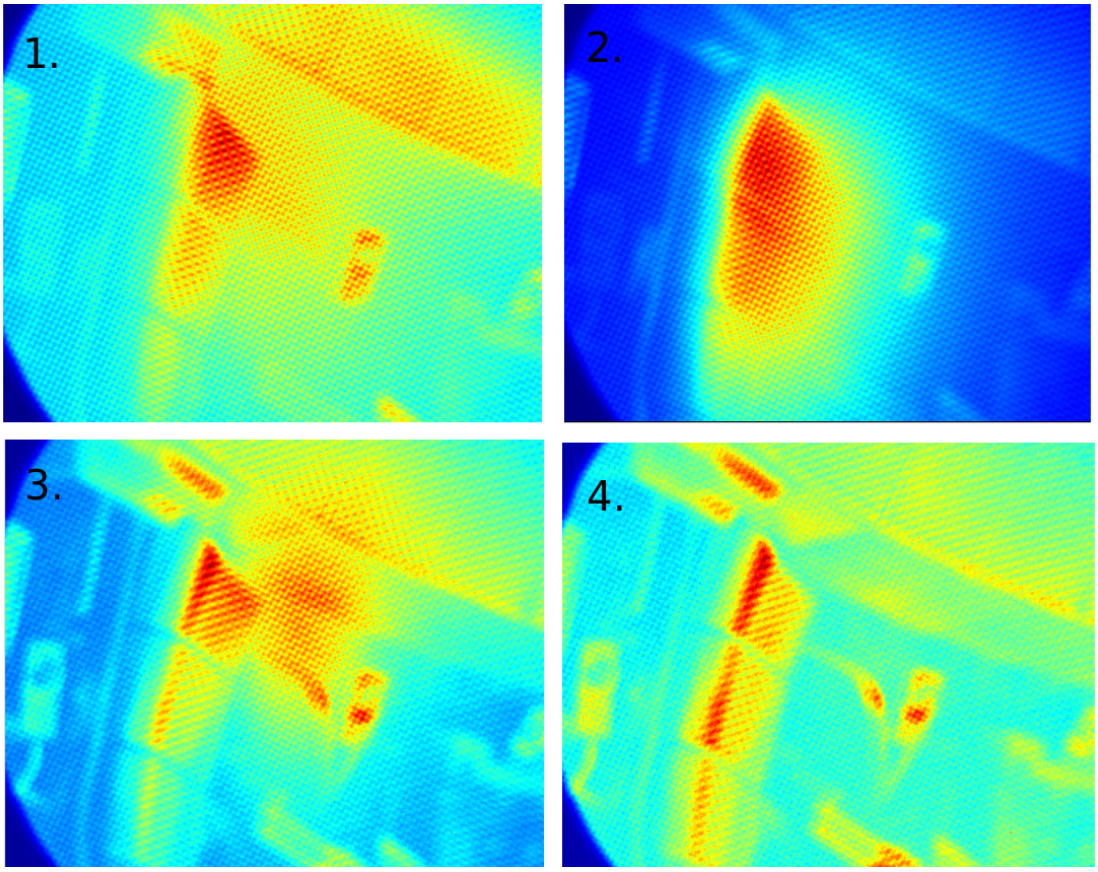

Figure 39 – IMSE-images of the Zeeman-emission in chronological order with changing intensity distribution during the current ramp up.

Value of the energy splitting by the Zeeman-effect

Since the neutral particles, which emits the H_α-light, are concentrated in a thin plasma edge layer near the limiter, the magnetic field strength is assumed to be constant at all coordinate points along the viewing direction. The constant value $|\vec{B}|$ and therefore the fixed frequency splitting are estimated for each pulse.

7.2 Program structure

In this section the main calculation steps of the code are shortly described. To each pixel on the CCD-camera belongs an integral over the intensity weighted stokes vectors along each viewing line $\vec{v}_{ij}$. For a numerical simulation discretisation is necessary, so the integral is replaced by a sum over intensity weighted stokes vectors on fixed points $\vec{x}^k_{ij} = (x^k_{ij}, y^k_{ij}, z^k_{ij})$, where k is the number of points per viewing line.

$$\vec{s}^{tot}_{ij} = \int \vec{s}\ I\ d\vec{v}_{ij} = \Sigma_k\ \vec{s}(\vec{x}^k_{ij})\ I(\vec{x}^k_{ij}) \tag{78}$$

These define a three-dimensional grid, where $I(\vec{x}_{ij}^{k})$ denotes the modelled intensity distribution and $\vec{s}(\vec{x}_{ij}^{k})$ is the Stokes vector at each point of the grid. It is convenient and physically reasonable to choose these discretesation points in such a way, that they belong to constant differences of Ψ (i.e. $\Psi(\vec{x}_{ij}^{k}) - \Psi(\vec{x}_{ij}^{k-1}) = \text{constant}$). To calculate the discrete grid the code uses linear and bilinear interpolation. In the first step a set of points for each viewing line obtained by linear parametrisation of each viewing direction as represented by following equation.

$$\vec{x}_{ij}^{m} = \vec{x_O} + m\vec{v_{ij}} \tag{79}$$

Then the poloidal flux function is calculated on each of these points $\vec{x}_{ij}^{m}$ using bilinear interpolation with the flux surface data from CLISTE. Therefore, the points on the viewing lines are transformed from the Cartesian to the cylindrical coordinate system. Afterwards a set of fixed values of $\Psi(\vec{x}_{ij}^{k})$ is chosen. The corresponding new grid points $\vec{x}_{ij}^{k}$ at each viewing line are obtained with linear spline interpolation, which is done for each of three coordinates and each viewing line separately. The accuracy of the new grid is sufficient enough for a basic physical investigation. In a last interpolation step the magnetic field direction $\vec{B}(R, \phi, Z)$ on each new grid point $\vec{x}_{ij}^{k}$ is calculated with linear spline interpolation for each coordinate separately. Since the change of the magnetic field direction between neighbouring points is small, the resulting magnetic field vectors are accurate enough. Afterwards the new grid points and the magnetic field directions at these are transformed back to Cartesian coordinates using the following relation for the magnetic field vectors:

$$\begin{aligned} B_x &= B_R\cos(\phi) - B_\phi\sin(\phi) \\ B_y &= B_R\sin(\phi) - B_\phi\cos(\phi) \\ B_z &= B_Z \end{aligned} \tag{80}$$

In the Cartesian system the global polarisation angle β and the the direction angle γ can be calculated. As explained in section 4.2 the definition of the polarisation angle requires a defined coordinate system for each viewing direction. Starting from the global z-direction $\vec{z}_G = (0, 0, 1)$ in the tokamak frame, the three-dimensional cartesian coordinate system is generated for each viewing direction by the normalised vectors $\vec{v}_{ij}, \vec{l}_{ij}^{A}$ und $\vec{l}_{ij}^{B}$. These are obtained by using following relations:

$$\vec{l}_{ij}^{A} = \frac{\vec{e}_{ij}^{A}}{|\vec{e}_{ij}^{A}|} \qquad \text{with} \qquad \vec{e}_{ij}^{A} = \vec{v}_{ij} \times \vec{z}_G \tag{81}$$

$$\vec{l}_{ij}^{B} = \frac{\vec{e}_{ij}^{B}}{|\vec{e}_{ij}^{B}|} \qquad \text{with} \qquad \vec{e}_{ij}^{B} = \vec{v}_{ij} \times \vec{l}_{ij}^{A} \tag{82}$$

In this definition the vector $\vec{e}_{ij}^{B}$ is the vector perpendicular to the line of sight that is closest to the vertical direction $\vec{z}_G = (0, 0, 1)$ in the global tokamak frame. The angles γ_{ij}^{k} and β_{ij}^{k} at each grid point are then given by the following equation, where $\vec{B}_{ij}^{k} = \vec{B}(\vec{x}_{ij}^{k})$ is the magnetic field on the grid.

$$\cos(\gamma_{ij}^{k}) = \frac{\vec{B}_{ij}^{k} \cdot \vec{v}_{ij}}{|\vec{B}_{ij}^{k}|} \qquad \text{and} \qquad \tan(\beta_{ij}^{k}) = \frac{\vec{B}_{ij}^{k} \cdot \vec{l}_{ij}^{A}}{\vec{B}_{ij}^{k} \cdot \vec{l}_{ij}^{B}} \tag{83}$$

The Stokes vector at each point can be calculated directly from these angles using (**??**). Afterwards, the Stokes vectors are weighted by the intensity distribution and are added for each viewing direction according to equation (78), which leads to the global total Stokes vector for each pixel on the image s^{tot}. From the global total Stokes vector, the line integrated polarisation angle β^{tot} and the line integrated value of γ^{tot} across the picture can be obtained, which represent the measurable polarisation state of the π-component.
Until now the programme only calculates the global polarisation angle β^{tot}. The polarisation angle the IMSE-system at the end of the MSE-diagnostic measured is denoted as θ_S^{tot}, which is the polarisation angle of the π-component relative to the Savart plate. The difference between both frames of polarisation can be split in two terms as follows:

$$\theta_S^{tot} = \beta^{tot} + \Delta\beta_F + \Delta\beta_{M+C} \tag{84}$$

The both term will be explained more in detail now:

1. The term $\Delta\beta_F$ describes the influence of the Faraday effect, which effects the polarisation angle of the light passing through the protection cover in the vessel wall. The Faraday effect always rotates the polarisation direction of polarised light, if the light is passing through a dielectric medium with magnetic field component parallel to the propagation direction inside. $\Delta\beta_F$ is different for each viewing direction and depends on the magnetic field strength, the length of the lights path through the media and the Verdet constant. The Verdet constant depends on the dielectric media and the wavelength of the light. The data used in the program are extracted from a ray trace program [27] that describes the polarisation state of the light passing through the entire MSE-optics. Measured data for the Faraday rotation in the protection cover have shown a accurate agreement with these calculated values. The changes of the polarisation angle through the Faraday are smaller then 1° [11].

2. The term $\Delta\beta_{M+C}$ is the main geometric term effecting the polarisation angle and depends on the influence of the reflection of the polarised light at the dielectric mirror and the rotation of the birefringent plates around the optical axis of the MSE-optics. The value of $\Delta\beta_{M+C}$ is also different for each viewing line, since the definition frame ($\vec{l}_{ij}^{A}$ and $\vec{l}_{ij}^{B}$) for each pixel is different. It can be estimated from comparison with the ray trace program. Therefore, several reference vectors were defined in the global tokamak frame and are projected in the polarisation plane orthogonal to the viewing vector. The ray tracer calculates the transformation of the projected reference vectors to the frame of the Savart plate. The comparison of the reference vectors in both frames allows the geometrical calculation of the values for $\Delta\beta_{M+C}$. The quantity $\Delta\beta_{M+C}$ is the desired parameter for calibration by fitting the simulated data to measurement results.

The angle γ^{tot} should not be influenced when the polarised light passes the MSE-optics, since Faraday rotation does not effect circular polarisation. The used special dielectric mirror is assumed not to change the ratio of linear and circular polarised light, since it the dielectric mirror is optimised to have total reflectance for the parallel and the perpendicular component of the incident wave for the used wavelength range.

With the angles θ_S^{tot} and γ^{tot} the simulated values for the Stokes vectors measured by the IMSE-system can be obtained using (3). Starting from this the image equation for each component of the Zeeman-multiplett can be calculated separately with equation (38), where the characteristic frequency of the component is estimated from the calculated energy splitting due to the Zeeman effect. For the full image of the entire multiplett the three single images are added with regard of the components relative intensities. The program also includes a demodulation tool to obtain the Fourier components, which can be used for simulated and for measured data. For the demodulation the two-dimensional Fourier transform algorithm in $Python - Numpy$ is used. The code also includes the different equations for data evaluation of the polarisation angle θ_S^{tot} and all three case of FLC modi. A separate tool is implemented to compare the simulated and demodulated Fourier components with the analytically calculated terms in equation (66). This allows to prove the accuracy of the demodulation tool.

7.3 Comparison of simulated and measured results

This section will present the main results of the full simulation code. The results will be analysed in comparison to the theoretical results from the former chapter and will be interpreted with regard to measured data. A typical measured IMSE-image of the Zeeman edge emission located near the limiter is illustrated in Figure 40 in comparison with the corresponding simulated image.

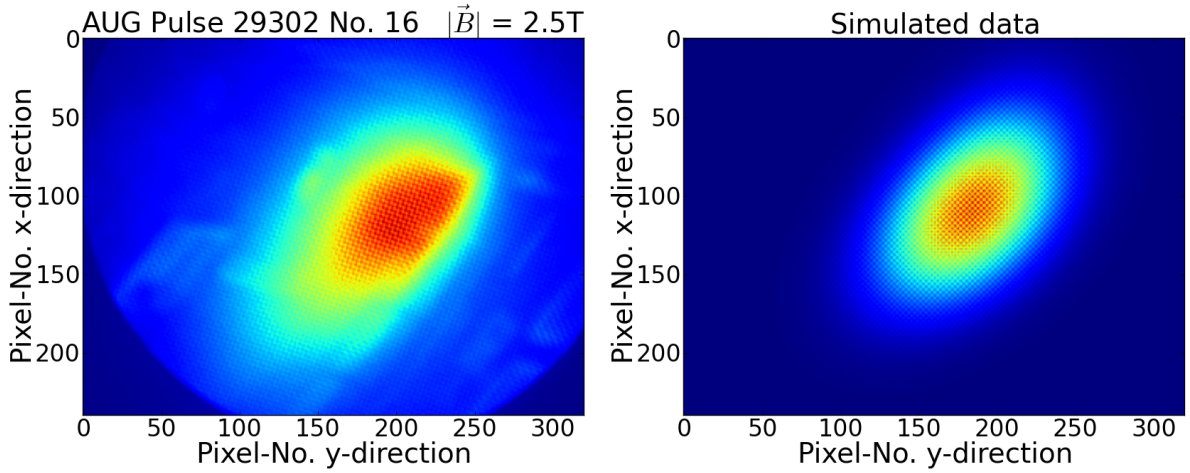

Figure 40 – IMSE-image of the Zeeman-edge emission near the limiter in ADEX Upgrade (left) and corresponding simulated image (right).

The intensity distribution for the simulated image in Figure 40 was chosen to have a strong exponential decay from the limiter inside the plasma in the narrow edge area of $0.95 \leq \Psi_{Norm.}(R, Z) \leq 1.0$ with points per viewing line k = 10. As already explained the intensity distribution on a fixed flux surface is of minor interest, since intensity variations cross the image are eliminated during data evaluation. For the chosen grid discretisation a change of the angles θ_S^{tot} and γ^{tot} through the intensity distribution can be only introduced, if the local angles change rapidly across different flux surface. Important for the discussion of calibration are the simulated values of the angle θ_S^{tot} and γ^{tot}, which are used to calculate the simulated image in 40 (right). The results for θ_S^{tot} and γ^{tot} are presented in Figure 41. The right part of Figure 41 shows the variation of γ^{tot} in the range between 30° and 40°. The results in the last chapter have already shown, that for the current configuration of the IMSE-system and such values of the observation angle γ^{tot} the measurement of the Zeeman emission will not give accurate results for the polarisation angle θ_S^{tot}. The reason therefore is the high weighted influence of the circular polarisation, which prevents a possibility of calibration. Since the Zeeman edge emission is assumed to be localised at a narrow edge layer near the limiter, changes of the integrated polarisation angle θ_S^{tot} are small for different exponential decays of the intensity distribution. Especially in comparison to the deviation introduced by the circular polarisation during data evaluation the effect of a non optimised intensity distribution for the simulation is negligible low. A very accurate intensity distribution is therefore not necessary for a general physical discussion and interpretation of simulation results in this chapter. In the left part of Figure 41 the simulated values of the polarisation angle are shown, which vary between 0° and 15° in the center of the image. The range of the values for

θ_S^{tot} and γ^{tot} match the geometrical expectations from the ray trace program. If instead of the former case, the Zeeman-edge emission is assumed to come only from one constant flux surface $\Psi_{Norm.}(R, Z) \approx 1.0$ near the limiter, the values of θ_S^{tot} and γ^{tot} do not change significantly.

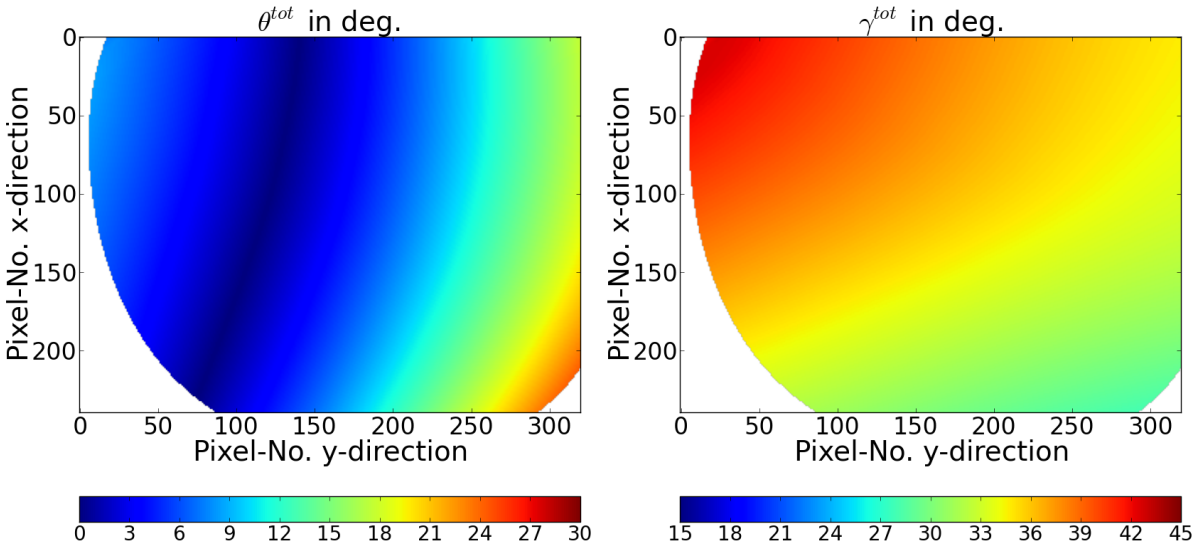

Figure 41 – Simulated values for the line averaged polarisation angle θ_S^{tot} and observation angle γ^{tot} for the measurement of pulse AUG 29302 with the IMSE-system.

The simulated values for θ_S^{tot} represent the polarisation angle as measured by the IMSE-system and are used to calculate the simulated image in Figure 40. In the next step the data evaluation for the simulated IMSE-image in 40 is made using the demodulation tool of the program. The demodulated polarisation angle from the the simulated image is denoted as θ_S^{theo} and the results are illustrated in Figure 42.

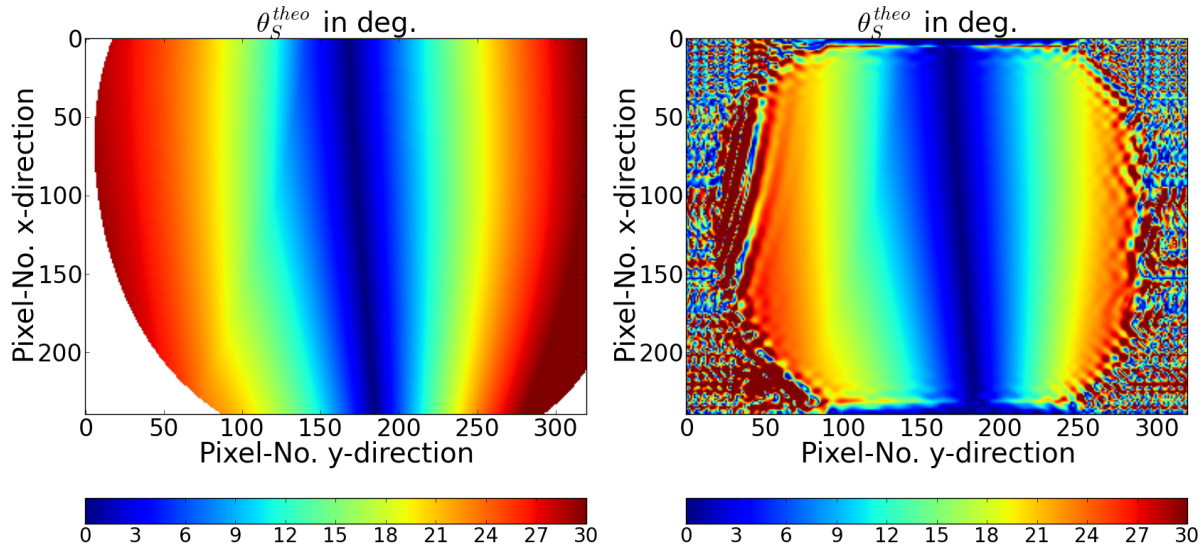

Figure 42 – Values for the polarisation angle θ_S^{theo} from from analytical calculation (left part) and from demodulation of the simulated IMSE-image (right part)

The equation (69) is used to obtain the polarisation angle from the Fourier components, since it was shown in the last chapter, that this is the correct equation for the current IMSE-system configuration and a magnetic field strength of $|\vec{B}| = 2.5$ T. The only exception are for values for $\gamma \approx 90°$. In this case the values of γ^{tot} are far away from this limit. The right part of Figure 42 shows the results for the polarisation angle θ_S^{theo} calculated with the full demodulation tool using the FFT algorithm. For the results in the left part of Figure 42 the Fourier components are calculated with the analytical equations (66) directly from the Stokes parameters. The comparison between both results shows, that the demodulation tool gives the same value for θ_S^{theo} in the center of the image as expected analytically. The oscillations at the edge of the demodulated image are an numerical artefact, which is caused by the selection of the Fourier components during the demodulation process. In the Fourier image the Fourier components are broadened peaks. The sides of this peaks are cut off of by selection the Fourier component. The shape cut and the small missing part of the Fourier component lead to small oscillations at the edge of the demodulated image after the inverse Fourier transform is performed. The results show a distinct deviation between the ideal polarisation angle θ_S^{tot} in Figure 41 (left) and the demodulated polarisation angle θ_S^{theo} in 42 (left). To analyse this more in detail the following Figure 43 shows the absolute difference between both values. The deviation of the polarisation angles in Figure 43 show the theoretically expected strong dependence on y, which is on the horizontal axis in Figure 43. For a narrow area around $y = 0$ mm (Pixel-No. 160) the difference between θ_S^{theo} and θ_S^{tot} is close to zero, which matches the theoretical expectations introduced in chapter 6.2. For measurements of the polarisation angle or for calibration the geometry of observation via the MSE-port at ASDEX Upgrade is inapplicable, since the circular polarised part for the $\sigma^{\pm}$-components of the Zeeman multiplett perturb the measurement strongly.

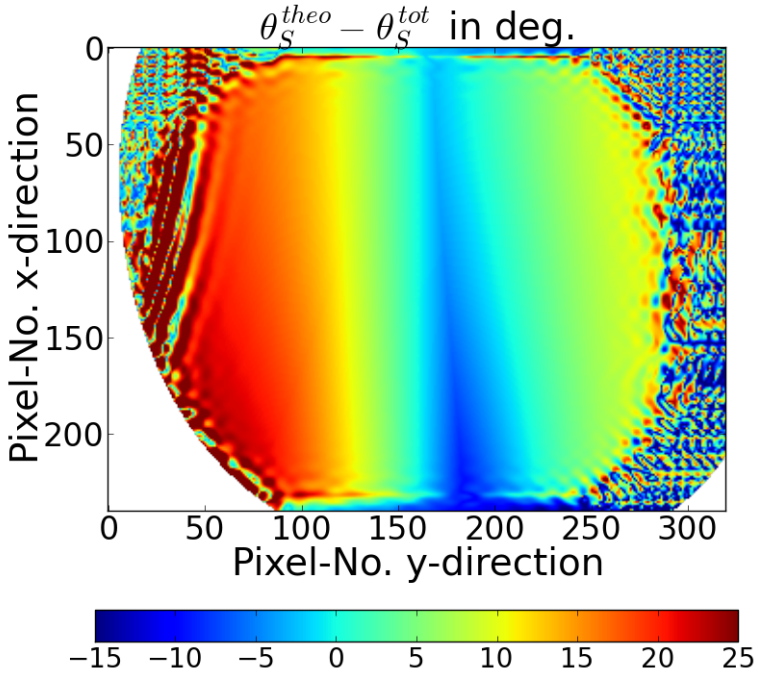

Figure 43 – Difference between simulated line integrated polarisation angle θ_S^{tot} and the demodulated polarisation angle from the simulated IMSE-image θ_S^{theo}

After discussing the simulated results from the program, now follows an investigation of the measured IMSE-image in Figure 40 (left). From demodulation and data evaluation with equation 69 the polarisation angle from the measured data $\theta_S^{measured}$ is obtained and the results are presented in Figure 44 (left). The right part in Figure 44 illustrates the difference between measured polarisation angle $\theta_S^{measured}$ and expected value θ_S^{tot}.

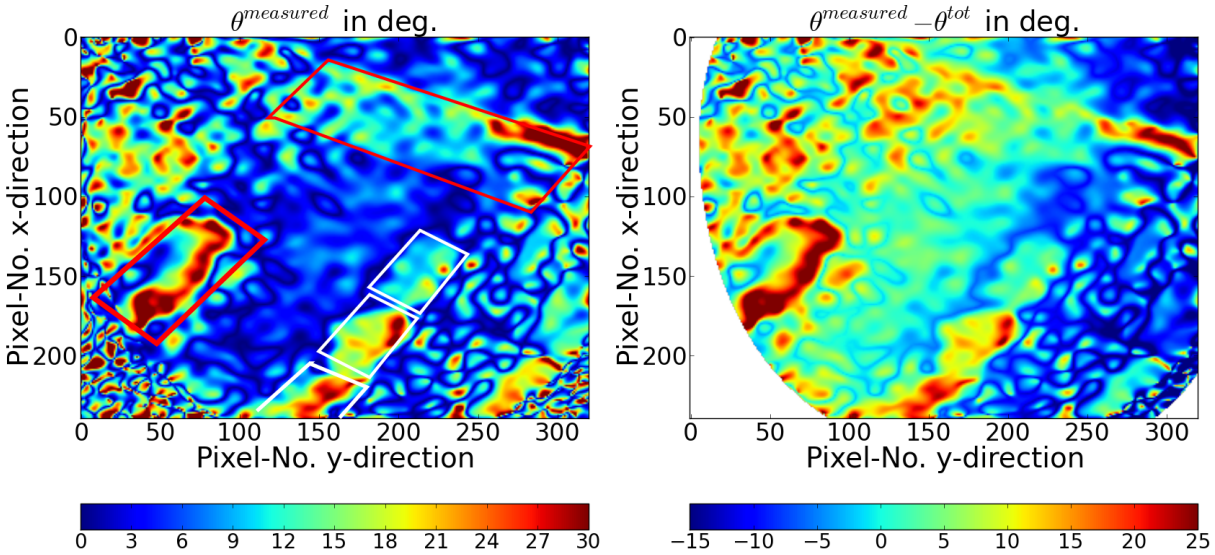

Figure 44 – Measured polarisation angle $\theta_S^{measured}$ for pulse AUG 29302 (left) and difference between $\theta_S^{measured}$ and the simulated polarisation angle θ_S^{tot} (right). The marked areas are the limiter position in white and different metal plates (red).

In comparison to the simulated values θ_S^{theo} in Figure 42 the polarisation angle from the measurement $\theta_S^{measured}$ shows not the expected characteristic dependence on y. In the center of the measured and demodulated image the values of the polarisation angle are seems to be close to the expected value, which is illustrated in Figure 42 (right), but the dependence of the deviation on y is quite different as for the simulated expectation. The marked areas in Figure 42 are the limiter position (white) and the other metal plates (red). The data from this regions should be ignored, since reflections perturb the results. The simulation therefore does not match the experimental data as expected and it is therefore not yet clear if the apparently good values at the center of the demodulated IMSE-measurement are significant or only incidentally correct. The experimental results also show high local variations in order of some degrees as a results of signal noise, which is much stronger then for the standard MSE-measurement. A physical reason are stronger local fluctuation effects for the Zeeman edge emission in comparison to the well localised and stable neural beam emission. The strong influence of the signal-to-noise ratio is a new reason for the impossibility of an accurate calibration. The deviation between simulated and measured data described here are representative of several measurements of different pulses at ASDEX Upgrade. To find the reason for the deviation of simulated and measured data different possible reasons will be investigated in the next section.

7.4 Discussion of reasons for strong deviations

The results in the last section have shown a fundamental difference between measured data and a full simulation of the IMSE-system installed at ASDEX Upgrade. Therefore this section will consider various physical effects more in detail, which may cause this deviation.

Influence of different filters

As already suggested, during the theoretically description of the IMSE-systems response to the Zeeman emission, the use of an unsuitable filter can introduce strong deviations of the measured polarisation angle. For the measurement leading to the results in the former section a filter was used, which is optimised for measuring the MSE-multiplett. A change of the filter during measurements was not possible for early IMSE-measurement, but a filter changer was added later to the IMSE-system. The main focus during this early campaign lay on test measurement for the MSE-multiplett and the Zeeman emission was only observed secondarily. For later measurements, an available 'H_α'-filter was used observing the Zeeman edge emission, and before for the last campaign at ADEX Upgrade a special interference filter optimised to the Zeeman multiplett was purchased. To investigate possible effects by using the different filter, the transmittance of all filter was measured with a well calibrated optical spectrometer. The results are shown in Figure 45 for perpendicular incident of the light relative to the filter interface.

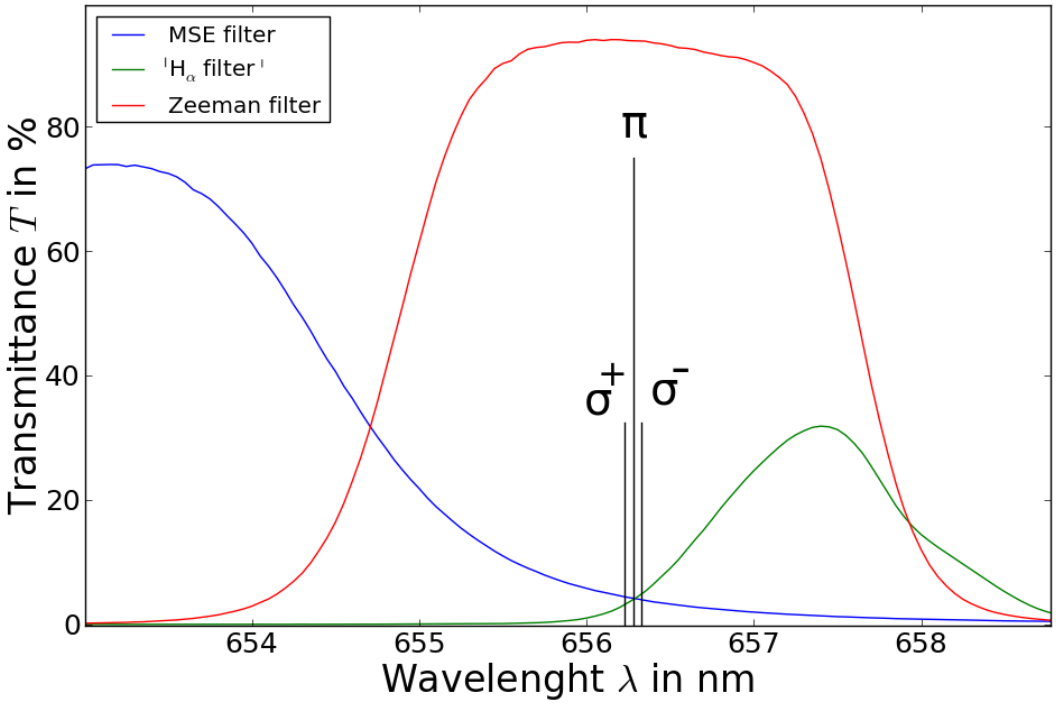

Figure 45 – Transmittance of different filter for the wavelength range of the Zeeman multiplett with splitting caused by a magnetic field strength of $|\vec{B}| = 2.5$ T

The optimised Zeeman filter has a high transmittance of nearly 95 % at the wavelength range of the Zeeman multiplett, whereas the 'H_α'-filter and the MSE filter have a low transmittance of around 7 %. Since absolute intensities of the Zeeman multiplett are not expected to change

the measurement fundamentally, it is mainly important to consider the change of the intensity ratios due to filters. The splitting due to the Zeeman effect for magnetic fields strength between 1.5 T and 3.5 T lies in a small range of 0.03 - 0.07 nm, so large differences of the intensities of the $\sigma^{\pm}$-components are not possible. The results in Figure 45 illustrate, that the optimised Zeeman filter is approximately constant over the Zeeman multiplett. For the MSE-filter, the intensity ratio of the σ-components is $I^{\sigma^+}/I^{\sigma^-} = 1.05$ and $I^{\sigma^+}/I^{\sigma^-} = 0.8$ for the 'H_α'-filter for perpendicular incident angle of the incoming light to the filter surface. Since the angle of incident α_I changes across the image, it was necessary to measure also the angle dependence of the transmittance for all filter to implement a complete two-dimensional filter function to the simulation code. With increasing incident angle the area of high transmittance is increasingly blue shifted, whereas the absolute transmittance decreases slowly and the filter shape becomes broader. For the simulation the use of different filters changes the results of the demodulated polarisation angle θ_S^{theo} significantly, where the accuracy is as expected much higher for the Zeeman filter as for other filters. For the Zeeman filter the $I^{\sigma^+}/I^{\sigma^-}$ is expected to be nearly constant for different incident angles, whereas for the H_α-filter and the MSE filter this ratio changes cross the image. Measurements at ASDEX Upgrate have not shown a significant change of the measured polarisation angle $\theta_S^{measured}$ for the use of different filters. The measured results for the other filter were nearly the same as for the MSE-filter, where the measured polarisation angle was already presented in Figure 42. For this reason filter effects are not the main influence factor causing the deviation between measured and simulated results. To exclude the effect of filters the optimised Zeeman filter was used exclusively in the further test measurements.

Change of polarisation angle by system rotation

In Figure 42 the obtained polarisation angle does not show the expected strong variation cross the image. To investigate the significance of the measured results it is reasonable to prove the response of the IMSE-system to a marked change of the polarisation direction. Since the IMSE-diagnostic measures the polarisation angle θ_S^{tot} relative to the frame of the Savart plate, a rotation of the entire IMSE-system around the optical axis of the MSE-optics at ASDEX Upgrade would add a constant offset to the polarisation angle. This was well proven for measurements of the MSE-multiplett. The value of the offset for the polarisation angle is directly given by the angle of rotation, but with regard to the fact, that the measured polarisation angle is only defined on the interval $[0°, 45°]$. In Figure 46 two IMSE-measurements of the Zeeman edge emission are shown for different pulses at ASDEX Upgrade. Between these measurements the IMSE-system was rotated by roughly 20° and the optimised Zeeman filter was used to exclude strong filter effects in both cases. Therefore, a significant change of the calculated polarisation angle was expected, but was not measured according to the results in Figure 46. The obtained polarisation angle lies for both pulses in the same range as already for the first measurement with the MSE filter in Figure 40. This means in conclusion, that the IMSE-system is empirically not sensitive for measuring the polarisation angle from the Zeeman edge emission at ASDEX Upgrade. From the theoretically calculations in chapter 6 it is already clear, that accurate values for the measured polarisation angle are not possible for an observation angle γ^{tot} between 30° and 40°. On the other hand total loss of sensitivity is only expected for observation parallel to the direction of the

magnetic field ($\gamma \approx 0°$), which is definitely not given for the current geometry of the MSE-optics. The theoretical results in chapter 6 have also shown, that the expected measured polarisation angle for nearly parallel observation is close to 45°, which is in comparison to the measured values in this section of $0° - 15°$ the other limit in the range of possible values for the polarisation angle.

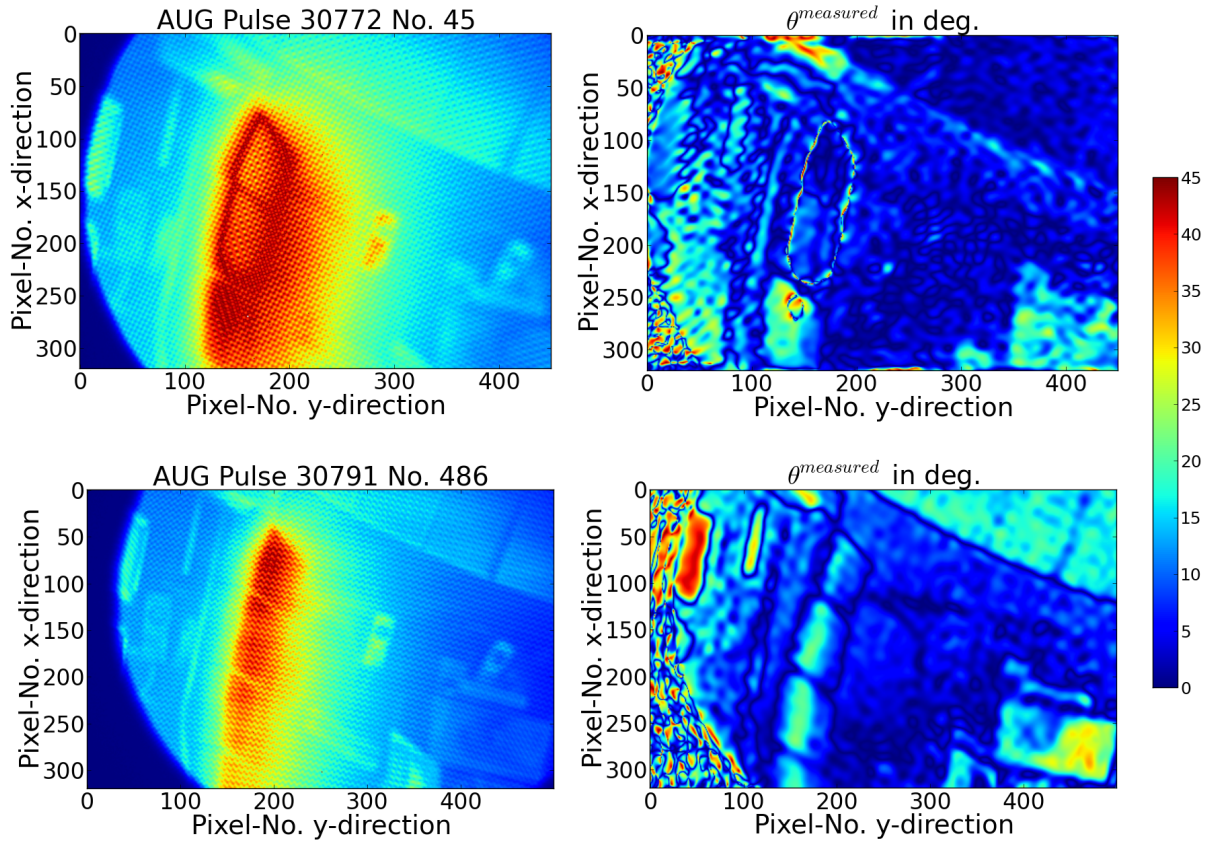

Figure 46 – Measurement of the polarisation angle $\theta_S^{measured}$ from the Zeeman edge emission for two different pulses at ASDEX Upgrade. Between the two measurements the IMSE-system was rotated by roughly 20° around the optical axis to introduce a significant change of the measured polarisation.

Influence of circular polarisation and non-statistical population of atomic states

In the last section is was already implied, that possibly the degree of circular polarisation is different in the measurements as considered for simulation. The theoretical discussion in chapter 6 has shown, that a direct measurement of γ or the ellipticity χ is not possible with the IMSE-system. To get an idea of the influence of circular polarisation for the measured data, it is useful to analyse the ratios of the Fourier amplitudes more in detail. Therefore the Fourier amplitudes were average over the areas of the measured image, which are not effected by reflections, for the simulated and the measured data. For the measurements the ratio $\langle |I(+,+)| \rangle$ / $\langle |I(+,0)| \rangle$ has typical values in the range of $1.5 - 2.5$, whereas for the simulation this ratio is with $\langle |I(+,+)| \rangle$ / $\langle |I(+,0)| \rangle \approx 7.5 - 11.0$ much higher. In both cases the ratio of $\langle |I(+,+)| \rangle$ / $\langle |I(+,-)| \rangle$ is nearly 1.1 . This significant difference of the amplitude ratios

was observed for several measurements and corresponding simulations under varying conditions like different magnetic field strengths and filters. The deviation of the amplitude ratio can be explained by a smaller degree of circular polarisation for the $\sigma^{\pm}$-components in measurements in comparison to the expected value from simulation. Since small variations of the γ^{tot} are not strong enough to explain such a huge deviation, two different other options for a smaller degree of circular polarisation must be taken into account. A non-statistical population of the atomic states can theoretically cause the deviation in the amplitude ratios. After theoretical estimations the state population must differ very strongly from the statistical case, which is physically less realistic for the H_α-edge plasma. The second option is a loss of degree of circular polarisation through the MSE optics. To investigate this more in detail a measured spectra of the Zeeman split H_α-edge emission can be useful. For technical reasons this could not be realised for this thesis, because of the small energy splitting high spectral resolution is required. A suitable spectrometer, which allows a measurement of the light passing the MSE-optics, was not available. The main problem with explaining the difference of the amplitudes with a smaller degree of circular polarisation is the fact, that this contradicts the theoretical assumption of an higher sensitivity for polarisation measurements. The results in the former section have shown, that this sensitivity is definitely not given for the measurements. Until now the reason for this inconsistency was not found. A possible solution can be a conversation from circular to linear polarisation, which will be described more in detail in the following section.

Influence of the dielectric mirror and coating on the surface of the protection cover

Until now the dielectric mirror was assumed not to change the ratio between linear and circular polarisation. A normal mirror would change this ratio due to different reflectance coefficients for the parallel and the perpendicular wave component relative to the incident plane. For the special dielectric mirror the both reflectance coefficients are nearly identical for the wavelength range of the MSE-multiplett. Only under this conditions a useful measurement with the MSE-system is possible. The wavelength of the H_α-emission is slightly away from this ideal range, so it was assumed, that this is still valid for the H_α-emission in ASDEX Upgrade. To prove this, a measurement of the mirror properties for different wavelength, incident angles and polarisation states is planed in the future. Until now an influence of the mirror can not be excluded totally. On the other hand a coating film emerges at the surface of the protection cover during plasma operation, which may also influence the polarisation. The possible influence of the coating layer was ignored until no and should be measured in the future to verify the expectation, that the coating has only a small effect.

Conclusion from measurements

The comparison between measurements and simulations have shown a fundamental deviation of the results. Especially the total absence of significance for the measurement of the polarisation angle was not expected for the simulated conditions, which seem to be reasonable from geometry estimations. During the work for this thesis several different influencing factors, which were introduced in this section, were analysed and discussed, but the main reason for this strong deviation between simulation and measured data was not found yet. Different factors like coating

of the protection cover and small filter asymmetries can now be excluded. On the other hand some possible reasons like the influence of the mirror or from the MSE optics demand a more precise investigations and additional measurements. To explain the main deviation between simulation and measurements, it is helpful to reduce the complex measurements at ASDEX Upgrade to a simpler test measurement at laboratory. This allows to produce light with well known polarisation state and therefore an experimental test of the response of the IMSE-system to simulated Zeeman emission with arbitrary polarisation angle θ_S and ellipticity χ representing the observation direction γ. Such an experiment would solve the fundamental question, whether the huge difference between simulation at ASDEX Upgrade and corresponding measurements is caused by a defective theoretically description of the IMSE-system or by unrecognised factors in the full simulation at ASDEX Upgrade. A first small experiment was already performed and the results will be described in the next chapter.

8 First laboratory test for the IMSE-system measuring Zeeman-emission

The last chapter has shown, that a match between the simulation for the IMSE-system and measurements of the H_α-edge emission at ASDEX Upgrade was not achieved. Since the physical reasons for the mismatch was not fully clarified by several test measurements at ASDEX Upgrade, simple test measurements with emission, which has well defined polarisation states are useful. Such a performance test was previously performed for a simulated simple MSE-spectrum [27], but is more complex for the Zeeman emission due to the additional circular polarisation. For the MSE performance test, the three spectral components were simulated using three identical light bulbs as light sources. The different wavelength were adjusted by using narrow filters, which were tilted relative to the incoming light. The spectral width of the filter was nearly the same as the spectral width of the MSE-components. It was already mentioned, that with increasing incident angle the wavelength range of high transmittance is blue shifted. To adjust the correct wavelength a spectrometer was used. The light from the three bulbs was linear polarised with polarisers with regards to the different polarisation angles for the σ- and π-components. To combine the three rays two semi-silvered mirrors were used. The superposed full simulated MSE-spectrum was focused onto a virtual image plane. Form there it is directly measured with the IMSE-diagnostic.

For the Zeeman emission, a simulation of all three components and therefore the entire Zeeman spectrum at once was not possible, since the additional degree of circular polarisation requires more optical plates then available. Therefore, each component was measured with the IMSE-system independently and the measured images were added later. This is the same way as the theoretical description was calculated. To simulate each component separately, a single light bulb was used. A lens behind the light bulb makes the light approximately parallel. The wavelength was again adjusted by tilting a narrow filter and measure the transmitted light with a spectrometer. Afterwards the light was linear polarised with a polariser to the required polarisation angle relative to the Savart plate. For the σ-components, a quater-wave plate was introduced into the beam path to add circular polarisation. Since this also influences the polarisation angle, the polariser was rotated to compensate the change. The entire optical setup is illustrated in Figure 47.

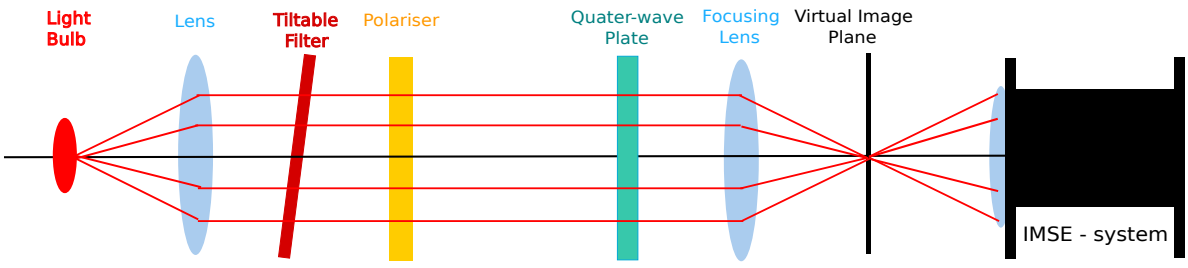

Figure 47 – Sketch of the experimental setup for the test measurement at laboratory

The recorded IMSE-images for each component where added at the PC with regard of the relative intensity for the Zeeman components. Therefore the absolute intensity of the images were normalised and multiplied with the new intensity factor. Since the intensities of the Zeeman component depend on the observation direction, the correct ratio can be estimated from the angle γ, using following relations with $I^{\pi} = 2I^{\sigma}$ (see section 6.1):

$$I^{\pi}_{exp} = I_{\pi} \sin^2(\gamma) \qquad \text{and} \qquad I^{\sigma}_{exp} = I_{\sigma}(1 - \cos^2(\gamma)) \tag{85}$$

The polarisation state of the simulated Zeeman spectrum was chosen to represent the expected geometry at ASDEX Upgrade. Therefore, a value of the observation angle was assumed with $\gamma \approx 35°$, which is a realistic value as illustrated in Figure 41. The corresponding ellipticity $\chi^{\pm}$ $= \mp 39.3°$ for the $\sigma^{\pm}$-components can be calculated with equation 31. The polarisation angle of the π-component was selected with $\theta_S \approx 26°$ and for the σ-components with $\theta_S + 90°$. This represents the expected polarisation angle at ASDEX Upgrade after the rotation of the IMSE-system around the optical axis of the IMSE optics. This polarisation angle represent a reasonable value, since the measured polarisation angles at ASDEX Upgrade were always smaller the 15°. That the system measures as expected is more convincing if a higher value for the polarisation angle is simulated to exclude accidentally fitting values. The simulated image for the added three Zeeman components and the corresponding two dimensional Fourier transform of the image are presented in Figure 48.

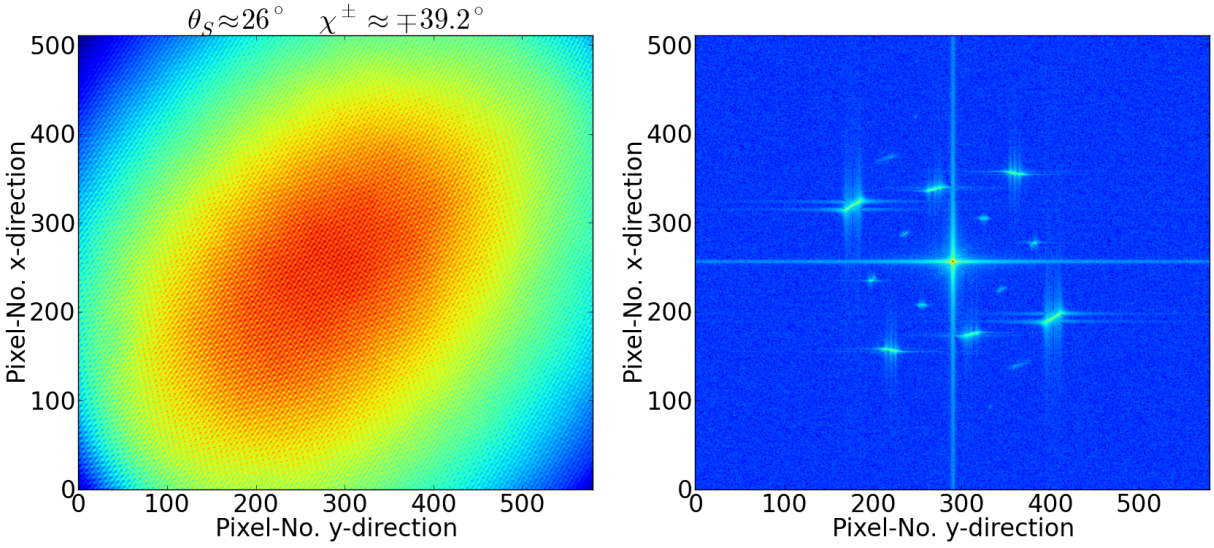

Figure 48 – Experimental test image for the IMSE-system measuring the full Zeeman multiplett with well defined polarisation angle θ_S and ellipticity χ (left) and corresponding two-dimensional Fourier transform (right).

Demodulation of the Fourier components and the calculation of the measured polarisation angle $\theta_S^{measured}$ with equation (69) give the results presented in Figure 49. For the center of the image the value of $\theta_S^{measured}$ is close to the expected value θ_S. Local variations at the center of the image are in the order of 2°. To the edge of the image the value for $\theta_S^{measured}$ decrease strongly

caused by the experimental setup, since deviations from the defined intensity ratio are given at the edges and also deviations of the component wavelengths due to steep incidence angles, when the light is crossing the filter. Therefore, the strength of the expected intrinsic error with y can not be checked for the test measurements. The result presented here should be understood as a first clue, that the IMSE-diagnostic measures Zeeman emission with arbitrary degree of circular polarisation as expected from mathematically calculations in this thesis. To make sure that the diagnostic works always as expected several additional test should be performed in the future to prove the sensitivity of the measurement to variations of the polarisation angle θ_S, the ellipticity χ and the energy splitting (i.e. magnetic field strength), which influence the spectral contrast functions. These tests are not part of this thesis for temporal reasons, since significant tests will require a high accuracy of the optical setup and time consuming analysis.

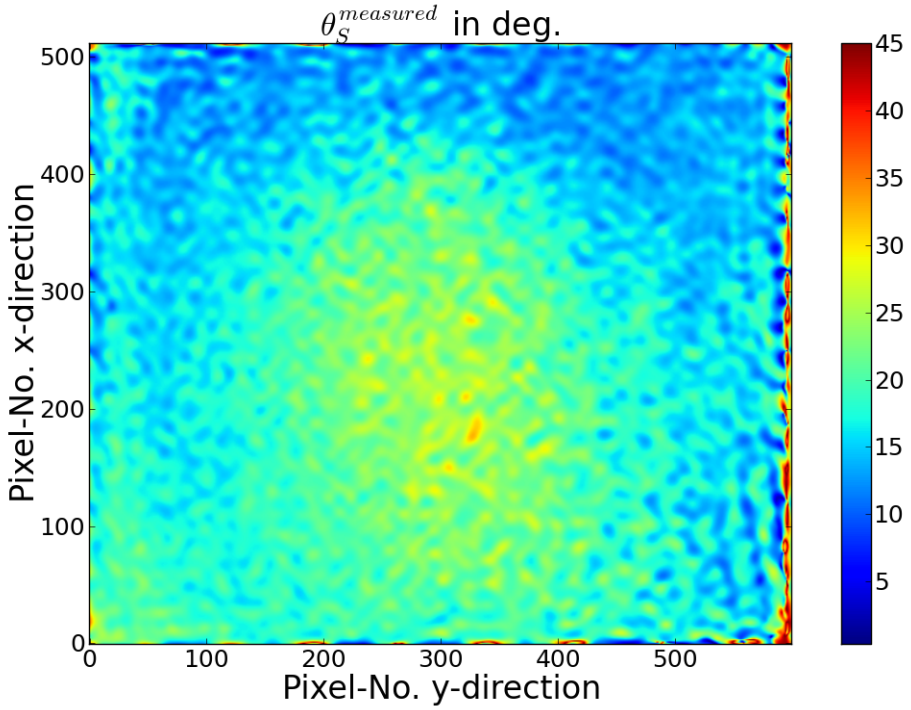

Figure 49 – Demodulated polarisation angle $\theta_S^{measured}$ from the measured test image in Figure 48.

Summary and Conclusions

The aim of this thesis was the investigation of the IMSE-system's response to the Zeeman H_α-edge emission at ASDEX Upgrade with regard to a possible use for calibration. Therefore, a general and complete theoretical description was developed, assesed and implemented in a forward model, which includes the full geometry for the diagnostic installed at ASDEX Upgrade. The theoretical investigation has shown that the emergence of circular polarisation for the $\sigma^{\pm}$-components of the Zeeman-multiplett changes the functionality of the IMSE-diagnostic substantially and makes a modification of the data evaluation inevitable. The dominant influence of circular polarisation restricts strongly the parameter range, for which an accurate measurement of the polarisation angle is possible for calibration. This effect is enhanced because the current system configuration is not optimised for the value of frequency splitting of the Zeeman-effect. A total optimisation of the system by changing optical components is theoretically possible, but is only valid for a narrow range of magnetic field strengths and is therefore only practically useful within limited parameter range. An nearly perpendicular observation direction is the only solution for accurate measurements, since the degree of circular polarisation vanishes completely. Unfortunately, this is not practically achievable. Although the polarisation cannot be clearly extracted, it remains in principle possible to perform the calibration by obtaining a match between the forward model and measured data. The full forward model has shown, that the viewing geometry at ASDEX Upgrade does not allow a reasonable calibration for the current IMSE-system. On the other hand, the implemented forward model does not match the measured data. An analysis and comparison of several measured and simulated data has led to an exclusion of all the most obvious physical reasons for this deviation. A simple performance test in the laboratory for fixed conditions, implies that the system operates as theoretically expected and an unconsidered effect causes the deviation of simulated and measured data for the full simulation of the IMSE-system at ASDEX Upgrade. To verify this, more performance test measurements with parameter variations should be performed in the future. The results of this thesis have significantly improved the understanding of the IMSE-diagnostic and will be used as part of the design for a new IMSE-system, which will be installed at ASDEX Upgrade in 2015.

References

[1] E. Rutherford. "Collision of α particles with light atoms - IV. An anomalous effect in nitrogen." *Philosophical Magazine*, vol. 37, pp. 581 (1919).

[2] H. A. Bethe. "Energy Production in Stars." *Physical Review*, vol. 55, pp. 434 (1939).

[3] C. von Weizsäcker. "Über Elem,entarumwandlung im Innern der Sterne." *Physicalische Zeitschrift*, vol. 38, pp. 176 (1937).

[4] "Property of the Max-Planck Institut für Plasmaphysik (IPP)."

[5] H.-S. Bosch and G. Hale. "Improved formulas for fusion cross-sections and thermal reactivities." *Nuclear Fusion*, vol. 32, no. 4, p. 611 (1992).

[6] O. N. Jarvis. "Nuclear Fusion." (2014).

[7] U. Stroth. *Plasmaphysik: Phänomene, Grundlagen, Anwendungen.* Vieweg+Teubner Verlag (2011).

[8] F. F. Chen. *Introduction to Plasma Physics and Controlled Fusion.* Springer Verlag (2006).

[9] U. Stroth. "Material zu Vorlesungen der Plasmaphysik." (2014).

[10] H. Y.-H. Yuh. *The Motional Stark Effect Diacnostic on Alcator C-Mod.* Ph.D. thesis, Massachusetts Institute of Technology (2005).

[11] T. Löbhard. *Kalibrierverfahren für die Motional Stark Effekt Diagnostik am Fusionsexperiment ASDEX Upgrade.* Master's thesis, TU München / IPP Garching (2011).

[12] M. J. Creese. *An Analysis of 2D Motional Stark Effect Imaging and Prospects for Determining the Structure of the Magnetics Field Inside a Tokamak.* Master's thesis, Australian National University Canberra (2009).

[13] R. Raimer, A. Dinklage, R. Fischer et al. "Spectrally resolved motional Stark effect measurements on ASDEX Upgrade." *AIP Review of Scientific Intruments*, vol. 84, no. 113503 (2013).

[14] O. Ford. "private communication." (2014).

[15] O. Ford. "Ray Trace Model for IMSE at ASDEX Upgrade."

[16] S. Huard. *Polarization of Light.* Wiley VCH (1997).

[17] M. Auzinsh, D. Budker and S. M. Rochester. *Optically Polarized Atoms.* Oxford University Press (2010).

[18] S. E. Segre. "A review of plasma polarimetry - theory and methods." *Plasma Physics and Controlled Fusion*, vol. 41, pp. R57 (1998).

[19] F. E. Veiras, L. I. Perez and M. T. Garea. "Phase shift formulars in uniaxial media: an application to waveplates." *Applied Optics*, vol. 49, p. 2796 (2010).

[20] H. Haken and H. C. Wolf. *Atom- und Quantenphysik.* Springer Verlag (1996).

[21] J. Howard, C. Michael, F. Glass et al. "Time-resolved two-dimensional plasma spectroscopy using coherence.imaging techniques." *Plasma Physics and Controlled Fusion*, vol. 45, pp. R1143 (2003).

[22] J. Howard. "Snapshot-imaging motional Stark effect polarimetry." *Plasma Physics and Controlled Fusion*, vol. 50, p. 125003 (2008).

[23] I. H. Hutchinson. *Principles of Plasma Diagnostic.* Cambridge Press (1987).

[24] J. Harhausen. *Interpretation of D_α Imaging Diagnostics Data on ASDEX Upgrade Tokamak.* Ph.D. thesis, LMU München (2008).

[25] O. P. Ford, J. Howard, M. Reich et al. "First Results from the Imaging Motional Stark Effect diagnostic on ASDEX Upgrade." *40. EPS Conference on Plasma Physics* (2013).

[26] O. P. Ford, J. Howard and R. Wolf. "The ASDEX Upgrade prototype Imaging Motional Stark Effekt (IMSE) disgnostic." *unpublished* (2014).

[27] O. P. Ford, J. Howard and R. Wolf. "Performance tests of the ASDEX Upgrade Imaging Motional Stark Effect diagnostic (IMSE)." *40. EPS Conference on Plasma Physics* (2013).

[28] D.Eimerl, L. Davis, S. Velsko et al. "Optical, mechanical and thermal properties of barium borate." *AIP Journal of Applied Physics*, vol. 62, no. 5, pp. 1968 (1987).

[29] O. Marchuk, Y. Ralchenki and R. K. Janev. "Collisional excitation and emission of H_α Stark multiplet in fusion plasmas." *Journal of Physics B*, vol. 43 (2010).

[30] O. Marchuk. "private communication." (2014).

[31] P. Mc Carthy, C. Forest, M. Foley et al. "Plasma geometry and current profile identification on ASDEX Upgrade using an integrated equilibrium generation and interpretation system." In "Proc. 21st. Int. Conf. on Fusion Energy 2006 (Chengdu, 2006)," (2007).